KAHRAMANMARAŞ SÜTÇÜ İMAM ÜNİVERSİTESİ

e-ISSN 1309-1751

Mühendislik Bilimleri Dergisi
Journal of Engineering Sciences

2023

SAYI / NUMBER : 4

CİLT / VOLUME :

Özel Sayı/Special Issue

IFSCOM-E 2023

e-ISSN 1308-7751

Kahramanmaraş Sütçü İmam University
Journal of Engineering Sciences

Yazışma Adresi / Corresponding Address

Kahramanmaraş Sütçü İmam Üniversitesi
Mühendislik Bilimleri Dergisi
46050, Onikişubat/Kahramanmaraş
TÜRKİYE

E - Posta

jes@ksu.edu.tr

Web

http://jes.ksu.edu.tr/

Bu dergi hakemli olup yılda 4 kez yayınlanır.
This journal is peer - reviewed and published 4 issues per year.

e-ISSN 1308-1751

Kahramanmaraş Sütçü İmam University
Journal of Engineering Sciences

Cilt / Volume : 26 Özel Sayı / Special Issue Yıl / Year : 2023

Res. Assist. Yalın YAMAÇ
Technical Manager
KSU Univ. TURKEY
yalinyamac@ksu.edu.tr

Res. Assist. Arif ÇUTAY
Technical Manager
KSU Univ. TURKEY
arifcutay@ksu.edu.tr

Danışma Kurulu / Advisory Board

e-ISSN 1308-1751

Kahramanmaraş Sütçü İmam University
Journal of Engineering Sciences

İÇİNDEKİLER

ARAŞTIRMA MAKALESİ – RESEARCH ARTICLE

e-ISSN 1309-4751

Kahramanmaraş Sütçü İmam University
Journal of Engineering Sciences

BU SAYIYA (CİLT 26 IFSCOM-E 2023 ÖZEL SAYI) KATKI VEREN HAKEMLER

Ekinhan ERİŞKİN	Ecir KÜÇÜKSİLLE
Cafer AVCI	Kubilay TAŞDELEN
Murat UÇAR	Nazım MAHMUDOV
Erdem BAYTUNÇ	Ali DEMİRCİ
Duygu ÇELİK ERTUĞRUL	Yıtan BİTİRİM
Abdullah Engin ÖZÇELİK	Özgür SOLMAZ
Gökhan ÖZÇELİK	Kemal ALAYKIRAN
Emre ÇALIŞKAN	Mustafa Yusuf YAZICI
Ataollah KHANLARI	Faraz AFSHARİ
Levent KARA	Nalan ÖZDEMİR

KSÜ Mühendislik Bilimleri Dergisi, 26(Özel Sayı), 2023 KSU J Eng Sci, 26(Special Issue), 2023
9th Uluslararası IFS Çağdaş Matematik ve Mühendislik Konferansı Özel Sayısı
9th International IFS Contemporary Mathematics and Engineering Conference Special Issue
Araştırma Makalesi Research Article

Kahramanmaras Sutcu Imam University
Journal of Engineering Sciences

Geliş Tarihi : 01.08.2023 Received Date : 01.08.2023
Kabul Tarihi : 02.11.2023 Accepted Date : 02.11.2023

A STUDY ON OPTIMIZING TRAFFIC SIGNAL CONTROL FOR IMPROVED TRAFFIC FLOW

İYİLEŞTİRİLMİŞ TRAFİK AKIŞI İÇİN TRAFİK SİNYAL KONTROLÜNÜN OPTİMİZE EDİLMESİ ÜZERİNE BİR ÇALIŞMA

Serap ERGÜN[1] (ORCID: 0000-0003-2504-5101)

[1] Isparta Uygulamalı Bilimler Üniversitesi, Bilgisayar Mühendisliği Bölümü, Isparta, Türkiye

*Sorumlu Yazar / Corresponding Author: Serap ERGÜN, serapbakioglu@isparta.edu.tr

ABSTRACT

Addressing traffic congestion holds paramount importance due to its severe economic and environmental repercussions. This study introduces an approach to address this pervasive issue by employing a wide-area control strategy for diverse road networks. The strategy leverages a dynamic offset control method and a multi-agent model to create a unique solution. In this framework, individual intersections function as distinct agents, engaging in negotiations, establishing connections, and forming a dynamic offset control zone resembling a tree structure. Within this structure, agents collaboratively manage green wave synchronization based on real-time traffic conditions at the network boundaries. To evaluate the effectiveness of this approach, comprehensive tests utilize both a simulated road network (Experiment 1) and an actual grid-like road network (Experiment 2). In Experiment 1, the proposed method consistently reduces lost time, resulting in an average reduction of 15% across all scenarios. Experiment 2 demonstrates a reduction in lost time across various intervals, with an impressive average reduction of 34% in lost time across all scenarios. These results demonstrate the strategy's ability to dynamically and adaptively establish green waves that significantly enhance traffic flow. In conclusion, this study demonstrates that the proposed method autonomously conducts offset control, effectively contributing to the smooth flow of vehicles.

Keywords: Traffic congestion, dynamic offset control, multi-agent model, green wave control, traffic flow enhancement

ÖZET

Trafik sıkışıklığının giderilmesi, ciddi ekonomik ve çevresel yansımaları nedeniyle büyük önem taşıyor. Bu çalışma, çeşitli yol ağları için geniş alanlı bir kontrol stratejisi kullanarak bu yaygın sorunu çözmeye yönelik bir yaklaşım sunmaktadır. Strateji, benzersiz bir çözüm oluşturmak için dinamik bir dengeleme kontrol yönteminden ve çok etmenli bir modelden yararlanır. Bu çerçevede bireysel kesişimler, müzakerelere katılan, bağlantılar kuran ve bir ağaç yapısına benzeyen dinamik bir dengeleme kontrol bölgesi oluşturan ayrı aktörler olarak işlev görür. Bu yapı içerisinde aracılar, ağ sınırlarındaki gerçek zamanlı trafik koşullarına dayalı olarak yeşil dalga senkronizasyonunu işbirliği içinde yönetir. Bu yaklaşımın etkinliğini değerlendirmek için, kapsamlı testler hem simüle edilmiş bir yol ağını (Deney 1) hem de gerçek ızgara benzeri bir yol ağını (Deney 2) kullanır. Deney 1'de önerilen yöntem, kayıp zamanı sürekli olarak azaltarak tüm senaryolarda ortalama %15'lik bir azalmaya yol açtı. Deney 2, tüm senaryolarda kayıp sürede ortalama %34'lük etkileyici bir azalmayla, çeşitli aralıklarla kayıp sürede bir azalma olduğunu göstermektedir. Bu sonuçlar, stratejinin trafik akışını önemli ölçüde artıran yeşil dalgaları dinamik ve uyarlanabilir bir şekilde oluşturma yeteneğini göstermektedir. Sonuç olarak bu çalışma, önerilen yöntemin otonom olarak ofset kontrolü gerçekleştirdiğini ve araçların düzgün akışına etkili bir şekilde katkıda bulunduğunu göstermektedir.

ToCite: ERGÜN, S., (2023). A STUDY ON OPTIMIZING TRAFFIC SIGNAL CONTROL FOR IMPROVED TRAFFIC FLOW. *Kahramanmaraş Sütçü İmam Üniversitesi Mühendislik Bilimleri Dergisi*, 26(Özel Sayı) 1097-1108.

Anahtar Kelimeler: Trafik sıkışıklığı, dinamik ofset kontrolü, çok etmenli model, yeşil dalga kontrolü, trafik akışı geliştirme

INTRODUCTION

Traffic congestion is a condition where the volume of vehicles on a road network exceeds its capacity, resulting in slower traffic flow, longer travel times, and often complete standstills. It is a significant urban transportation problem characterized by reduced mobility, environmental harm, and economic costs. Congestion leads to increased fuel consumption, lost productivity, and additional maintenance expenses for vehicles. Moreover, it contributes to air pollution, greenhouse gas emissions, and adverse health effects due to prolonged exposure to traffic-related pollutants. It also has a negative impact on the quality of life, causing stress and reducing leisure time for residents of congested areas (Abdurakhmanov, R., 2022).

Addressing traffic congestion is vital for several reasons. It has a substantial economic impact, resulting in lost productivity and increased operating costs for businesses. It can also discourage investment and economic growth in congested regions. From an environmental standpoint, congestion contributes to air pollution and worsens climate change by increasing greenhouse gas emissions. It has public health implications, as it can lead to stress and health issues such as cardiovascular and respiratory problems. Reducing congestion improves the efficiency of transportation networks, facilitating the movement of people and goods, which, in turn, boosts economic activity. Congestion management is an integral part of urban planning, ensuring the development of livable and sustainable cities (Cao et al., 2022; Alsaawy et al., 2022). It also promotes equity by providing equitable access to jobs, education, and services for all members of the community. In essence, addressing traffic congestion is crucial for creating more efficient, environmentally friendly, and socially inclusive urban environments.

Traffic congestion has emerged as a pressing concern, attributed to the escalating traffic demand on road networks resulting from increased motorization and economic growth (Yang, 2023). Given the detrimental effects of traffic on pollution, resolving congestion holds significant importance. Extensive research efforts are underway to enhance traffic signal control and augment the processing capacity of existing road networks for improved traffic flow (Babaei et al., 2023; Abdurakhmanov, R., 2022).

Signal control parameters encompass cycle length, split, and offset, among others. This study focuses on offset control, which refers to the phase difference between adjacent signalized intersections (Alsaawy et al., 2022). Effective control of offsets can minimize the frequency of vehicle stops at red lights. Notably, approaches such as GreenWave (Yuan and Zheng, 2022; Cao et al., 2022) prioritize offset control to optimize directional traffic flows. In recent years, the concept of Bidirectional Green Wave (Zhu et al., 2023; Karimov, 2023), which facilitates synchronized traffic flow in both directions, has been proposed. Additionally, offset control methods utilizing real-time traffic information through intersection communication have gained prominence (Ji and Cheng, 2022).

One notable example of early online control is proposed by Soon et al. (2019), which employs statistical parameter design and fine-tuning based on sensor data. While these methods continue to be widely utilized, recent years have witnessed an increase in proposals for more dynamic or real-time offset control techniques. One such proposal involves a distributed control method that divides the mixed integer linear programming problem into intersections, with the objective function centered on the link queue length (Ma and He, 2019; Khamis and Gomaa, 2014).

Numerous control methods have been suggested for determining the offset value (Yang and Yang, 2022). However, most of these methods concentrate on fixed control target areas, predominantly focusing on single arterial roads (Lu et al., 2022; Wu et al., 2014). Addressing this limitation, this study introduces an online offset control model that dynamically constructs offset control areas on a road network using a multi-agent model.

The proposed method operates on the fundamental principles of GreenWave. A tree structure is established, primarily focusing on intersections with high traffic concentration, and the offset values are determined based on directional traffic flows. Experiments conducted using both a simulated grid-like road network and an existing road network showcased the dynamic and autonomous capabilities of the proposed method in constructing GreenWave. Furthermore, it demonstrated a remarkable efficacy in smoothing traffic flow compared to the existing control system in France.

The urgency of mitigating traffic congestion is underscored by its far-reaching consequences on the environment and daily life. The evolution of offset control methods, as evidenced by this study, highlights the ongoing pursuit of innovative solutions to enhance traffic flow and reduce congestion, ultimately contributing to more sustainable and efficient urban transportation systems.

The contributions of this study to the literature can be summarized as follows:

Comprehensive Understanding of Traffic Congestion: This study provides a comprehensive overview of traffic congestion, outlining its multifaceted nature, including its impact on mobility, economics, environment, and public health. It sets the stage for understanding the urgency of addressing this urban transportation challenge.

Focus on Offset Control: The study emphasizes the importance of offset control as a key parameter in traffic signal management. It highlights how effective offset control can alleviate congestion by reducing unnecessary stops at traffic lights, thus improving traffic flow.

Exploration of Innovative Solutions: By introducing an online offset control model that employs a multi-agent approach, the study delves into innovative solutions for addressing congestion. It breaks away from traditional fixed-control methods and explores dynamic, real-time approaches.

Application of GreenWave Principles: The study builds on the fundamental principles of GreenWave, a well-established concept in traffic management. It adapts these principles to develop a dynamic offset control strategy that can be applied in various road network scenarios.

Empirical Evidence: Through experiments conducted in both simulated and real-world road network settings, the study provides empirical evidence of the effectiveness of the proposed online offset control model. This empirical validation contributes to the practicality and applicability of the research findings.

In summary, this study not only serves as a comprehensive primer on traffic congestion but also introduces innovative offset control strategies and provides empirical support for their effectiveness. It contributes to the ongoing discourse on congestion management, offering valuable insights and solutions for creating more sustainable and efficient urban transportation systems.

The structure of the paper is as follows: Problem statement is presented in Section 2, the proposed method is proposed in Section 3. The evaluation experiments and results are given in Section 4. And finally, the conclusion and outlook part is given in Section 5.

PROBLEM STATEMENT

The challenge of traffic congestion presents significant economic and environmental implications (Wang and Hussain, 2021). Traffic congestion occurs when the road's capacity to facilitate smooth traffic flow is exceeded by the volume of vehicles, leading to increased travel times, elevated fuel consumption, and higher emissions, resulting in substantial economic losses and environmental harm (Tobita and Nagatani, 2013).

The focus of this study lies in the optimization of traffic signal control, a critical strategy for congestion mitigation (Chen and Chang, 2016). To effectively implement offset control using GreenWave, it is imperative that a consistent cycle length is maintained across all signalized intersections (Tobita and Nagatani, 2013). The cycle length, signifying the duration of a complete sequence of signal phases at an intersection, including green and red phases, is crucial for the success of GreenWave-based traffic signal coordination, as it ensures the smooth progression of vehicles through the network.

To establish this uniform cycle length, the unique characteristics of each intersection are considered, including link distances, system speeds, the number of vehicles entering from specific links, and the traffic capacity of the intersection per cycle (Wang and Hussain, 2021). These factors play a pivotal role in determining the optimal cycle length and, consequently, the effectiveness of offset control in enhancing traffic flow.

Therefore, the central problem addressed in this research is the strategic optimization of traffic signal control, with a specific focus on the establishment of a consistent cycle length across various signalized intersections, aiming to

alleviate traffic congestion and enhance the overall efficiency of the road network. This approach seeks to minimize travel times, reduce fuel consumption, and mitigate environmental impacts, contributing to a more sustainable and economically viable transportation system.

In Figure 1, the adjacent signalized intersections (Wang and Hussain, 2021) are depicted at the bottom, and the variables are defined as follows:

$l_{(i,j)}$ represents the link distance between i and j.
$v_{(i,j)}$ denotes the system speed between i and j.
$p_{(i,j)}$ represents the number of vehicles entering from link i->j to intersection i in a single cycle.
Cap_i is traffic capacity of intersection i per cycle.
$Cap_{(ij)}$: indicates the traffic capacity of intersection i per cycle, encompassing the traffic capacity of link $i \rightarrow j$ per cycle.
For this research, the traffic capacity is calculated as 0.5 $veh.lane^{-1}.s^{-1}$.
Let J represent the set of intersections adjacent to intersection i. The total number of vehicles entering intersection i during one cycle is defined by Equation 1.

$$P_i = \sum_{j \in J} p(j,i) \tag{1}$$

To implement offset control using GreenWave, it is essential to ensure that the cycle length remains consistent across all intersections (Tobita and Nagatani, 2013). In alignment with the methodology employed in this study, where GreenWave is utilized, it is assumed a uniform cycle length for all intersections under control (Chen and Chang, 2016). This means that the duration of green and red phases at each signalized intersection is synchronized to be the same, ensuring that vehicles progress smoothly through the network. The need for a uniform cycle length arises from the core principles of GreenWave, where the coordination of traffic signals relies on synchronized timing.

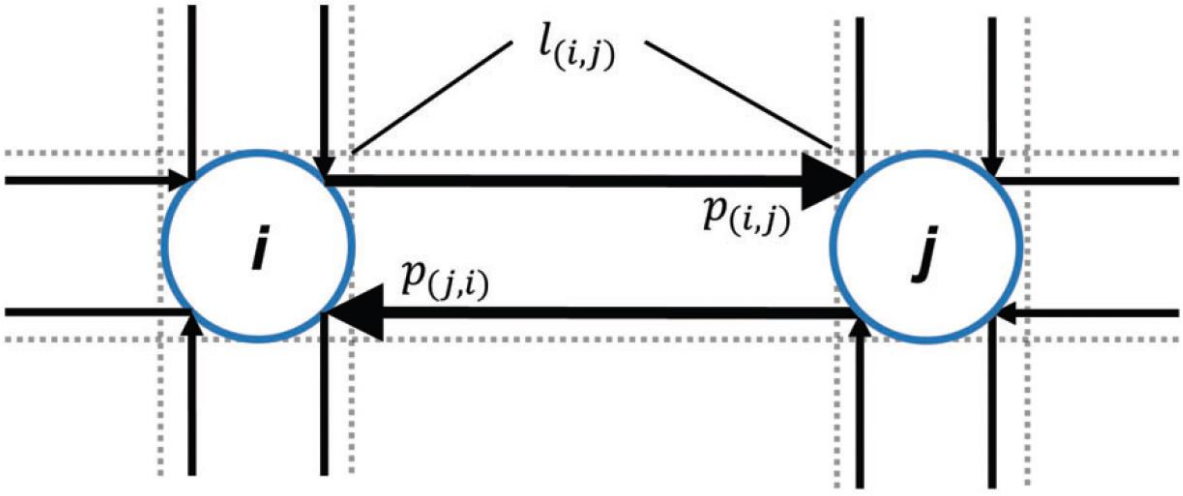

Figure 1. Two Adjacent Intersections

PROPOSED METHOD

In this method, each signalized intersection is virtually assigned an agent. In addition to the information outlined in the Problem Statement section, the agent is assumed to have access to the signal schedule information. Control operations are executed based on the information surrounding the assigned intersection.

The agent assesses the level of traffic congestion at the assigned intersection, determining whether the application of offset control is warranted. It's important to note that while the offset value is always present, the agent's role involves dynamic adjustments to this value based on real-time traffic conditions.

If the agent deems offset control necessary, it initiates negotiations with neighboring intersections to establish cooperative measures. Through a series of actions, the agent dynamically constructs an organizational framework for collaborative control and conducts offset control within this framework.
Furthermore, when it is determined that the degree of traffic congestion has significantly reduced, coordinated control is concluded.

Agent Configuration

Each agent is constantly in one of the five following states (modes):
Isolation: A state characterized by non-coordination.
Root: The central state of cooperative control.
Sub-Root: A state in which the agent serves as a component of the area.
Clearance Root: A state occurring just before the Root agent concludes cooperative control.
Clearance Sub-Root: The state immediately preceding the conclusion of cooperative control by the sub-agent.

Collaborative Functions

Let A_i represent the agent at a specific intersection, and A_j denote the agent at an adjacent intersection j to intersection i. If A_i is a Sub agent, A_i^R refers to the root agent of the organization to which A_i belongs.

Root Generation

The Isolation agent verifies the satisfaction of Eq. 2 by the Sub agent and confirms if Eq. 3 is met to determine whether a transition to the Root agent is required. This assessment is conducted on a per-cycle basis. In this context, α denotes a constant, and P_R^i represents the total number of vehicles entering the intersection where A_R^i is positioned.

$$P_i > \alpha Cap_i \quad (2)$$
$$P_i > P_R^i \quad (3)$$

Negotiation

Once A_i transitions to the Root mode, it initiates a cooperative proposal to its neighbouring agent A_j when Eq. 4 is fulfilled. In this context, β represents a constant.

If A_j is in the Isolation mode, the proposal is unconditionally accepted. If A_j is in the Sub mode, the proposal is accepted only when Eq. 5 is met. Lastly, if A_j is in the Root mode, the proposal is accepted provided Eq. 6 is satisfied.

$$P_i > P_R^j \quad (5)$$
$$P_i > P_j \quad (6)$$

If the proposal is accepted, A_j undergoes a transition to the Sub mode with A_i as its parent. During this process, the relative offset between the two agents is computed. However, if the proposal is not accepted, A_j remains unchanged.

Propagation

The Sub mode is activated by A_j's change. When Equation 7 is satisfied, a collaborative proposal is made to the neighboring agent, A_k. However, if A_k is already affiliated with A_R^j, the cooperative performance is not allowed.

$$\left(p(j,k) > \beta Cap_{(j,k)}\right) \vee \left(p(j,k) > \beta Cap_{(j,k)}\right) \quad (7)$$

If the Isolation mode is active for A_k, the proposal is unconditionally accepted. If the Sub mode is active for A_k, the proposal is accepted if Equation 8 is satisfied. If the Root mode is active for A_k, the proposal is accepted if Equation 9 is satisfied.

$$P_R^j > P_R^k \quad (7)$$
$$P_R^j > P_k \quad (8)$$

If the proposal is accepted, A_k is switched to Sub mode with A_k as the parent. At this point, the relative offset between the two is calculated. If the proposal is not accepted, A_k remains unchanged. Following that, the cooperative proposal

continues to propagate until it becomes completely unacceptable, forming a tree structure around the initiating agent and the subagents that have accepted the proposal. Offset control is executed within the organization formed in this manner.

Organization Dissolution

When Equation 10 is satisfied by the root agent, it is determined that traffic concentration has been reduced, and organization dissolution is carried out. In this equation, θ represents a constant, and $\overline{P_i}$ denotes the average number of vehicles entering the root agent over the past few cycles.

$$\overline{P_i} < \theta Cap_i \tag{10}$$

The message regarding the dissolution of the organization propagates throughout the entire organization in a chain reaction. Consequently, the Root mode agent is switched to ClearanceRoot mode, while the Sub mode agent is switched to ClearanceSub mode. After offset cancellation based on the ClearanceRoot agent, the ClearanceSub agent transitions to the Isolation mode. Similar to the Isolation agent, both the ClearanceRoot agent and the ClearanceSub agent assess changes to the Root mode. If they receive a collaborative proposal, they accept it unconditionally.

Offset Control

Within the organized structure, the offset is computed by each agent for every cycle. Considering adjacent intersections i and j, where i serves as the parent agent and j as the child agent. Furthermore, considering the values $p(i,j)$ and $p(j,i)$, the larger value is designated as p_l, and the smaller value as p_s. The traffic volume deviation r for each direction is then determined using Equation 11.

$$r = \frac{p_l}{p_s} \tag{11}$$

Table 1. The Inflows of Vehicles for the Experiment 1

	Vehicle inflow ($veh/h.each\ row$)	
time (s)	West-East	East-West
0-7200	1000	0
7200-7800	0	0
7800-15000	0	1000

The duration of two hours of traffic flow and 30-minute pauses is chosen to simulate different traffic scenarios that encompass peak and off-peak traffic periods. This approach allows to evaluate the effectiveness of our offset control strategy under various traffic conditions.

Next, the absolute value O_r of the relative offset is calculated by Equation 12. Here, γ, δ $(\gamma > \delta \geq 1)$ are constant threshold values.

The threshold values γ and δ, as mentioned in the equations, play a significant role in determining the relative offset O_r and, subsequently, the cycle start time t_j at intersection j. Here's an explanation of these threshold values:

Threshold Value γ: This threshold value, denoted as γ, serves as a crucial parameter in the calculation of the relative offset O_r when determining whether to adjust the offset. When the relative offset r exceeds this threshold $(r \geq \gamma)$, it triggers the calculation of O_r using the formula: $O_r = \frac{l_{(i,j)}}{v_{(i,j)}}$. In this context, γ acts as a criterion for evaluating whether the traffic conditions, as indicated by r, warrant a change in offset.

Threshold Value δ: δ is another threshold value, and it is used in conjunction with γ to calculate O_r when the relative offset falls within a certain range $(1 \geq r \geq \gamma)$. Specifically, when r falls within this range, O_r is calculated using the formula: $O_r = \frac{r-\delta}{\gamma-\delta}$. δ helps define a transitional region where offset adjustments are considered. It represents the lower boundary of the range within which offset changes are gradually introduced.

These threshold values, γ and δ, are integral to the offset control algorithm, as they determine the conditions under which offset adjustments are made. γ represents a higher threshold, signifying more substantial changes in offset, while δ defines a transitional zone where offset adjustments are moderate. The choice of these threshold values depends on the specific traffic conditions and the desired level of offset control responsiveness.

$$O_r = \begin{cases} \dfrac{l_{(i,j)}}{v_{(i,j)}}, & (r \geq \gamma) \\ \dfrac{l_{(i,j)}}{v_{(i,j)}} \dfrac{r-\delta}{\gamma-\delta}, & (1 \geq r \geq \gamma) \\ 0, & (r \leq 1) \end{cases} \tag{12}$$

The relative offset $O_{(i,j)}$ from A_i to A_j can be calculated by Equation 13.

$$O_{(i,j)} = \begin{cases} O_r, & (p_{(i,j)} > p_{(j,i)}) \\ -O_r, & (p_{(i,j)} \geq p_{(j,i)}) \end{cases} \tag{13}$$

Finally, the cycle start time t_j at intersection j is derived from Equation 14. Here, t_i represents the start time of the next cycle at intersection i, and $split_i$ denotes the duration of time allocated for the indication of the corresponding direction at intersection i.

$$t_j = t_i + O_{(i,j)} + split_i \tag{14}$$

In summary, γ and δ are key parameters in the offset control algorithm, helping to evaluate and regulate offset adjustments based on the relative offset r between intersections. Their values are carefully chosen to strike a balance between maintaining traffic flow efficiency and adapting to changing traffic conditions.

EVALUATION EXPERIMENT

Two experiments are conducted to examine the feasibility of dynamic offset control by the proposed method and its effectiveness.

In the current signal control used for comparison, the offset variation is limited to 25% of the cycle length per cycle. Therefore, when an offset exceeding the variation limit is calculated in the evaluation experiment, this variation is reflected in several cycles.

Experiment 1: Grid Road Network

A comparative experiment is conducted on a grid road network consisting of 5 rows and 5 columns, where signal control without offset control is employed. Both the proposed method and the comparative method have a cycle length of 90 seconds. Table 1 presents the count of inflow vehicles.

Experiment 2: Real Area Network

A comparative experiment is conducted on a road network that replicates an actual area in Clermont-Ferrand Prefecture, as depicted in Figure 2. The intersections to be controlled are represented by red circles in Figure 2, with a total of 16 locations.

For the control parameters, the values utilized in the current control at the site are employed. However, due to the constraint of offset control, the cycle length is standardized to 120 seconds for all intersections, using only the proposed method.

Table 2 displays the count of inflow vehicles. In this context, R_1, R_2, and R_3 denote the routes $B \rightarrow F \rightarrow A, D \rightarrow G \rightarrow C$, and $E \rightarrow G \rightarrow F \rightarrow A$, respectively.

Additionally, the reverse routes are indicated by primed symbols, such as R_1'.

Simulation Parameters

In this study, the experiment utilized SUMO (Simulation of Urban Mobility). As the method proposed in this paper focuses on offset control, a uniform value for the split duration is employed across all methods.

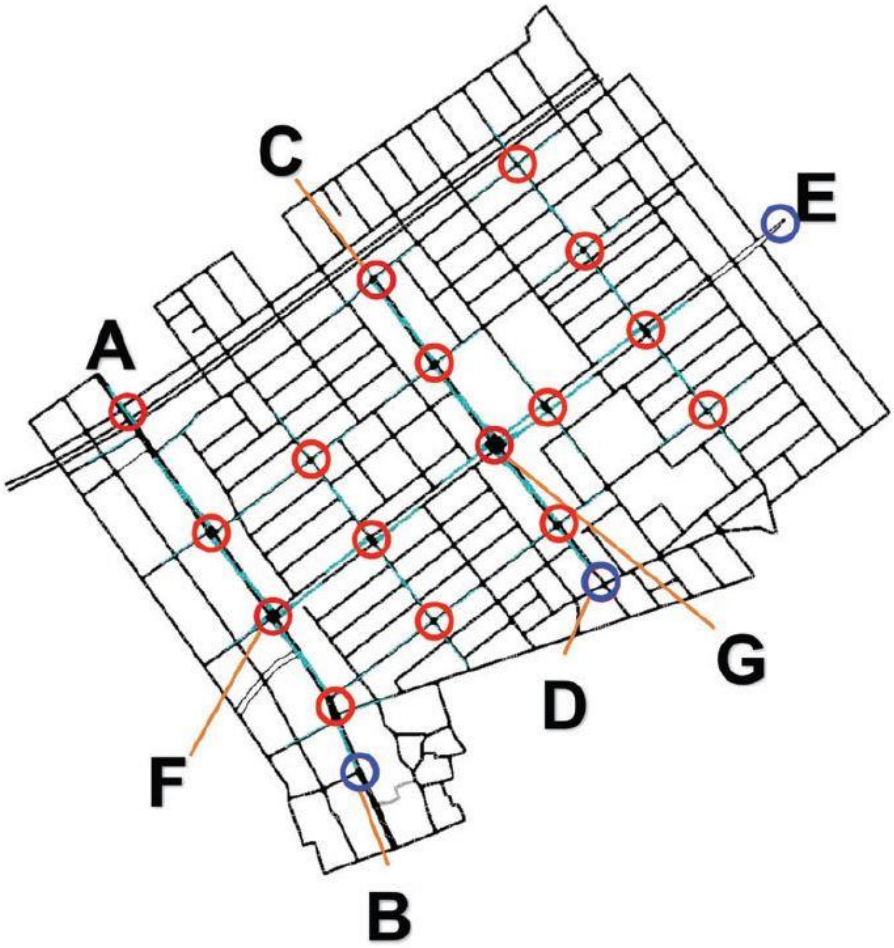

Figure 2. The Simulated Area

Table 2. The Inflows of Vehicles for the Experiment 2

	Vehicle inflow (veh/h)		
time (s)	R_1	R_2	R_3
0-7200	1350	1350	500
7200-7800	0	0	0
	R_1'	R_2'	R_3'
7800-15000	1350	1350	500

For the parameters used in Equations 2, 4, 10, and 12, the values of Equation 15 are used.

$$\begin{pmatrix} \alpha \\ \beta \\ \gamma \\ \delta \\ \theta \end{pmatrix} = \begin{pmatrix} 0.4 \\ 0.15 \\ 1.5 \\ 1.1 \\ 0.8 \end{pmatrix} \tag{15}$$

In the study, an investigation within the Clermont-Ferrand Prefecture is conducted, focusing on a critical main road and its associated intersections, where the traffic volume data over a 2-hour duration is collected. This main road spans approximately 10 kilometers within the Clermont-Ferrand Prefecture.

Experimental Results

In this study, the effectiveness is assessed based on vehicle lost time.

Figure 3 illustrates the average loss time progression in Experiment 1, while Figure 4 presents the average loss time progression in Experiment 2. Furthermore, Table 3 provides statistical values for the entire scenario in each experiment.

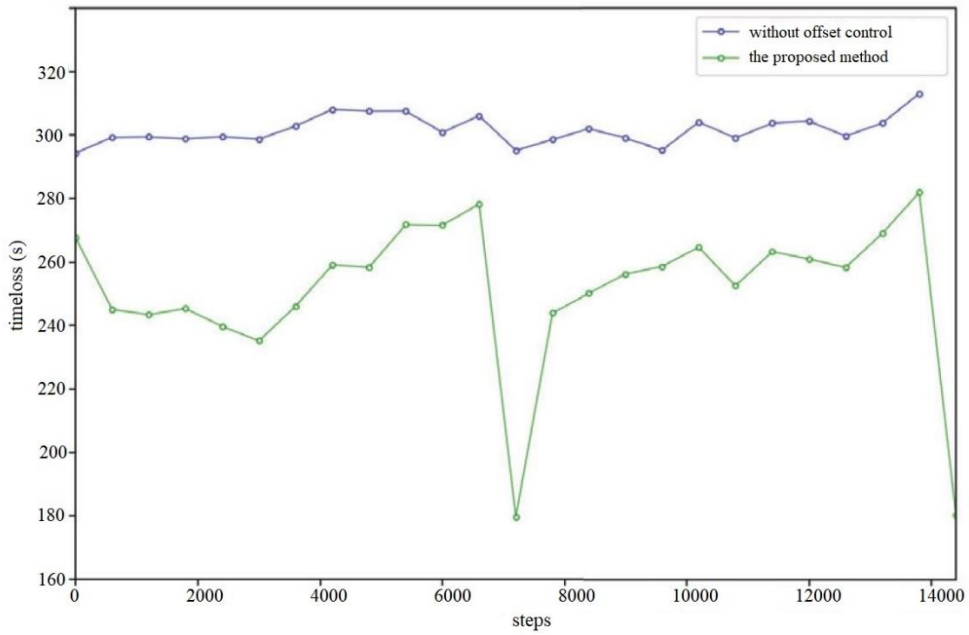

Figure 3. Variation of Average Loss Time for Experiment 1

For Experiment 1, the proposed method consistently reduced lost time throughout the duration, as depicted in Figure 3. Moreover, as indicated in Table 3, the proposed method achieved an average reduction of 15% in lost time across all scenario variations.

In Experiment 2, the proposed method exhibited a reduction in lost time across almost all time intervals, as demonstrated in Figure 4. Additionally, according to Table 3, the proposed method yielded an average reduction of 34% in lost time across all scenarios within the actual area of rice fields.

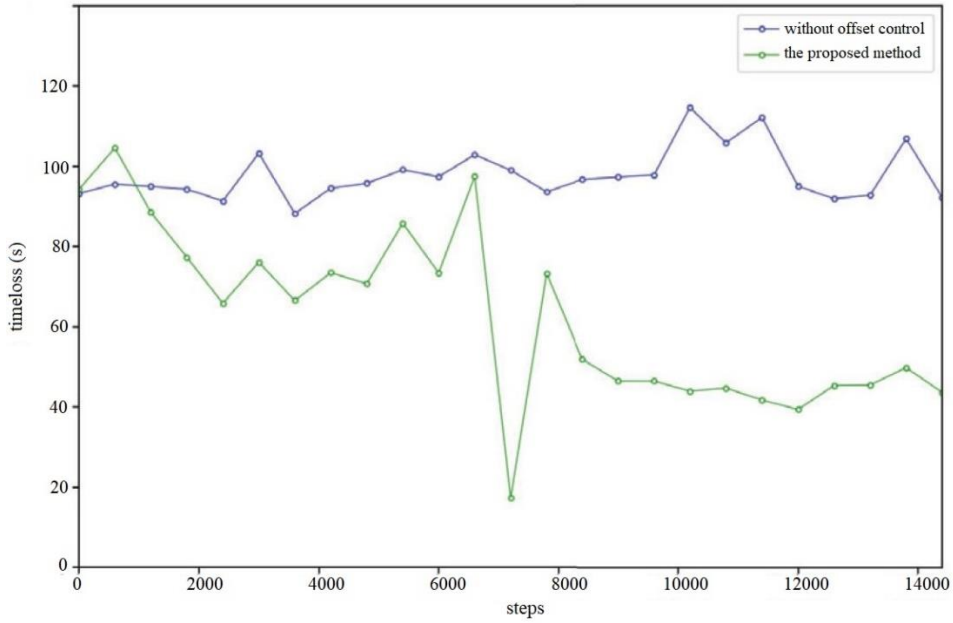

Figure 4. Variation of Average Loss Time for Experiment 2

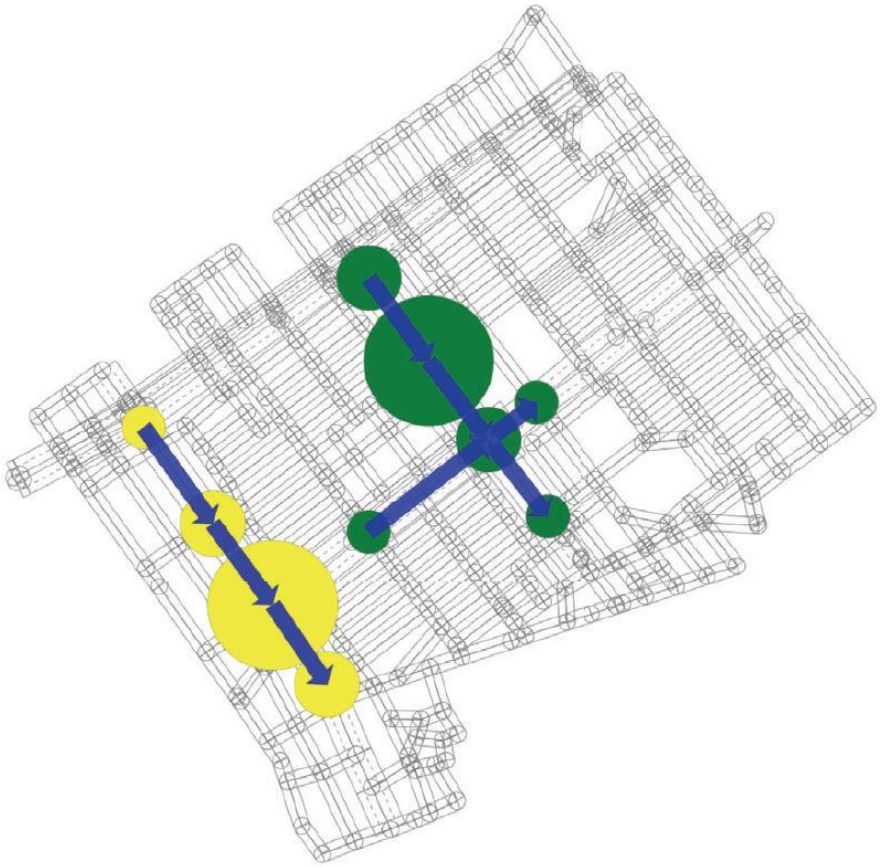

Figure 5. The Visualisation of Organization of Experiment 2

Figure 5 offers a visualization of a specific instance depicting agent tissue formation and offset control in Experiment 2. The coloured circles represent Root or Sub mode agents, signifying their affiliation within the same organization. The arrows in the figure indicate the execution of offset control, prioritizing the direction indicated by each arrow. This visualization confirms the seamless operation facilitated by the proposed method.

Based on the above findings, it is evident that the proposed method autonomously performs offset control and effectively contributes to the smooth flow of vehicles.

CONCLUSION AND OUTLOOK

In this study, a dynamic offset control method utilizing a multi-agent model is proposed with the objective of enhancing traffic flow. The aim is to enable autonomous construction of control areas by groups based on prevailing traffic conditions. The concept of GreenWave, widely employed in current practices, served as the control standard for the agents in this research.

Through simulation experiments, it is demonstrated that the proposed method effectively autonomously performs offset control, establishes GreenWave patterns, reduces vehicle loss time, and improves traffic flow.

Looking ahead, future prospects encompass the exploration of various related approaches such as offset optimization methods and traffic condition prediction, which have emerged in recent years. It is conceivable that the model proposed in this study, which autonomously constructs control areas, could be further developed by integrating alternative offset control standards beyond GreenWave and leveraging predictive information for traffic condition assessment. This holds promise for advancing the field of traffic control and optimization.

In the realm of Cooperative Intelligent Transport Systems, various avenues offer opportunities for advancements in addressing traffic congestion and optimizing traffic signal control. These include advanced data analytics, machine learning and artificial intelligence techniques, cooperative strategies, integration of transportation modes, network-wide optimization approaches, and the integration of emerging technologies such as connected and autonomous

vehicles. Scalability, adaptability, and real-world pilot studies are essential considerations for implementing and evaluating these strategies.

Additionally, comprehensive cost-benefit analysis is crucial to quantify the economic, environmental, and societal impacts of different traffic signal control approaches. This analysis will assist in decision-making processes and prioritize strategies based on their value and benefits.

By delving into these areas of research and development, the field of traffic signal control for Cooperative Intelligent Transport Systems can continue to evolve. These efforts hold the potential to create more efficient, sustainable, and congestion-free transportation networks, ultimately improving the quality of life for individuals and societies alike.

REFERENCES

Abdurakhmanov, R. (2022). Determination of Traffic Congestion and Delay of Traffic Flow At Controlled Intersections. The American Journal of Engineering and Technology, 4(10), 4-11.

Alsaawy, Y., Alkhodre, A., Abi Sen, A., Alshanqiti, A., Bhat, W. A., & Bahbouh, N. M. (2022). A comprehensive and effective framework for traffic congestion problem based on the integration of IoT and data analytics. Applied Sciences, 12(4), 2043.

Babaei, A., Khedmati, M., Jokar, M. R. A., & Tirkolaee, E. B. (2023). Sustainable transportation planning considering traffic congestion and uncertain conditions. Expert Systems with Applications, 227, 119792.

Cao, M., Li, V. O., & Shuai, Q. (2022). Book Your Green Wave: Exploiting Navigation Information for Intelligent Traffic Signal Control. IEEE Transactions on Vehicular Technology, 71(8), 8225-8236.

Chen, L. W., & Chang, C. C. (2016). Cooperative traffic control with green wave coordination for multiple intersections based on the internet of vehicles. IEEE Transactions on Systems, Man, and Cybernetics: Systems, 47(7), 1321-1335.

Ji, L., & Cheng, W. (2022). Method of Bidirectional Green Wave Coordinated Control for Arterials under Asymmetric Release Mode. Electronics, 11(18), 2846.

Karimov, A. (2023). " Green Wave" Module for Creating An Artificial Intelligence-Based Adaptive Complex Of Road Network Permeability To Improve Road Traffic Safety. International Bulletin of Engineering and Technology, 3(3), 108-127.

Khamis, M. A., & Gomaa, W. (2014). Adaptive multi-objective reinforcement learning with hybrid exploration for traffic signal control based on cooperative multi-agent framework. Engineering Applications of Artificial Intelligence, 29, 134-151.

Lu, K., Jiang, S., Xin, W., Zhang, J., & He, K. (2022). Algebraic method of regional green wave coordinated control. Journal of Intelligent Transportation Systems, 1-19.

Lu, K., Tian, X., Jiang, S., Lin, Y., & Zhang, W. (2023). Optimization Model of Regional Green Wave Coordination Control for the Coordinated Path Set. IEEE Transactions on Intelligent Transportation Systems.

Ma, C., & He, R. (2019). Green wave traffic control system optimization based on adaptive genetic-artificial fish swarm algorithm. Neural Computing and Applications, 31, 2073-2083.

Soon, K. L., Lim, J. M. Y., & Parthiban, R. (2019). Coordinated traffic light control in cooperative green vehicle routing for pheromone-based multi-agent systems. Applied Soft Computing, 81, 105486.

Tobita, K., & Nagatani, T. (2013). Green-wave control of an unbalanced two-route traffic system with signals. Physica A: Statistical Mechanics and its Applications, 392(21), 5422-5430.

Wang, T., Cao, J., & Hussain, A. (2021). Adaptive Traffic Signal Control for large-scale scenario with Cooperative Group-based Multi-agent reinforcement learning. Transportation research part C: emerging technologies, 125, 103046.

Wu, X., Deng, S., Du, X., & Ma, J. (2014). Green-wave traffic theory optimization and analysis. World Journal of Engineering and Technology, 2(3), 14-19.

Yang, S. (2023). Hierarchical graph multi-agent reinforcement learning for traffic signal control. Information Sciences, 634, 55-72.

Yang, S., & Yang, B. (2022). An inductive heterogeneous graph attention-based multi-agent deep graph infomax algorithm for adaptive traffic signal control. Information Fusion, 88, 249-262.

Yuan, S., Xu, S., & Zheng, S. (2022, January). Deep reinforcement learning based green wave speed guidance for human-driven connected vehicles at signalized intersections. In 2022 14th International Conference on Measuring Technology and Mechatronics Automation (ICMTMA) (pp. 331-339). IEEE.

Zhu, L., Wang, J. X., Dai, S., & Wu, J. Y. (2023). A phase sequence optimization method oriented by ideal bidirectional green wave. In Advances in Urban Construction and Management Engineering (pp. 563-570). CRC Press.

KSÜ Mühendislik Bilimleri Dergisi, 26(Özel Sayı), 2023 KSU J Eng Sci, 26(Special Issue), 2023
9th Uluslararası IFS Çağdaş Matematik ve Mühendislik Konferansı Özel Sayısı
9th International IFS Contemporary Mathematics and Engineering Conference Special Issue
Araştırma Makalesi Research Article

Kahramanmaras Sutcu Imam University Journal of Engineering Sciences

Geliş Tarihi : 05.08.2023 Received Date : 05.08.2023
Kabul Tarihi : 11.10.2023 Accepted Date : 11.10.2023

ASSESSING THE EFFECT OF AGE-RELATED SENSORY INPUT CHANGES ON POSTURAL SWAY IRREGULARITY

YAŞA BAĞLI DUYUSAL DEĞİŞİKLİKLERİN POSTURAL SALINIM DÜZENSİZLİĞİ ÜZERİNDEKİ ETKİSİNİN DEĞERLENDİRİLMESİ

Veysel ALCAN[1] (ORCID: 0000-0002-7786-8591)*

[1]Tarsus University, Department of Electrical and Electronics Engineering, Tarsus, Mersin, Turkiye

*Corresponding Author: Veysel ALCAN, alcanveysel@tarsus.edu.tr

ABSTRACT

Age-related decline in sensory inputs in elderly people leads to postural instability that increases irregularity of postural sway. This study aimed to examine the effect of visual or somatosensory inputs on postural sway irregularity in the elderly by using machine learning (ML). The feature set was extracted from entropy measurements including sample, fuzzy, distribution, conditional, and permutation. Then, the variables were classified by ML including support vector machines (SVM), k-nearest neighbors (k-NN), and linear discriminant analysis (LDA) algorithms. Classification performances were compared with the confusion matrix. For the elderly, in the eyes closed condition on an unstable surface, the SVM algorithm achieved higher accuracy (77%), sensitivity (72%), specificity (85%), and precision (83%) for the cv dataset. For young, SVM also achieved high accuracy (86%), sensitivity (87%), specificity (84%), and precision (84%). For the elderly, under the eyes open on unstable surface conditions, the SVM exhibited an accuracy of 79%, sensitivity of 75%, specificity of 72%, and precision of 75%. However, for young, it did not reveal good results for both surfaces. In conclusion, the findings suggest that older people adapt their postural control mechanisms, relying more on somatosensory inputs. ML algorithms with entropy-based features can give insights into age-related differences in postural control.

Keywords: Older people, balance, postural sway, entropy, machine learning

ÖZET

Yaşlılarda duyusal girdilerde yaşa bağlı azalma, postüral dengesizliğe yol açarak postüral salınımın düzensizliğini artırır. Bu çalışma, makine öğrenimi (ML) kullanarak görsel veya somatosensoriyel girdilerin yaşlılarda postural salınım düzensizliği üzerindeki etkisini incelemeyi amaçladı. Özellik seti örnek, bulanık, dağıtım, koşullu ve permütasyon dâhil Entropi ölçümlerinden çıkarıldı. Daha sonra değişkenler, destek vektör makineleri (SVM), k-en yakın komşular (k-NN) ve doğrusal diskriminant analizi (LDA) algoritmalarını içeren ML modelleri ile sınıflandırıldı. Modellerin sınıflandırma performansları hata matrisi ile karşılaştırıldı. Yaşlılar için, stabil olmayan bir yüzeyde gözleri kapalı durumda SVM algoritması test veri seti için daha yüksek doğruluk (%77), duyarlılık (%72), özgüllük (%85) ve kesinlik (%83) elde etti. Gençler içinde SVM yüksek doğruluk (%86), duyarlılık (%87), özgüllük (%84) ve kesinlik (%84) elde etti. Kararsız yüzey koşullarında gözleri açık olan yaşlılar için SVM %79 doğruluk, %75 duyarlılık, %72 özgüllük ve %75 kesinlik sergiledi. Ancak gençler için her iki yüzeyde de iyi sonuçlar ortaya çıkmadı. Sonuç olarak, bulgular yaşlı insanların postüral kontrol mekanizmalarını somatosensör girdilere daha fazla güvenerek uyarladıklarını göstermektedir. Entropi tabanlı özellik setine sahip ML algoritmaları, yaşlılarda postüral salınım dinamiklerini yöneten temel mekanizmalar hakkında fikir verebilir.

ToCite: ALCAN, V., (2023). ASSESSING THE EFFECT OF AGE-RELATED SENSORY INPUT CHANGES ON POSTURAL SWAY IRREGULARITY. *Kahramanmaraş Sütçü İmam Universitesi Mühendislik Bilimler Dergisi*, 26(Özel Sayı), 1109-1120.

Anahtar Kelimeler: Yaşlı insanlar, denge, postüral salınım, entropi, makine öğrenimi

INTRODUCTION

The human body's ability to maintain an upright stance and navigate through its environment is facilitated by a sophisticated balance system, which plays a fundamental role in performing daily activities. To achieve and sustain postural stability, the human body relies on the intricate interplay of three key sensory systems including the visual, vestibular, and proprioceptive systems (Peterka, 2018). These systems converge their sensory inputs, and through a highly coordinated motor output, form a feedback mechanism essential for maintaining precise balance control. Each of these systems possesses unique anatomical and functional features, collectively contributing to the body's perception of spatial orientation and movement. The visual system, encompassing the eyes as the primary sensory organs, along with relevant parts of the central nervous system, plays a pivotal role in postural stability (Maurer et al., 2006). The vestibular system consists of the semicircular canals and otolith organs, which are mainly responsible for detecting angular accelerations and linear accelerations, respectively. The somatosensory system, encompassing various sensory receptors, plays a vital role in providing the body with information about its position and movement in space (Mergner et al., 2005). This intricate system includes cutaneous receptors, joint receptors, muscle spindles, and Golgi tendon organs, each serving unique functions. Understanding the integration and interactions of these sensory inputs is of paramount importance in comprehending the mechanisms underlying postural sway and balance control, particularly in the context of aging populations and related issues such as fall risk in the elderly because the aging process is an inevitable facet of the human life cycle, bringing with it a myriad of physiological, sensorial, and functional changes (Horak et al., 1989). Decrease or deterioration in sensory inputs in elderly people leads to balance problems that increase the risk of falling, which can have severe consequences for the health and independence of older individuals (Qiu et al., 2012). Analysis of postural sway, defined as the involuntary movement of the body while maintaining an upright stance, has been a critical indicator of balance and postural control.

In literature, many studies have revealed an in-depth investigation into the interplay of visual, vestibular, and somatosensory inputs in postural sway dynamics (Horak et al., 1989; Mergner et al., 2005; Qiu et al., 2012; Wang et al., 2010). Qui et al. (2012) examined the integration of visual and somatosensory inputs affects postural sway and balance, with reliance on somatosensory information increasing when visual input was limited. They suggested that textured insole surfaces could reduce postural sway in older people, particularly during more challenging balance tasks, providing an important intervention in fall prevention. They found clear differences in postural sway based on age, insole surface, and standing surface and significant interaction for various postural sway measures. Wang et al. (2010) found that visual inputs significantly affected postural sway and balance, particularly when combined with an unstable base of support. Their results revealed that visual information impacted postural reactions and sway responses. Postural response amplitudes depended on visual field velocity. Tanaka & Uetake (2005) found that older adults had increased postural sway on a foam surface compared to a firm surface, regardless of age. The findings of their study revealed that among older adults, there is an increased dependence on visual cues for correcting M-L postural sway. Moreover, the deterioration in visual acuity associated with aging could potentially heighten the susceptibility to sideways falls, especially in demanding conditions, such as when standing on unstable surfaces. This underscores the significance of visual function assessment in the context of fall prevention strategies for the elderly. Garbus et al. (2019) investigated how visual and somatosensory inputs interact to improve postural sway and balance. They suggested that providing explicit visual feedback of the center of pressure does not increase the light touch effects on the postural sway, and the importance of the implicit somatosensory information on postural control is discussed. Ito et al. (2020) reported that elderly individuals were more dependent on somatosensory signals for balance control than adults.

Previous studies indicate that there is no consensus on the dominant effects of visual and/or somatosensory inputs on postural control and balance due to aging. Moreover, postural sway has been traditionally assessed through simple biomechanical metrics, such as center of pressure (COP) displacement and velocity, in particular using linear or statistical signal analysis approaches. However, these conventional measures may not fully capture the complexity of postural control mechanisms, especially in dynamic real-life situations. Instability or irregularity of postural sway could be associated with an increased risk of falls (Seigle et al., 2009). The irregularity can be measured by nonlinear methods rather than linear or statistical approaches. Employing a nonlinear approach, it can integrate findings from neurophysiology, biomechanics, and machine learning (ML) to gain comprehensive insights into the complexity of human balance control. In recent years, entropy measurements have been used as a very popular method for

measuring irregularity and complexity in time series (Alcan, 2022). By leveraging advancements in nonlinear signal analysis capabilities, it is needed to shed further light on the mechanisms governing postural stability in older people. Furthermore, advancements in ML algorithms have been considered useful clinical decision support tools for investigating postural sway dynamics and analyzing intricate patterns within large datasets. Therefore, this study aimed to present the results of an in-depth investigation into the impact of sensory inputs on the entropy of postural sway in the elderly, utilizing ML techniques. Specifically, the study focused on various entropy algorithms and the application of support machine vectors (SVM), k-nearest neighbors (k-NN), and partial least squares discriminant analysis (PLS-DA) algorithms to decipher the complex interactions between sensory inputs and postural sway patterns in older people

METHODS

Data

The present study used a public dataset that recruited a cohort of elderly participants, who underwent comprehensive assessments of postural sway under four sensory conditions including eyes-open, eyes-closed, stable surface, and unstable surface (Santos & Duarte, 2016). Postural sway data were collected using advanced force plate technology in anterior-posterior (A-P) and medial–lateral (M-L) directions, allowing for precise measurements of COP displacement in response to sensory perturbations.

Entropy Algorithms

Based on entropy algorithms, the feature set was built with six well-known entropy algorithms to conduct postural sway changes of older people in A-P and M-L directions.

Sample entropy (SampEn):

SampEn is a measure used to quantify the complexity or irregularity of time series data. It compares the likelihood of repeated patterns of a certain length in the data. Sample entropy builds upon approximate entropy and involves counting matches of templates in the time series data (Richman & Moorman, 2000). The mathematical equations and backgrounds for SamEn are explained in Equation 1.

$$SampEn\ (m,\tau,r) = -\ln\frac{\sum_{i=1}^{N-m\tau} A_i^{(m+1)}(d,r)}{\sum_{i=1}^{N-m\tau} A_i^{(m)}(d,r)} \quad (1)$$

Fuzzy Entropy (FuzzyEn)

FuzzyEn measures the spread or dispersion of membership degrees within the fuzzy set (Chen et al., 2009). Unlike SampEn, the average number of vectors Xm(j) that are within "r" of Xm(i) is used with the average degree of membership. The specific mathematical equations for the membership function and FuzzyEn are calculated in Equation 2 and Equation 3.

$$A_i^{(m)}(d,r) = \sum_{j=1,j\neq i}^{N-m\tau} e^{-\ln(2)(^{d_{i,j}}/_{r})^2} \quad (2)$$

$$membership\ function = e^{-\ln 2(^{x}/_{r})^2} \quad (3)$$

Conditional Entropy (CE)

CE is a measure of the amount of uncertainty or information content in a random variable given the knowledge of another random variable. It quantifies the remaining uncertainty in one variable after the other variable is observed (Porta et al., 1998). CE is calculated as the average entropy of the conditional probability distribution of the first variable given the second variable. Mathematically, for two discrete random variables, CE is calculated by Equation 4.

$$CE(m,\tau) = SE(z_j) - SE(w_i) + perc(m)SE \quad (4)$$

where the summation is performed over all possible values of X and Y.

Distribution Entropy (DistEn)

DistEn is a measure that quantifies the diversity or variability in the probability distribution of a random variable (Li et al., 2016). It captures the dispersion of the probability density function of the distance matrix by the histogram approach with a fixed bin number of B. The mathematical equations for DistEn are calculated by Equation 5.

$$DistEn\ (m,\tau,B) = -\frac{1}{log_2(B)}\sum_{t=1}^{B} p_t \log_2(p_t) \quad (5)$$

where p_t is the probability of each bin

Permutation Entropy (PermEn)

PermEn is based on the idea of permuting the values of a time series and analyzing the resulting patterns (Bandt & Pompe, 2002). It quantifies the probability distribution of ordinal patterns (sequences of values' ranks) within the time series as follows:

$$PermEn\ (m,\tau) = -\frac{1}{log_2 m!}\sum_{j=1}^{m!} p_t(m,\tau) \log_2[(p_j(m,\tau)] \quad (6)$$

Machine Learning Algorithms

To investigate the intricate relationship between sensory inputs and postural sway patterns, the most common ML algorithms including SVM, k-NN, and LDA were applied to model the complex interactions within the data. These supervised ML algorithms were chosen for classification tasks and their ability to handle high-dimensional data and nonlinear relationships, makes them well-suited for the analysis of postural sway dynamics. Samples were usually divided into training dataset and cross-validation (CV) as a testing dataset based on the Venetian blinds approach. A 5-fold CV value was used for internal validation of all models.

Support Vector Machines (SVM)

SVMs aim to find an optimal hyperplane that separates the data points of different classes with the largest margin. The mathematical foundation of SVM relies on the concept of a maximum-margin hyperplane and the use of kernel functions for handling nonlinearly separable data. The basic idea is to transform the input data into a higher-dimensional space using a kernel function and then find the hyperplane that maximizes the margin between classes. The optimization problem in SVM involves finding the hyperplane parameters that minimize the classification error and maximize the margin. Popular kernel functions used in SVM include linear, polynomial, gaussian, and sigmoid kernels.

K-Nearest Neighbor (k-NN)

In k-NN, the class or value of an unknown sample is determined based on the majority vote or averaging of the values of its k nearest neighbors in the training data. The mathematical background of k-NN involves computing the distances between data points to identify the k-nearest neighbors. The choice of distance metric, such as Euclidean distance or Manhattan distance, plays a crucial role in the k-NN algorithm. For classification tasks, k-NN assigns the class label based on the majority class among the k nearest neighbors. For regression tasks, k-NN takes the average or weighted average of the target values of the k nearest neighbors to estimate the unknown sample's value.

Linear Discriminant Analysis (LDA)

LDA is a supervised classification and dimensionality reduction technique that seeks to find linear discriminants to maximize the separability between classes. It can be used for classification tasks when the class structure is important and is a useful tool for feature extraction and dimensionality reduction in supervised learning scenarios. Concerning principal component analysis, LDA can provide a two-step approach to first reduce dimensionality and then maximize class separability for improved classification performance.

Classification Performance of ML Algorithms

To evaluate the classification performances (in training and cross-validation test sets of samples), a confusion matrix was provided. From the confusion matrix, several important metrics were calculated, including precision, sensitivity (recall), and specificity. A confusion matrix is a square matrix with dimensions “NxN+1”, where N is the number of

classes. It summarizes the true positive (TP), false positive (FP), true negative (TN), and false negative (FN) predictions made by a classification model, where TP is the number of correctly predicted positive samples, FP is the number of samples wrongly predicted as positive (actually negative), TN is the number of correctly predicted negative samples, and FN is the number of samples wrongly predicted as negative (actually positive). Precision indicates the proportion of correctly predicted positive samples among all samples predicted as positive by Precision = TP/(TP+FP). Sensitivity (recall) measures the proportion of correctly predicted positive samples among all actual positive samples. It assesses positive samples correctly by sensitivity = TP/(TP+FN). Specificity measures the proportion of correctly predicted negative samples among all actual negative samples. It assesses negative samples correctly by specificity = TN/(TN+FP). Accuracy measures the overall proportion of correct predictions made by the model, considering both positive and negative instances by accuracy = (TP+TN)/(TP+TN+FP+FN).

RESULTS

The classification performance of the SVM, k-NN, and LDA algorithms was evaluated by using a confusion matrix. Table 1 shows the overall accuracy of the models for older subjects.

Table 1. The overall accuracy of the ML algorithms for older subjects

Overall Accuracy for Older Subject							
		SVM		k-NN		LDA	
Eyes Condition	Class	Training (%)	CV (%)	Training (%)	CV (%)	Training (%)	CV (%)
Eyes Open	Stable Surface	82	79	78	73	83	79
	Unstable Surface						
Eyes Closed	Stable Surface	82	77	70	72	79	77
	Unstable Surface						

Concerning the older subjects, the overall accuracy of the SVM model was 82% and 79% for training and CV data, respectively, under eyes-open conditions while 82% and 77% for training and CV data under eyes-closed conditions, respectively. The overall accuracy of the k-NN model was 78% and 73% for training and CV data respectively, under eyes-open conditions while 70% and 72% for training and CV data under eyes-closed conditions, respectively. For the LDA algorithm, the overall accuracy was 83% and 79% for training and CV data respectively, under the eyes-open condition while 79% and 77% for training and CV data under the eyes-closed condition, respectively. These results indicated that the SVM model revealed a better performance than k-NN and LDA models in overall predictive accuracy. Table 2 shows the overall accuracy of the models for young subjects.

Table 2. The overall accuracy of the ML algorithms for young subjects.

Overall Accuracy for Young Subject							
		SVM		kNN		LDA	
Eyes Condition	Class	Training (%)	CV (%)	Training (%)	CV (%)	Training (%)	CV (%)
Eyes Open	Stable Surface	70	64	66	71	80	74
	Unstable Surface						
Eyes Closed	Stable Surface	88	86	87	86	85	86
	Unstable Surface						

In Table 2, the overall accuracy of the SVM model was 70% and 64% for training and CV data, respectively, under eyes-open conditions while 88% and 86% for training and CV data under eyes-closed conditions, respectively. The overall accuracy of the k-NN model was 66% and 71% for training and CV data under eyes-open conditions, respectively. On the other hand, it was 87% and 86% for training and CV data under eyes-closed conditions, respectively. For the LDA algorithm, the overall accuracy was 80% and 74% for training and CV data, respectively, under eyes-open conditions while 85% and 86% for training and CV data under eyes-closed conditions, respectively. These results indicated that the SVM model also revealed a better performance than k-NN and LDA models in overall predictive accuracy.

To understand the classifier's confidence in its predictions and assess its performance, the probability graphs were produced by SVM algorithms shown in Figure 1 and Figure 2. Each point on the graph represents a sample, and its corresponding probability estimate is on the y-axis. These graphs are often used in binary classification tasks, where the SVM model assigns labels +1 and -1 to the two classes and tries to maximize the margin between the support vectors (data points closest to the decision boundary). Figure 1 shows the probability graphs for older subjects.

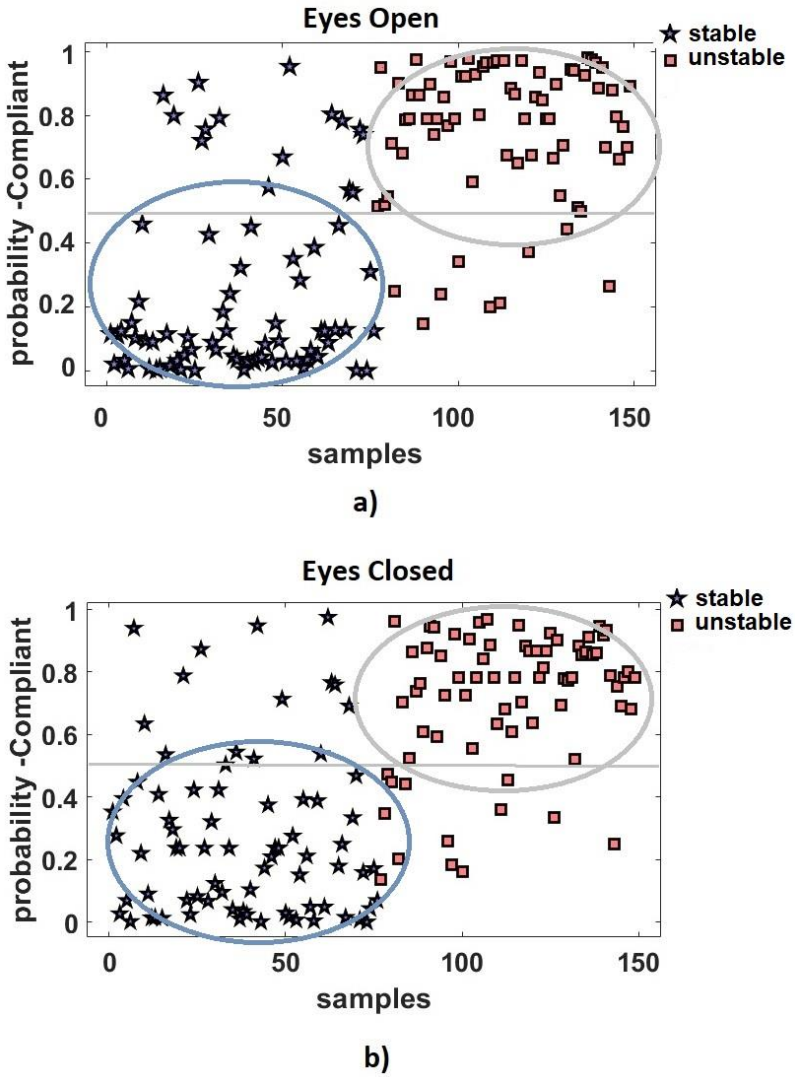

Figure 1. The Probability Graphs For Older Subjects. The Relationship Between The SVM's Probability Estimates And The Samples Used In Stable Vs Unstable Evaluation Under a) Eyes-Open Condition b) Eyes-Closed Condition.

In Figure 1a, most samples of the unstable class have high probabilities (close to 1), while samples of the stable class have low probabilities (close to 0), which indicates that the SVM is effectively distinguishing between the classes. A tight cluster of probabilities around 0.5 for the samples indicates that the SVM is uncertain about their classification. On the other hand, Figure 1b indicates that SVM does not perfectly distinguish between the classes. Fewer samples of unstable and stable classes have high and low probabilities (close to 1 or 0), respectively. Figure 2 shows the probability graphs for young subjects.

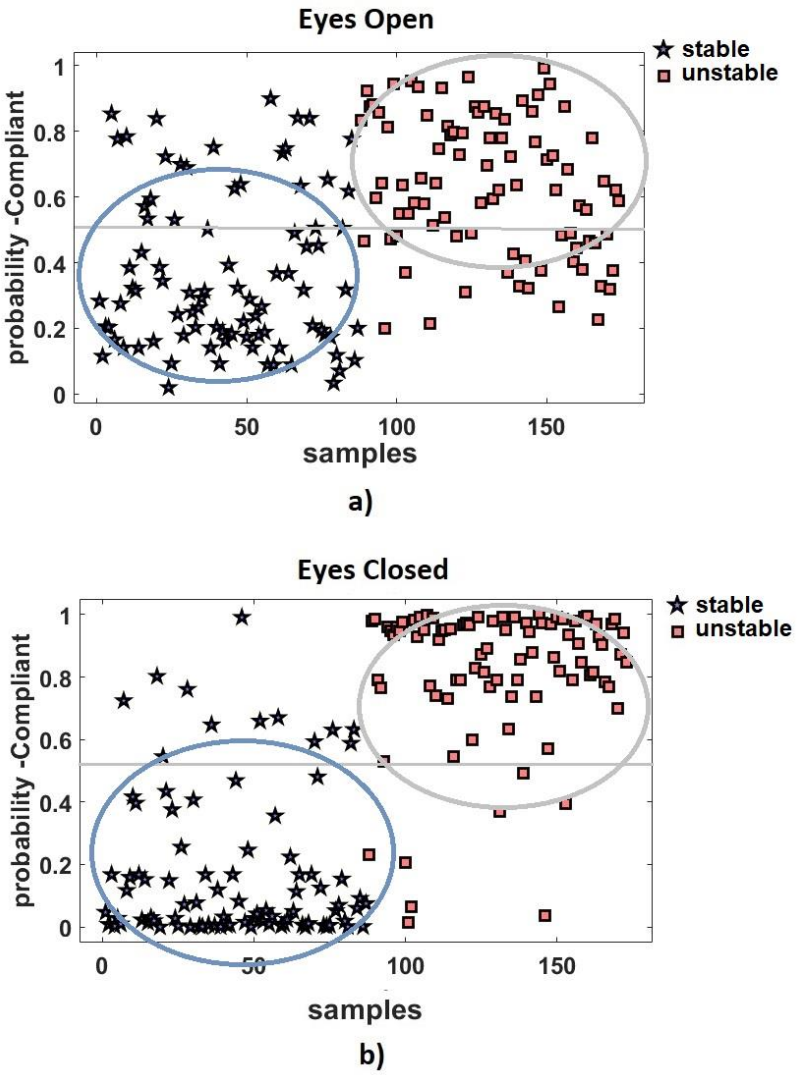

Figure 2. The Probability Graphs For Young Subject. The Relationship Between The SVM's Probability Estimates And The Samples Used In Stable Vs Unstable Evaluation Under a) Eyes-Open Condition b) Eyes-Closed Condition.

In Figure 2a, a larger cluster of probabilities around "0.5" for the samples indicates that the SVM is uncertain about their classification. Fewer samples of the unstable class have high probabilities (close to 1), while fewer samples of the stable class have low probabilities (close to 0). In Figure 2b, most samples of unstable and stable classes have a high and low probability, respectively. The graph results indicate that the SVM better distinguished between stable and unstable classes under eyes-closed condition compared to eyes-open condition.

Table 3 shows confusion matrix metrics for older subjects. When compared to the ML models, the SVM model exhibited also better sensitivity (recall), specificity, and precision values than k-NN and LDA models, indicating its capability to correctly identify true positive samples for both training and CV data sets.

Table 3. Confusion Matrix Metrics For Evaluating The Performance Of Classification ML Algorithms For Older Subjects

			SVM			k-NN			LDA		
		Class	Sens %	Spec %	Prec %	Sens %	Spec %	Prec %	Sens %	Spec %	Prec %
Training	Eyes Open	Stable	75	89	88	64	92	89	78	90	89
		Unstable	89	75	77	92	64	71	90	78	80
	Eyes Closed	Stable	82	82	83	55	86	81	68	86	84
		Unstable	82	82	81	86	55	65	86	68	72
CV	Eyes Open	Stable	72	85	83	55	92	88	76	88	87
		Unstable	85	72	75	92	55	66	88	76	78
	Eyes Closed	Stable	76	77	77	66	66	66	67	84	81
		Unstable	77	76	76	66	66	66	84	67	71

CV=cross-validation; SVM=support vector mechines; k-NN=k-nearest neighbors; LDA=linear discriminant analysis; Sens= sensitivity; Spec= specificity; Prec=precision

Concerning older subjects, under eyes-open conditions, the SVM algorithm generally achieved higher sensitivity (89% and 85%), specificity (75% and 72%), and precision (77% and 75%) for unstable surfaces in both training and CV datasets, respectively. For stable surfaces, the SVM algorithm revealed high sensitivity (75% and 72%), specificity (89% and 85%), and precision (88% and 83%) in training and CV datasets, respectively. SVM revealed also similarly good results for the eyes-closed condition in both stable and unstable surfaces. Table 4 shows confusion matrix metrics for young subjects.

Table 4. Confusion Matrix Metrics For Evaluating The Performance Of Classification ML Algorithms For Young Subjects

			SVM			k-NN			LDA		
		Class	Sens %	Spec %	Prec %	Sens %	Spec %	Prec %	Sens %	Spec %	Prec %
Training	Eyes Open	Stable	74	67	69	48	84	75	75	85	83
		Unstable	67	74	72	84	48	62	85	75	77
	Eyes Closed	Stable	84	92	91	86	87	87	82	88	88
		Unstable	92	84	85	87	86	86	88	82	83
CV	Eyes Open	Stable	68	61	63	53	90	84	70	77	75
		Unstable	61	68	65	90	53	66	77	70	72
	Eyes Closed	Stable	84	87	87	84	87	87	84	87	87
		Unstable	87	84	84	87	84	84	87	84	84

CV=cross-validation; SVM=support vector mechines; K-NN=k-nearest neighbors; LDA=linear discriminant analysis; Sens= sensitivity; Spec= specificity; Prec=precision

Concerning young subjects, under eyes-closed conditions, the SVM algorithm achieved higher sensitivity (92% and 87%), specificity (84% and 84%), and precision (85% and 84%) for unstable surfaces in both training and CV datasets, respectively. For stable surfaces, the SVM algorithm revealed high sensitivity (84% and 84%), specificity (92% and 87%), and precision (91% and 87%) in training and CV datasets, respectively. However, it did not reveal good results for eyes-open conditions in both stable and unstable surfaces.

DISCUSSION

The primary objective of this study was to evaluate the relationship between visual and somatosensory inputs and the entropy of postural sway in elderly individuals. Secondly, it was aimed to assess the efficacy of ML algorithms (SVM k-NN, and LDA) in analyzing postural sway patterns and identifying potential predictors of postural stability. Four sensory conditions involved altered visual inputs (eyes open and eyes closed) and somatosensory manipulations (stable and unstable surfaces) to simulate real-life scenarios where sensory challenges may lead to balance disturbances. In the present study, the results of the classification of postural sway entropy features suggested valuable insights into the effects of age on postural control.

Age-Related Visual And Somatosensory Effect On Postural Sway

The young subjects indicated a high rate of classification accuracy, sensitivity, specificity, and precision, particularly in conditions with eyes closed and on unstable surfaces. However, they exhibited a lower rate of performance when their eyes were open, suggesting that visual input and stable surface significantly contributed to decreased irregularity of postural sway in young or vice versa. In contrast, the older subjects exhibited similar rates of accuracy, sensitivity, specificity, and precision in postural sway classification on both stable and unstable surfaces, regardless of whether their eyes were open or closed. This suggests that the postural control mechanisms in the elderly remain relatively consistent across different sensory conditions. The observed differences in classification performance between the older and the young subjects can be attributed to changes in sensory processing with age. Age-related physiological changes can affect the sensory systems of older people, including the visual and somatosensory systems. The lower classification performance in young subjects with their eyes open could indicate that reliance on visual input decreases with age. This could be due to age-related declines in visual acuity and processing speed. As a result, young individuals might experience difficulty maintaining balance solely with visual input, especially in challenging conditions like standing on unstable surfaces. On the other hand, the consistent performance of older people across different sensory conditions suggests that they might rely more on somatosensory inputs for postural control. The somatosensory system, which includes sensory information from the feet and proprioceptive receptors, plays a crucial role in balance maintenance. The results showed that stability gains were observed with increasing sensory information, but the nature of these gains was modulated by somatosensory (proprioceptive) information and the reliability of the haptic support surface. Additionally, the perception of somatosensation was influenced by congruent and incongruent visual inputs and body posture, with better localization observed when visual inputs and body posture were congruent with somatosensation. With aging, the somatosensory system might become more important in compensating for visual deficits and maintaining postural stability. These findings suggest that somatosensory inputs play important roles in postural control and can affect balance (Wiesmeier et al., 2015). It was found that older subjects favor proprioceptive than younger subjects do, and parameter differences between young and old may result from both deficits and compensation strategies in the elderly. The main reason can be related to impairments of the motor system in older people who can have difficulties in sensory reweighting, which is the process of scaling the relative importance of sensory cues (visual, vestibular, and proprioceptive) for motor control (Horak et al., 1989).
In this study, standing on an unstable surface reduced the reliability of somatosensory information and increased the entropy of postural sway. With aging, older subjects can have a lower sensitivity to the plantar surface of the foot than younger subjects, which can increase postural sway. These age-related effects may be further magnified in conditions where visual input is eliminated, leading to heightened dependence on somatosensory information (Lord et al., 1991; Patel et al., 2011).

Entropy and ML Algorithms

Age-related differences in spontaneous sway mainly concern an increased postural sway (mean velocity, sway, mean frequency, etc.) by using traditional CoP analysis (Barela et al. 2018). However, in this study, measures of postural control were segregated into spontaneous sway entropy measures of motor behavior induced by surface perturbations. While removing visual feedback affects postural control in young people leading to changes in the dynamics of postural oscillations by increased entropy, it did not affect older people. On the contrary, for older subjects, manipulating somatosensory feedback led to changes in the dynamics of postural oscillations by increased entropy suggesting somatosensory had a dominant effect on the postural sway oscillations. Concerning unstable surface conditions under both eyes open-and-closed conditions, the results showed that the irregularity of postural sway was higher in older subjects than in young subjects. For older subjects, the balance was less stable with absent somatosensory information. Sensory inputs to the somatic system can decrease with age, which can contribute to increased irregularity (entropy) postural sway in older subjects compared to young (Shiota, 2015).

In previous studies, Alcan (2023) calculated entropy measurements including SampEn, FuzzyEn, DistEn, CE, PermEn, and sparse density entropy from CoP data. SVM and k-NN ML algorithms were used to investigate the effect of visual or somatosensory inputs on CoP signal in solely the elderly. This study found that the measurement of CoP irregularity or nonlinear dynamics in balance assessments in the elderly was more sensitive to somatosensory inputs than visual inputs. Similarly, Hansen et al. (2017) found that entropy measures were more sensitive in analyzing postural sway compared to traditional measures. They used SampEn, multi-scale sample entropy (MSE), and multivariate multi-scale entropy and compared them to traditional measures of COP variability. Their results suggested that non-linear methods appear to be an additional valuable tool for analysis of the dynamics of posture

especially when applied to incremental time series when compared to the classical parameters and entropy measures of the original time series. Giovanini et al. categorized age groups using different CoP time series. They used the same data as the dataset. However, they calculated large feature sets including temporal, spatial, spectral, and nonlinear features including mean distance, root mean square (RMS) distance, mean velocity, RMS velocity, standard deviation (SD) of velocity), sway path, length of COP path, excursion area, total mean velocity, mean frequency, median frequency, spectral power with 95%), SampEn, MSE, scaling exponent, Hurst exponent of distance. They used SVMs, k-NN, NB MLP, RF, and decision tree (DT) ML models and found that a 60 s sampling duration provided the most discriminative information. The overall classification accuracy of all ML models was 61.3% for dataset 1 and 67.8% for dataset 2. The mean values of all ML models were smaller for a 30 s duration, affecting the CoP time series duration in different age groups. Çetin & Bilgin (2019) distinguished between young and aged groups using the same dataset. Unlike our feature set, they extracted features from time-dependent variables including CoP and force change. They used various classifiers and found that force signals were more successful than COP signals. The SVM model had the highest accuracy (81.67%) in separating the young and older groups. Seigle et al. (2009) concluded that classical stabilometric variables and Recurrence Quantification Analysis (RQA) outputs provided complementary information for the characterization of aging effects on postural sway. They found that COP displacement was affected by vision in both young and elderly adults. The RQA method was able to discriminate COP displacement in elderly subjects. Ojle et al. (2021) investigated the effects of visual and somatosensory input on postural sway using entropy and ML algorithms. They used the k-NN model to investigate the effects of the visual, proprioceptive, and vestibular systems using the postural sway information in the M-L and A-P directions. They found that the visual system affected M-L sway, and proprioceptive and vestibular systems affected A-P sway. A-P sway was more affected by sensory systems than M-L sway. Sun et al. (2019) implemented an ML approach to assess the accuracy and feature importance of various postural sway metrics to differentiate individuals with Multiple Sclerosis (MS) from healthy controls as a function of physiological fall risk and M-L sway amplitude was identified as the strongest predictor for fall risk groupings. The feature set used in this study consisted of 20 common postural sway metrics derived from static posturography assessment. The ML algorithm used in this study was random forest (RF) with 10-fold cross-validation. The sway-metric-based RF classifier had high accuracy in discriminating controls from MS individuals (>86%). Sway sample entropy was identified as the strongest feature for the classification of low-risk MS individuals from healthy controls. Whereas for all other comparisons, mediolateral sway amplitude was identified as the strongest predictor for fall risk groupings. They found that posturography was beneficial for balance impairment and fall risk assessment in individuals with MS. Sample entropy and M-L sway amplitude were strong predictors for fall risk in MS individuals. Lee et al. (2020) found that using logistic regression analysis with sensor data and entropy analysis provided an accurate classification of fall risk in elderly people. Their results showed that logistic regression analysis predicted fall risk in the elderly and PerEn and statistical features provided accurate classification.

Consequently, the findings of the present study are consistent with previous research on age-related changes in postural sway and suggest the use of such entropy indices from nonlinear domains extracted from CoP signals and its complex components as potential markers for postural instability and fall risk in older adults. ML algorithms also provided complementary information and very good classification performance for the characterization of aging effects on postural sway. From a clinical perspective, the ML approach of applying entropy analysis to CoP data on a fall-risk scale can allow medical practitioners to predict risk and can provide decision-makers with a more accurate way to classify fall risk in elderly people.

CONCLUSION

This study found how visual and somatosensory information significantly affects the postural sway irregularity (balance ability) of older people, as measured by nonlinear dynamics by entropy. The findings suggest that older people adapt their postural control mechanisms, relying more on somatosensory inputs, to maintain stability. Meanwhile, young individuals heavily rely on visual input, particularly in challenging situations. Findings suggest the loss of somatosensory function may explain much of the age-related increase in the irregularity of postural sway, with different entropy algorithms measured with eyes closed then eyes open on foam, and then a firm surface. For clinical decision support systems, the SVM algorithms can give insights into the underlying mechanisms that govern postural sway dynamics in the elderly population, shedding light on the role of sensory inputs in maintaining balance. The findings of this study have the potential to enhance preventive measures and interventions aimed at improving postural stability and reducing fall-related incidents, thereby contributing to the well-being and quality of life of the elderly population and society at large.

Acknowledge
I would like to acknowledge the support and collaboration provided by COST Action CA 20104 PhysAgeNet during this research.

REFERENCES

Alcan, V. (2022). Nonlinear Analysis of Stride Interval Time Series in Gait Maturation Using Distribution Entropy. IRBM, 43(4), 309-316. https://doi.org/10.1016/j.irbm.2021.02.001.

Alcan, V. (2023, July). Evaluation Of The Effects Of Visual And Somatosensory Inputs On Balance In The Elderly By Usıng Machine Learning. In 2023 th International IFS and Contemporary Mathematics and Engineering Conference(IFSCOM-E 2023) (pp.223)

Bandt, C., & Pompe, B. (2002). Permutation entropy: a natural complexity measure for time series. Physical review letters, 88(17), 174102. https://doi.org/10.1103/PhysRevLett.88.174102

Barela, A. M. F., Caporicci, S., de Freitas, P. B., Jeka, J. J., & Barela, J. A. (2018). Light touch compensates for peripheral somatosensory degradation in postural control of older adults. *Human movement science*, *60*, 122–130.

Chen, W., Zhuang, J., Yu, W., & Wang, Z. (2009). Measuring complexity using FuzzyEn, ApEn, and SampEn. *Medical engineering & physics*, *31*(1), 61–68. https://doi.org/10.1016/j.medengphy.2008.04.005

Cetin, E., &Bilgi,n S. (2019) Investigating effects of force and pressure center signals on stabilogram analysis. *IET Science Measurement &Technology*, 13(9): 1305– 1310. https://doi.org/10.1049/iet-smt.2019.0078

Garbus, R. B. S. C., Alouche, S. R., Prado-Rico, J. M., Aquino, C. M., & Freitas, S. M. S. F. (2019). From One to Two: Can Visual Feedback Improve the Light Touch Effects on Postural Sway? *Journal of Motor Behavior*, *51*(5), 532–539. https://doi.org/10.1080/00222895.2018.1528201

Giovanini, L.H.F., Manffra, E.F., & Nievola, J.C. (2018). Discriminating Postural Control Behaviors from Posturography with Statistical Tests and Machine Learning Models: Does Time Series Length Matter? In: Shi, Y., et al. Computational Science – ICCS 2018. ICCS 2018. *Lecture Notes in Computer Science*, 10862, 350–357. https://doi.org/10.1007/978-3-319-93713-7_28

Hansen, C., Wei, Q., Shieh, J. S., Fourcade, P., Isableu, B., & Majed, L. (2017). Sample Entropy, Univariate, and Multivariate Multi-Scale Entropy in Comparison with Classical Postural Sway Parameters in Young Healthy Adults. *Frontiers in human neuroscience*, *11*, 206. https://doi.org/10.3389/fnhum.2017.00206

Horak, F. B., Shupert, C. L., & Mirka, A. (1989). Components of postural dyscontrol in the elderly: a review. *Neurobiology of aging*, *10*(6), 727–738. https://doi.org/10.1016/0197-4580(89)90010-9

Ito, T., Sakai, Y., Nishio, R. Yohei, I., Kazunori Y., & Yoshifumi M. (2020). Postural Sway in Adults and Elderly Individuals During Local Vibratory Stimulation of the Somatosensory System. SN Compr. Clin. Med. 2, 753–758.

Lee, C. H., Chen, S. H., Jiang, B. C., & Sun, T. L. (2020). Estimating Postural Stability Using Improved Permutation Entropy via TUG Accelerometer Data for Community-Dwelling Elderly People. *Entropy (Basel, Switzerland)*, *22*(10), 1097. https://doi.org/10.3390/e22101097

Li, P., Li, K., Liu, C., Zheng, D., Li, Z. M., & Liu, C. (2016). Detection of Coupling in Short Physiological Series by a Joint Distribution Entropy Method. *IEEE Transactions on Bio-Medical Engineering*, *63*(11), 2231–2242. https://doi.org/10.1109/TBME.2016.2515543

Lord, S. R., Clark, R. D., & Webster, I. W. (1991). Postural stability and associated physiological factors in a population of aged persons. *Journal of Gerontology*, *46*(3), M69–M76. https://doi.org/10.1093/geronj/46.3.m69

Maurer, C., Mergner, T., & Peterka, R. J. (2006). Multisensory control of human upright stance. *Experimental brain research*, *171*(2), 231–250. https://doi.org/10.1007/s00221-005-0256-y

Mergner, T., Schweigart, G., Maurer, C., & Blümle, A. (2005). Human postural responses to motion of real and virtual visual environments under different support base conditions. *Experimental brain research*, *167*(4), 535–556. https://doi.org/10.1007/s00221-005-0065-3

Ojie, O. D., & Saatchi, R. (2021). Kohonen Neural Network Investigation of the Effects of the Visual, Proprioceptive, and Vestibular Systems to Balance in Young Healthy Adult Subjects. *Healthcare (Basel, Switzerland)*, *9*(9), 1219. https://doi.org/10.3390/healthcare9091219

Patel, M., Fransson, P. A., Johansson, R., & Magnusson, M. (2011). Foam posturography: standing on foam is not equivalent to standing with decreased rapidly adapting mechanoreceptive sensation. *Experimental brain research*, *208*(4), 519–527. https://doi.org/10.1007/s00221-010-2498-6

Peterka R. J. (2018). Sensory integration for human balance control. *Handbook of Clinical Neurology*, *159*, 27–42. https://doi.org/10.1016/B978-0-444-63916-5.00002-1

Porta, A., Baselli, G., Liberati, D., Montano, N., Cogliati, C., Gnecchi-Ruscone, T., Malliani, A., & Cerutti, S. (1998). Measuring regularity using a corrected conditional entropy in sympathetic outflow. *Biological cybernetics*, *78*(1), 71–78. https://doi.org/10.1007/s004220050414

Qiu, F., Cole, M. H., Davids, K. W., Hennig, E. M., Silburn, P. A., Netscher, H., & Kerr, G. K. (2012). Enhanced somatosensory information decreases postural sway in older people. *Gait & posture*, *35*(4), 630–635. https://doi.org/10.1016/j.gaitpost.2011.12.013

Richman, J. S., & Moorman, J. R. (2000). Physiological time-series analysis using approximate entropy and sample entropy. *American journal of physiology. Heart and circulatory physiology*, *278*(6), H2039–H2049. https://doi.org/10.1152/ajpheart.2000.278.6.H2039

Santos, D.A., & Duarte, M. (2016) A public data set of human balance evaluations. *PeerJ*, 4:e2648. https://doi.org/10.7717/peerj.2648

Seigle, B., Ramdani, S., & Bernard, P. L. (2009). Dynamical structure of the center of pressure fluctuations in elderly people. *Gait & posture*, *30*(2), 223–226. https://doi.org/10.1016/j.gaitpost.2009.05.005

Shiota, K. (2015). Influence of Aging on Postural Control in Terms of Sensory Movements. In: Kanosue, K., Oshima, S., Cao, ZB., Oka, K. (eds) Physical Activity, Exercise, Sedentary Behavior and Health. Tokyo: Springer.

Sun, R., Hsieh, K. L., & Sosnoff, J. J. (2019). Fall Risk Prediction in Multiple Sclerosis Using Postural Sway Measures: A Machine Learning Approach. *Scientific reports*, *9*(1), 16154. https://doi.org/10.1038/s41598-019-52697-2

Tanaka, H., & Uetake, T. (2005). Characteristics of postural sway in older adults standing on a soft surface. *Journal of Human Ergology*, *34*(1-2), 35–40.

Wang, Y., Kenyon, R. V., & Keshner, E. A. (2010). Identifying the control of physically and perceptually evoked sway responses with coincident visual scene velocities and tilt of the base of support. *Experimental brain research*, *201*(4), 663–672. https://doi.org/10.1007/s00221-009-2082-0

WMeier, I. K., Dalin, D., & Maurer, C. (2015). Elderly Use Proprioception Rather than Visual and Vestibular Cues for Postural Motor Control. *Frontiers in aging neuroscience*, *7*, 97. https://doi.org/10.3389/fnagi.2015.00097

KSÜ Mühendislik Bilimleri Dergisi, 26(Özel Sayı), 2023 KSU J Eng Sci, 26(Special Issue), 2023
9th Uluslararası IFS Çağdaş Matematik ve Mühendislik Konferansı Özel Sayısı
9th International IFS Contemporary Mathematics and Engineering Conference Special Issue
Araştırma Makalesi Research Article

Kahramanmaras Sutcu Imam University
Journal of Engineering Sciences

Geliş Tarihi : 08.08.2023 Received Date : 08.08.2023
Kabul Tarihi : 29.09.2023 Accepted Date : 29.09.2023

RELATIVE CONTROLLABILITY OF THE φ-CAPUTO FRACTIONAL DELAYED SYSTEM WITH IMPULSES

BAŞKABİR FONKSİYONA BAĞLI CAPUTO KESİRLİ ANİ DEĞİŞİMLİ GECİKMELİ SİSTEMİN GÖRECELİ KONTOL EDİLEBİLİRLİĞİ

Mustafa AYDIN[1] (ORCID: 0000- 0003-0132-9636)

[1] Van Yüzüncü Yıl Üniversitesi, Muradiye Meslek Yüksekokulu, Tıbbi Hizmetler ve Teknikler Bölümü, Van, Türkiye

*Sorumlu Yazar / Corresponding Author: Mustafa AYDIN, m.aydin@yyu.edu.tr

ABSTRACT

The impulsive fractional delayed differential system with the Caputo derivative with respect to another function is considered. An explicit solution to the system in the light of the available studies on this subject is determined and its existence and uniqueness are debated. Lastly, the stability and controllability of the given system are investigated.

Keywords: Existence uniqueness, impulsive fractional delayed system, relative controllability, Ulam-Hyers stability

ÖZET

Herhangi bir fonskiyona göre tanımlanmış Caputo türevli ani değişmeli kesirli gecikmeli bir sistem dikkate alınmaktadır. Bu konuda mevcut çalışmaların ışığında sistemin sarih bir çözümü belirlenmekte ve çözümün varlığı ve tekliği tartışılmaktadır. Son olarak, verilen sistemin kararlılığı ve kontrol edilebilirliği araştırılmaktadır.

Anahtar Kelimeler: Ani değişmeli kesirli gecikmeli sistem, varlık teklik, Ulam-Hyers kararlılığı, göreceli kontrol edilebilirliği

INTRODUCTION

Fractional calculus is regarded as a generalization of integer calculus. Of course, this generalization contributes different positive capabilities which integer calculus does not have to fractional calculus. For example, according to researchers in this field, this enables fractional calculus to model almost all of scientific problem more suitable than integer order, numerical approaches to fractional calculus give better results compared to integer calculus, etc. Fractional calculus begins to be used in many areas such as mathematical physics, biophysics, engineering, signal processing, etc. For more details, all of reference section can be scanned.

A differential equation which consists of the present state and its rate of changes is said to be a delayed differential equation(Aydin et al., 2022; Aydin & Mahmudov, 2022; Mahmudov, 2022; Elshenhab & Wang, 2021b, 2021a; Mahmudov & Aydin, 2021; Liu et al., 2021; Mahmudov, 2019; Mahmudov, 2018; Li & Wang, 2018; Khusainov & Shuklin, 2003) if it also includes the past state. As stated and shown in (Mahmudov, 2019), a solution of a linear system $\rho'(\varsigma) = M\rho(\varsigma), \varsigma \geq 0$ has the form $\rho(\varsigma) = e^{M\varsigma}\rho(0)$, where the exponential matrix is also called fundamental matrix having a simple structure, but, it becomes more complex for seeking a fundamental matrix for a linear delayed system $\rho'(\varsigma) = M\rho(\varsigma) + A\rho(\varsigma - r), \varsigma \geq 0, r > 0$ with an initial condition $\rho(\varsigma) = \vartheta(\varsigma), -r \leq \varsigma \leq 0$, because of its fundamental matrix's complex structure caused by the delay parameter. Its solution, which is obtained by (Khusainov

ToCite: AYDIN, M., (2023). RELATIVE CONTROLLABILITY OF THE φ-CAPUTO FRACTIONAL DELAYED SYSTEM WITH IMPULSES. *Kahramanmaraş Sütçü İmam Üniversitesi Mühendislik Bilimleri Dergisi*, 26(Özel Sayı), 1121-1132.

& Shuklin, 2003) under the assumption of commutativity of the coefficient matrices M and A, naturally has a complex structure. So, it is difficult to work on such an equation according to equivalent studies. When we have look at the literature, these kinds of systems have been investigated in terms of controllability, stability, and existence and uniqueness of solutions (You et al., 2020; Liang et al., 2017; Wang et al., 2017; Khusainov & Shuklin, 2005) of the systems.

Generally, a differential equation is exploited to describe the dynamics of changing processes. The dynamics of many changing phenomena count on abrupt changes such as shocks, natural phenomena which is an observable event that is not non-made. These sorts of processes own short-dated perturbations (deviations) of continuous dynamics. When the duration of the entire advancement is considered, its lenght is negligible. While such deviations are modelled, these deviations can be described in the form of ‘‘impulses”. Consequently, modelling impulsive problems produce differential impulsive equations in optimal control, industrial robotics, ecology, population dynamics, physics (Bainov & Simeonov, 1993; Bainov & Simeonov, 1989; Lakshmikantham et al., 1989; Samoilenko & Perestyuk, 1989) and so on.

Mahmudov in (Mahmudov, 2019) consider a delayed system having noncommutative coefficients in the classical Caputo fractional sense with the same structure as (Khusainov & Shuklin, 2003) and offer an explicit solution by proposing the delay perturbation of the two-parameter Mittag-Leffler functions. The reseachers in (Aydin et al., 2022) examine the system obtained by using the Caputo fractional derivative with respect to another function instead of the classical Caputo fractional derivative in the system of (Mahmudov, 2019). In the sequel, Aydin and Mahmudov in (Aydin & Mahmudov, 2022) take the same system as (Mahmudov, 2019) by adding an impulsive initial condition into consideration and prove its controllability in the iterative learning control sense. This time, we combine the system of (Aydin et al., 2022) with an impulsive initial condition. This makes the system (1) different from the existing studies in the literature. To the best of our knowledge, this system is firstly introduced and its relative controllability is investigated.

Inspired by the above-cited studies, we investigate the below semilinear impulsesive fractional delayed differential equations consisting of the traditional Caputo fractional derivative with respect to another function

$$\begin{cases} {}_{-r^+}^{C}D_{\varphi}^{\beta}\,\rho(\varsigma) = M\rho(\varsigma) + A\rho(\varsigma - r) + g\big(\varsigma, \rho(\varsigma)\big), & 0 < \varsigma \le T, \quad r > 0, \\ \rho(\varsigma) = \vartheta(\varsigma), & -r \le \varsigma \le 0, \\ \rho(\varsigma_i^+) = \rho(\varsigma_i^-) + f\big(\rho(\varsigma_i)\big) & \varsigma_i \in J \end{cases} \tag{1}$$

where ${}_{-r^+}^{C}D_{\varphi}^{\beta}$ is φ-Caputo derivative of order $0 < \beta \le 1$. Here, φ is a real valued increasing function on $\mathbb{R}$ and $\varphi'(t) \neq 0$, $t \in [-r, T]$, $M, A \in \mathbb{R}^{n\times n}$ which do not have to be commutative. Also, $g \in C([0,T] \times \mathbb{R}^n, \mathbb{R}^n)$, $f \in C(\mathbb{R}^n, \mathbb{R}^n)$, and $\vartheta(\varsigma) \in C^1([-r, 0], \mathbb{R}^n)$, $J = \{\varsigma_1, \varsigma_2, \dots, \varsigma_m\}$ is the impulsive times with $0 < \varsigma_1 < \cdots < \varsigma_m < T$, $T = lr$ for a fixed $l \in \mathbb{N}$. The jumps

$$\rho(\varsigma_i^+) = \lim_{\varepsilon \to 0^+} \rho(\varsigma_i + \varepsilon), \qquad \rho(\varsigma_i^-) = \lim_{\varepsilon \to 0^-} \rho(\varsigma_i + \varepsilon)$$

express the right limit and the left limit of $\rho(\varsigma)$ at $\varsigma = \varsigma_i$, each to each.

PRELIMINARIES

In this section we will present most essential tools to be used in the following sections. $\mathbb{R}^n$ is the famous Euclidean space with dimension n ∈ {1,2,3, ... }. For a, b ∈ ℝ with a < b, let

$$C([a,b], \mathbb{R}^n) = \{f : [a,b] \to \mathbb{R}^n : f \text{ is continuous}\}$$

with the maximum norm $\|.\|_C$, which is

$$\|f\|_C = max\{\|f(\varsigma)\|, \varsigma \in [a,b]\}$$

for $\|.\|$ is a norm on $\mathbb{R}^n$. Let $AC[a,b]$ symbolise the absolutely continuous functions' space. For $n \in \{1,2,3,\dots\}$, $AC^n[a,b]$ the space of all complex-valued functions $f(\varsigma)$ such that $f^{(n-1)}(\varsigma) \in AC[a,b]$.

Lemma 1. (Lemma 3.4., Aydin et al., 2022) $\mathcal{X}^{M,A,\varphi}_{\beta,1,r}(\varsigma,t)$ is a solution of ${}_{-r^+}^{C}D^{\beta}_{\varphi}\,\rho(\varsigma) = M\rho(\varsigma) + A\rho(\varsigma - r)$, that is,

$$ {}_{-r^+}^{C}D^{\beta}_{\varphi}\mathcal{X}^{M,A,\varphi}_{\beta,1,r}(\varsigma,t) = M\mathcal{X}^{M,A,\varphi}_{\beta,1,r}(\varsigma,t) + A\mathcal{X}^{M,A,\varphi}_{\beta,1,r}(\varsigma,t+r). $$

Lemma 2. (Corollary 3.8., Aydin et al., 2022) A continuous solution w of the equation (1) without the impulsive initial condition is

$$ \rho(\varsigma) = \mathcal{X}^{M,A,\varphi}_{\beta,1,r}(\varsigma,-r)\vartheta(-r) + \int_{-r}^{0} \mathcal{X}^{M,A,\varphi}_{\beta,\beta,r}(\varsigma,t)\left[\left({}_{-r^+}^{C}D^{\beta}_{\varphi}\vartheta\right)(t) - A\vartheta(t)\right]d\varphi(t) + \int_{0}^{\varsigma} \mathcal{X}^{M,A,\varphi}_{\beta,\beta,r}(\varsigma,t)g\big(t,\rho(t)\big)d\varphi(t), $$

here, φ-delay perturbation of two-parameter Mittag-Leffler function $\mathcal{X}^{M,A,\varphi}_{\beta,\alpha,r}$ defined by

$$ \mathcal{X}^{M,A,\varphi}_{\beta,\alpha,r}(\varsigma,s) = \begin{cases} \Theta\,, & \varsigma - \mathrm{s} \in [-r,0), \\ I, & \varsigma = s\,, \\ \sum_{k=0}^{\infty}\sum_{j=0}^{l-1} Q_{k+1}(jr)\frac{[\varphi(\varsigma)-\varphi(s+jr)]^{k\beta+\alpha-1}}{\Gamma(k\beta+\alpha)}, & \varsigma - s \in ((l-1)r, lr], \end{cases} \tag{2} $$

where φ is an increasing real-valued function on $\mathbb{R}$ such that $\varphi'(\varsigma) \neq 0$, $t \in [-r,T]$, I and Θ are the representations of the identity and zero matrices each to each. In the light of (Mahmudov, 2019), the recursive matrices $Q_k(s)$ are defined for $s = kr$, $k = 0,1,2,\dots$, as

$$ Q_0(s) = \Theta, \quad Q_1(0) = \mathrm{I}, \quad Q_k(-r) = \Theta, \quad Q_{k+1}(s) = \mathrm{M}Q_k(s) + \mathrm{A}Q_k(s-r)\ . $$

Lemma 3. (Lemma 3.10., Aydin et al., 2022) If $t \in [0,T]$, $T = lr$ where $l \in \mathbb{N}$ and $r \in \mathbb{R}^+$, then the following inequality holds true:

$$ \int_0^{\varsigma} \left\| \mathcal{X}^{M,A,\varphi}_{\beta,\alpha,r}(\varsigma,s) \right\| d\varphi(s) \leq [\varphi(T) - \varphi(0)]\, \mathcal{X}^{\|M\|,\|A\|,\varphi}_{\beta,\alpha,r}(T,0)\ . $$

Lemma 4. (Lemma 3.3., Aydin et al., 2022) $\mathcal{X}^{M,A,\varphi}_{\beta,\alpha,r}(\varsigma,s)$ is a jointly continuous matrix operator in $0 < s < \varsigma < \infty$.

From here on, we will offer our fundamental contributions.

THE REPRESENTATION OF A SOLUTION

Theorem 5. A continuous solution ρ of the equation (1) is

$$ \rho(\varsigma) = \mathcal{X}^{M,A,\varphi}_{\beta,1,r}(\varsigma,-r)\vartheta(-r) + \int_{-r}^{0} \mathcal{X}^{M,A,\varphi}_{\beta,\beta,r}(\varsigma,t)\left[\left({}_{-r^+}^{C}D^{\beta}_{\varphi}\vartheta\right)(t) - A\vartheta(t)\right]d\varphi(t) + \int_{0}^{\varsigma} \mathcal{X}^{M,A,\varphi}_{\beta,\beta,r}(\varsigma,t)g(t,\rho(t))d\varphi(t) + \sum_{0<x_i<x} \mathcal{X}^{M,A,\varphi}_{\beta,1,r}(\varsigma,\varsigma_i)\, f\big(\rho(\varsigma_i)\big), \quad x > 0. $$

where $\mathcal{X}^{M,A,\varphi}_{\beta,\alpha,r}$ is φ-delay perturbation of two-parameter Mittag-Leffler function given above.

Proof. If one combines Lemma 1 with Lemma 2, the proof is completed out of the satisfaction of the impulsive initial condition. Now, we will show that the solution satisfies the impulsive initial condition. For each $\varsigma \in (\varsigma_{k-1}, \varsigma_k]$ the solution $\rho(\varsigma)$ is given by

$$\rho(\varsigma) = \mathcal{X}^{M,A,\varphi}_{\beta,1,r}(\varsigma,-r)\vartheta(-r) + \int_{-r}^{0} \mathcal{X}^{M,A,\varphi}_{\beta,\beta,r}(\varsigma,t)\left[\left({}_{-r^+}^{C}D^{\beta}_{\varphi}\vartheta\right)(t) - A\vartheta(t)\right]d\varphi(t)$$
$$+ \int_{0}^{\varsigma} \mathcal{X}^{M,A,\varphi}_{\beta,\beta,r}(\varsigma,t)g(t,\rho(t))d\varphi(t) + \sum_{i=0}^{k-1} \mathcal{X}^{M,A,\varphi}_{\beta,1,r}(\varsigma,\varsigma_i)\, f\big(\rho(\varsigma_i)\big),$$

and for each $\varsigma \in (\varsigma_k, \varsigma_{k+1}]$, we have

$$\rho(\varsigma) = \mathcal{X}^{M,A,\varphi}_{\beta,1,r}(\varsigma,-r)\vartheta(-r) + \int_{-r}^{0} \mathcal{X}^{M,A,\varphi}_{\beta,\beta,r}(\varsigma,t)\left[\left({}_{-r^+}^{C}D^{\beta}_{\varphi}\vartheta\right)(t) - A\vartheta(t)\right]d\varphi(t)$$
$$+ \int_{0}^{\varsigma} \mathcal{X}^{M,A,\varphi}_{\beta,\beta,r}(\varsigma,t)g(t,\rho(t))d\varphi(t) + \sum_{i=0}^{k} \mathcal{X}^{M,A,\varphi}_{\beta,1,r}(\varsigma,\varsigma_i)\, f\big(\rho(\varsigma_i)\big).$$

Since it is known that $\mathcal{X}^{M,A,\varphi}_{\beta,1,r}(\varsigma_k,\varsigma_k) = I$, we acquire

$$\rho(\varsigma_i^+) = \mathcal{X}^{M,A,\varphi}_{\beta,1,r}(\varsigma,-r)\vartheta(-r) + \int_{-r}^{0} \mathcal{X}^{M,A,\varphi}_{\beta,\beta,r}(\varsigma,t)\left[\left({}_{-r^+}^{C}D^{\beta}_{\varphi}\vartheta\right)(t) - A\vartheta(t)\right]d\varphi(t)$$
$$+ \int_{0}^{\varsigma} \mathcal{X}^{M,A,\varphi}_{\beta,\beta,r}(\varsigma,t)g(t,\rho(t))d\varphi(t) + \sum_{i=0}^{k} \mathcal{X}^{M,A,\varphi}_{\beta,1,r}(\varsigma,\varsigma_i)\, f\big(\rho(\varsigma_i)\big)$$
$$= \rho(\varsigma_i^-) + \mathcal{X}^{M,A,\varphi}_{\beta,1,r}(\varsigma_k,\varsigma_k)\, f\big(\rho(\varsigma_k)\big) = \rho(\varsigma_i^-) + f\big(\rho(\varsigma_k)\big)$$

which completes the proof.

EXISTENCE UNIQUENESS RESULTS

Unfortunately, the conditions given in the statements of the problem root is not enough to assure that the solution given in Theorem 5 is unique. So, we need to make a couple of extra assumptions as follows:

A_1 :: The function g satisfies the Lipschitz condition with $L_g > 0$,

$$\|g(\varsigma,\rho) - g(\varsigma,v)\| \le L_g\|\rho - v\|, \qquad \varsigma \in [0,T], \quad \rho, v \in \mathbb{R}^n.$$

A_2 :: The function f satisfies the Lipschitz condition with $L_f > 0$.

A_3 :: $\big([\varphi(T) - \varphi(0)]L_g + mL_f\big)max\left\{\mathcal{X}^{\|M\|,\|A\|,\varphi}_{\beta,1,r}(T,0), \mathcal{X}^{\|M\|,\|A\|,\varphi}_{\beta,\beta,r}(T,0)\right\} < 1.$

Theorem 6. Under all assumptions A_1, A_2, A_3, the integral equation given in Theorem 5 has a unique solution on $[-r,T]$.

Proof. Define $G\colon C([-r,T],\mathbb{R}^n) \to C([-r,T],\mathbb{R}^n)$ by

$$G\rho(\varsigma) = \mathcal{X}^{M,A,\varphi}_{\beta,1,r}(\varsigma,-r)\vartheta(-r) + \int_{-r}^{0} \mathcal{X}^{M,A,\varphi}_{\beta,\beta,r}(\varsigma,t)\left[\left({}_{-r^+}^{C}D^{\beta}_{\varphi}\vartheta\right)(t) - A\vartheta(t)\right]d\varphi(t)$$
$$+\int_{0}^{\varsigma} \mathcal{X}^{M,A,\varphi}_{\beta,\beta,r}(\varsigma,t)g(t,\rho(t))d\varphi(t) + \sum_{0<\varsigma_i<\varsigma} \mathcal{X}^{M,A,\varphi}_{\beta,1,r}(\varsigma,\varsigma_i)\, f\big(\rho(\varsigma_i)\big).$$

By taking arbitrary $\rho, v \in C\,([-r,T],\mathbb{R}^n)$, one can obtain the following estimation of $\|G\rho(\varsigma) - Gv(\varsigma)\|$:

$$\|G\rho(\varsigma) - Gv(\varsigma)\| \le L_g \int_0^{\varsigma} \left\|\mathcal{X}^{M,A,\varphi}_{\beta,\beta,r}(\varsigma,s)\right\| d\varphi(s)\ \|\rho - v\|_C + L_f \sum_{0<t_i<t} \left\|\mathcal{X}^{M,A,\varphi}_{\beta,1,r}(\varsigma,\varsigma_i)\right\|\ \|\rho - v\|_C$$
$$\le \big([\varphi(T) - \varphi(0)]L_g + mL_f\big) max\left\{\mathcal{X}^{\|M\|,\|A\|,\varphi}_{\beta,1,r}(T,0), \mathcal{X}^{\|M\|,\|A\|,\varphi}_{\beta,\beta,r}(T,0)\right\}\ \|\rho - v\|_C$$

In the light of A_3, G is a contraction. Consequently, G owns a unique fixed point due to Banach fixed point theorem.

STABILITY RESULTS

In this section, we firstly share fundamental definition and remark to demonstrate that the equation (1) is Ulam-Hyers (UH) stable.

Definition 7. If $\forall \epsilon > 0$ and for any solution $\rho \in C\,([0,T],\mathbb{R}^n)$ of inequality

$$\left\|{}_{-r^+}^{C}D^{\beta}_{\varphi}\,\rho(\varsigma) - M\rho(\varsigma) - A\rho(\varsigma - r) - g\big(\varsigma,\rho(\varsigma)\big)\right\| < \epsilon \tag{3}$$

then there is a solution $v \in C\,([0,T],\mathbb{R}^n)$ of (1), and a $\sigma > 0$ such that

$$\|\rho(\varsigma) - v(\varsigma)\| < \sigma\epsilon, \quad \varsigma \in [0,T]. \tag{4}$$

Then, equation (1) is UH-stable.

Remark 8. A function $\rho \in C'\,([0,T],\mathbb{R}^n)$ is a solution of (3) iff there is at least one element $h \in C\,([0,T],\mathbb{R}^n)$ fulfilling

- $\|h(\varsigma)\| \le \epsilon$
- ${}_{-r^+}^{C}D^{\beta}_{\varphi}\rho(\varsigma) = M\rho(\varsigma) + A\rho(\varsigma - r) + g\big(\varsigma,\rho(\varsigma)\big) + h(\varsigma)$.

Theorem 9. Under all of circumstances in Theorem 6, the system (1) is stable in the sense of Ulam-Hyers.

Proof. Suppose $\rho \in C\,([0,T],\mathbb{R}^n)$ that fulfils (3), and let $v \in C\,([0,T],\mathbb{R}^n)$ which is the unique solution of system (1) with the initial condition $v(\varsigma) = \rho(\varsigma)$ for all $\varsigma \in [-r,0]$, $\rho(\varsigma_i^+) - \rho(\varsigma_i^-) = v(\varsigma_i^+) - v(\varsigma_i^-) = f\big(\rho(\varsigma_i)\big)$. Based on Remark 8 and the rule of G, one acquires

$$\|h(\varsigma)\| \le \epsilon, \quad \rho(\varsigma) = G\rho(\varsigma) + \int_0^{\varsigma} \mathcal{X}^{M,A,\varphi}_{\beta,\beta,r}(\varsigma,t)h(t)d\varphi(t),$$

and also $v(\varsigma) = Gv(\varsigma)$ for each $\varsigma \in [0,T]$. One gets

$$\|G\rho(\varsigma) - \rho(\varsigma)\| \le \int_0^{\varsigma} \left\|\mathcal{X}^{M,A,\varphi}_{\beta,\beta,r}(\varsigma,s)\right\| \|h(s)\| d\varphi(s) \le [\varphi(T) - \varphi(0)]\mathcal{X}^{\|M\|,\|A\|,\varphi}_{\beta,\beta,r}(T,0)\epsilon.$$

We are set to make an estimation $\|v(\varsigma) - \rho(\varsigma)\|$:

$$\|v(\varsigma) - \rho(\varsigma)\| \le \|v(\varsigma) - G\rho(\varsigma)\| + \|G\rho(\varsigma) - \rho(\varsigma)\|$$

$$\leq \left([\varphi(T)-\varphi(0)]L_g + mL_f\right) max\left\{\mathcal{X}_{\beta,1,r}^{\|M\|,\|A\|,\varphi}(T,0), \mathcal{X}_{\beta,\beta,r}^{\|M\|,\|A\|,\varphi}(T,0)\right\} \|\rho - v\|_C$$
$$+[\varphi(T)-\varphi(0)]\mathcal{X}_{\beta,\beta,r}^{\|M\|,\|A\|,\varphi}(T,0)\epsilon$$

which provides

$$\|v-\rho\|_C \leq \sigma\epsilon,$$

where

$$\sigma = \frac{[\varphi(T)-\varphi(0)]\mathcal{X}_{\beta,\beta,r}^{\|M\|,\|A\|,\varphi}(T,0)}{1-\left([\varphi(T)-\varphi(0)]L_g + mL_f\right) max\left\{\mathcal{X}_{\beta,1,r}^{\|M\|,\|A\|,\varphi}(T,0), \mathcal{X}_{\beta,\beta,r}^{\|M\|,\|A\|,\varphi}(T,0)\right\}} > 0.$$

This last point completes the proof.

RELATIVE CONTROLLABILITY RESULTS

In current section we relatively investigate the controllability of the impulsive fractional delayed differential systems having Caputo fractional derivatives w.r.t. another function while it is not only linear but also semilinear.

Definition 10. System (1) is called relatively controllable, if there is a control $u \in L^2(I=[0,T],\mathbb{R}^n)$ so that equation (1) owns a solution $\rho \in C([-r,\tau],\mathbb{R}^n)$ that holds the initial delayed condition, the initial impulsive condition, and $\rho(\tau) = \rho_\tau$ for the arbitrary final value $\rho_\tau \in \mathbb{R}^n$ with the arbitrary time τ, any initial continuously differentiable $\mathbb{R}^n$-valued function φ on $[-\mathrm{r},0]$.

There are two cases for the system (1) to investigate its relative controllability. If the system (1) is without the semilinear term $g(\varsigma,\rho(\varsigma))$, $0<\varsigma\leq T$, it is called the linear case of the system (1). Otherwise, it is called the semilinear case of the system (1). We will consider these two cases individually as follows.

The Relative Controllability of the Linear Case of the System (1).

We will consider the following control system

$$\begin{cases} {}_{-r^+}^{C}D_{\varphi}^{\beta}\,\rho(\varsigma) = M\rho(\varsigma) + A\rho(\varsigma-r) + Su(\varsigma), & 0<\varsigma\leq T,\quad r>0,\\ \rho(\varsigma) = \vartheta(\varsigma), & -r\leq\varsigma\leq 0,\\ \rho(\varsigma_i^+) = \rho(\varsigma_i^-) + f\big(\rho(\varsigma_i)\big) & \varsigma_i\in J \end{cases} \tag{5}$$

whose solution is given by

$$\rho(\varsigma) = \mathcal{X}_{\beta,1,r}^{M,A,\varphi}(\varsigma,-r)\vartheta(-r) + \int_{-r}^{0}\mathcal{X}_{\beta,\beta,r}^{M,A,\varphi}(\varsigma,s)\left[\left({}_{-r^+}^{C}D_{\varphi}^{\beta}\vartheta\right)(s) - A\vartheta(s)\right]d\varphi(s)$$
$$+\int_{0}^{\varsigma}\mathcal{X}_{\beta,\beta,r}^{M,A,\varphi}(\varsigma,s)Su(s)d\varphi(s) + \sum_{0<\varsigma_i<\varsigma}\mathcal{X}_{\beta,1,r}^{M,A,\varphi}(\varsigma,\varsigma_i)\,f\big(\rho(\varsigma_i)\big),$$

here $u\in\mathbb{R}^n$ is a control function and $S\in\mathbb{R}^{n\times n}$.

Theorem 11. The system (5) is relatively controllable if and only if the following Gramian matrix

$$W[0,\tau] = \int_{0}^{\tau}\mathcal{X}_{\beta,\beta,r}^{M,A,\varphi}(\tau,s)SS^*\,\mathcal{X}_{\beta,\beta,r}^{M^*,A^*,\varphi}(\tau,s)d\varphi(s)$$

is nonsingular, where $.^*$ stands for the transpose of a matrix.

Proof. ⇒: Let $W[0,\tau]$ be singular while the system (5) is relatively controllable. There is **a** nonzero $\pi \in \mathbb{R}^n$,

$$W[0,\tau]\,\pi = 0.$$

One gets

$$\int_0^\tau \pi^* \mathcal{X}^{M,A,\varphi}_{\beta,\beta,r}(\tau,s) S S^* \mathcal{X}^{M^*,A^*,\varphi}_{\beta,\beta,r}(\tau,s)\pi d\varphi(s) = 0,$$

which provides

$$\pi^* \mathcal{X}^{M,A,\varphi}_{\beta,\beta,r}(\tau,s) S = 0, \quad 0 \le s \le \tau.$$

Based on the relative controllability of the system, we can find u_1 and u_2 for the different final $0, \pi \in \mathbb{R}^n$,respectively so that

$$\pi^*\pi = \int_0^\tau \pi^* \mathcal{X}^{M,A,\varphi}_{\beta,\beta,r}(\tau,s) S\left(u_2(s) - u_1(s)\right) d\varphi(s) = 0$$

from which $\pi = 0$ is obtained. This is a contradiction.

⇐: By means of the invertibility of the Gramian matrix, it is known that its inverse $W^{-1}[0,\tau]$ exists. If one regards the following continuous function

$$u(\varsigma) = S^* \mathcal{X}^{M^*,A^*,\varphi}_{\beta,\beta,r}(\tau,\varsigma)\, W^{-1}[0,\tau]\ \vartheta$$

where

$$\vartheta(\varsigma) = \rho_\tau - \mathcal{X}^{M,A,\varphi}_{\beta,1,r}(\varsigma,-r)\vartheta(-r) - \int_{-r}^{0} \mathcal{X}^{M,A,\varphi}_{\beta,\beta,r}(\varsigma,t)\left[\left({}_{-r}^{C}D^{\beta}_{\varphi}\vartheta\right)(t) - A\vartheta(t)\right] d\varphi(t) - \sum_{0<\varsigma_i<\varsigma} \mathcal{X}^{M,A,\varphi}_{\beta,1,r}(\varsigma,\varsigma_i)\, f\left(\rho(\varsigma_i)\right).$$

as a control, one can easily observe $\rho(\tau) = \rho_\tau$, and w fulfills all of the initial conditions

The Relative Controllability of the Semilinear Case of the System (1).

We will consider the following control system

$$\begin{cases} {}_{-r}^{C}D^{\beta}_{\varphi}\,\rho(\varsigma) = M\rho(\varsigma) + A\rho(\varsigma - r) + g\left(\varsigma,\rho(\varsigma)\right) + Su(\varsigma), & 0 < \varsigma \le T,\ \ r > 0, \\ \rho(\varsigma) = \vartheta(\varsigma), & -r \le \varsigma \le 0, \\ \rho(\varsigma_i^+) = \rho(\varsigma_i^-) + f\left(\rho(\varsigma_i)\right) & \varsigma_i \in J \end{cases} \tag{6}$$

whose solution is given by

$$\rho(\varsigma) = \mathcal{X}^{M,A,\varphi}_{\beta,1,r}(\varsigma,-r)\vartheta(-r) + \int_{-r}^{0} \mathcal{X}^{M,A,\varphi}_{\beta,\beta,r}(\varsigma,t)\left[\left({}_{-r}^{C}D^{\beta}_{\varphi}\vartheta\right)(t) - A\vartheta(t)\right] d\varphi(t)$$

$$+\int_0^{x} \mathcal{X}_{\beta,\beta,r}^{M,A,\varphi}(\varsigma,t)g\big(t,\rho(t)\big)d\varphi(t)+\sum_{0<\varsigma_i<\varsigma}\mathcal{X}_{\beta,1,r}^{M,A,\varphi}(\varsigma,\varsigma_i)\,f\big(\rho(\varsigma_i)\big).$$
$$+\int_0^{\varsigma} \mathcal{X}_{\beta,\beta,r}^{M,A,\varphi}(\varsigma,t)Su(t)d\varphi(t),\quad \varsigma>0.$$

Unfortunately, we can not control this system without putting extra conditions on the nonlinear function and impulsive function, an extra operator. Now, let us make some assumptions as follows:

A_4 :: The operator $M: L^2(I,\mathbb{R}^n)\longrightarrow \mathbb{R}^n$

$$Mu=\int_0^{\tau} \mathcal{X}_{\beta,\beta,r}^{M,A,\varphi}(\tau,s)Su(s)d\varphi(s),$$

owns an inverse M^{-1} which taking values in $L^2(I,\mathbb{R}^n)/kerM$. Let X_i, $i=1,2$, be Banach spaces. $B(X_1,X_2)$ consisting of all both bounded and linear is endowed with the norm $\|.\|_B$. For simplicity, we will set

$$R:=\|M^{-1}\|_{B\left(\mathbb{R}^n,L^2(I,\mathbb{R}^n)/kerM\right)},$$
$$R_1:=\left\|\mathcal{X}_{\beta,1,r}^{M,A,\varphi}(\varsigma,-r)\vartheta(-r)\right\|+\left\|\int_{-r}^{0}\mathcal{X}_{\beta,\beta,r}^{M,A,\varphi}(\varsigma,s)\left[\left({}_{-r^+}^{C}D_{\varphi}^{\beta}\vartheta\right)(s)-A\vartheta(s)\right]d\varphi(s)\right\|,$$
$$R_2:=\sum_{0<\varsigma_i<\varsigma}\left\|\mathcal{X}_{\beta,1,r}^{M,A,\varphi}(\varsigma,\varsigma_i)\right\|\,|f(0)|+[\varphi(T)-\varphi(0)]\mathcal{X}_{\beta,\beta,r}^{\|M\|,\|A\|,\varphi}(T,0)\max_{[0,T]}|g(\varsigma,0)|,$$
$$R_3:=\left(L_f\sum_{0<\varsigma_i<\varsigma}\left\|\mathcal{X}_{\beta,1,r}^{M,A,\varphi}(\varsigma,\varsigma_i)\right\|\,|f(0)|+L_g[\varphi(T)-\varphi(0)]\mathcal{X}_{\beta,\beta,r}^{\|M\|,\|A\|,\varphi}(T,0)\right)\|\rho\|_{C}.$$

From Remark 3.3. of (Wang et al., 2017),

$$R=\sqrt{\|W^{-1}[0,\tau]\|}.$$

Theorem 12. Suppose that $1\geq\beta>0.5$. Under the assumptions A_1, A_2, and A_4 are fulfilled. Then the system (6) is relatively controllable if

$$(1+R\|S\|max\{1,R_3\})R_3<1.$$

Proof. Based on the assumption A_4, one can define the following control function

$$u_{\rho}=M^{-1}\left[\rho_{\tau}-\mathcal{X}_{\beta,1,r}^{M,A,\varphi}(\varsigma,-r)\vartheta(-r)-\int_{-r}^{0}\mathcal{X}_{\beta,\beta,r}^{M,A,\varphi}(\varsigma,s)\left[\left({}_{-r^+}^{C}D_{\varphi}^{\beta}\vartheta\right)(s)-A\vartheta(s)\right]d\varphi(s)\right]$$
$$+M^{-1}\left[-\sum_{0<\varsigma_i<\varsigma}\mathcal{X}_{\beta,1,r}^{M,A,\varphi}(\varsigma,\varsigma_i)\,f\big(\rho(\varsigma_i)\big)-\int_0^{\varsigma}\mathcal{X}_{\beta,\beta,r}^{M,A,\varphi}(\varsigma,s)g\big(s,\rho(s)\big)d\varphi(s)\right].$$

By executing this control function, one can also define $K:C\,(I,\mathbb{R}^n)\rightarrow C\,(I,\mathbb{R}^n)$ by

$$K\rho(\varsigma) = \mathcal{X}^{M,A,\varphi}_{\beta,1,r}(\varsigma,-r)\vartheta(-r) + \int_{-r}^{0} \mathcal{X}^{M,A,\varphi}_{\beta,\beta,r}(\varsigma,t)\left[\left({}_{-r}^{C}D^{\beta}_{\varphi}\vartheta\right)(t) - A\vartheta(t)\right]d\varphi(t)$$
$$+\int_{0}^{\varsigma} \mathcal{X}^{M,A,\varphi}_{\beta,\beta,r}(\varsigma,t)g\big(t,\rho(t)\big)d\varphi(t) + \sum_{0<\varsigma_i<\varsigma} \mathcal{X}^{M,A,\varphi}_{\beta,1,r}(\varsigma,\varsigma_i)\,f\big(\rho(\varsigma_i)\big).$$
$$+\int_{0}^{\varsigma} \mathcal{X}^{M,A,\varphi}_{\beta,\beta,r}(\varsigma,t)Su_{\rho}(t)d\varphi(t),\ \ \varsigma > 0.$$

Now, we need to determine such a radius r for $D_r \coloneqq \{\rho \in C\ (I,\mathbb{R}^n) :\ \|\rho\|_C \le r\}$ which is a convex, closed and bounded subset that $K(D_r)\ \subseteq\ D_r$. To do this, start with the norm of the control function:

$$\|u_{\rho}\| \le R(R_1 + R_2 + R_3\|\rho\|_C).$$

The norm of the operator $K\rho(\varsigma)$ for $\rho \in D_r$ is

$$\|K\rho(\varsigma)\ \| \le R_1 + R_2 + R_3\|\rho\|_C + R\|S\|(R_1 + R_2 + R_3\|\rho\|_C).$$

If we take

$$r = \frac{(1+R\|S\|)(R_1+R_2) + R\|S\|\|w_{\tau}\|}{1-(1+R\|S\|max\{1,R_3\})R_3} > 0,$$

the desired thing is demonstrated. Now we will separate K in two different operators as follows:

$$K_1\rho(\varsigma) = \mathcal{X}^{M,A,\varphi}_{\beta,1,r}(\varsigma,-r)\vartheta(-r) + \int_{-r}^{0} \mathcal{X}^{M,A,\varphi}_{\beta,\beta,r}(\varsigma,s)\left[\left({}_{-r}^{C}D^{\beta}_{\varphi}\vartheta\right)(s) - A\vartheta(s)\right]d\varphi(s)$$
$$+\int_{0}^{\varsigma} \mathcal{X}^{M,A,\varphi}_{\beta,\beta,r}(\varsigma,s)Su_{\rho}(s)d\varphi(s) + \sum_{0<\varsigma_i<\varsigma} \mathcal{X}^{M,A,\varphi}_{\beta,1,r}(\varsigma,\varsigma_i)\,f\big(\rho(\varsigma_i)\big), \qquad \varsigma \in I,$$

and

$$K_2w(\varsigma) = \int_{0}^{\varsigma} \mathcal{X}^{M,A,\varphi}_{\beta,\beta,r}(\varsigma,s)g\big(s,\rho(s)\big)d\varphi(s),\ \ \varsigma \in I.$$

For $\rho, v \in D_r$, one gets

$$\|u_{\rho}(\varsigma) - u_{v}(\varsigma)\| \le RR_3\|\rho(\varsigma) - v(\varsigma)\|$$

and

$$\begin{aligned}\|K_1\rho(\varsigma) - K_1v(\varsigma)\| &\le [\varphi(T)-\varphi(0)]\mathcal{X}^{\|M\|,\|A\|,\varphi}_{\beta,\beta,r}(T,0)\|S\|\ \|u_{\rho}(\varsigma) - u_{v}(\varsigma)\| \\ &\quad + L_f \sum_{0<\varsigma_i<\varsigma} \left\|\mathcal{X}^{M,A,\varphi}_{\beta,1,r}(\varsigma,\varsigma_i)\right\|\ \|\rho - v\|_C \\ &\le [\varphi(T)-\varphi(0)]\mathcal{X}^{\|M\|,\|A\|,\varphi}_{\beta,\beta,r}(T,0)\|S\|RR_3\|\rho - v\|_C \\ &\quad + L_f \sum_{0<\varsigma_i<\varsigma} \left\|\mathcal{X}^{M,A,\varphi}_{\beta,1,r}(\varsigma,\varsigma_i)\right\|\ \|\rho - v\|_C \\ &\le (1 + R\|S\|max\{1,R_3\})R_3\|\rho - v\|_C,\end{aligned}$$

which gives that K_1 is a contraction. Assume that $\rho_n \in D_r$ with $\rho_n \longrightarrow \rho$ in D_r . Since g is continuous, $g(\varsigma, \rho_n(\varsigma)) \rightarrow g(\varsigma, \rho(\varsigma))$. By using dominated convergence theorem

$$\|K_2\rho_n(\varsigma) - K_2\rho(\varsigma)\| \leq \int_0^{\varsigma} \left\|\mathcal{X}_{\beta,\beta,r}^{M,A,\varphi}(\varsigma, s)\right\| \left\|g\big(s, \rho_n(s)\big) - g\big(s, \rho(s)\big)\right\| d\varphi(s),$$

goes to zero as n tends to ∞. Thus, K_2 is continuous on D_r. The last task is to show that K_2 is compact. For $\rho \in D_r$, $0 < \varsigma < \varsigma + h < \tau$

$$K_2\rho(\varsigma + h) - K_2\rho(\varsigma) = \int_t^{\varsigma+h} \mathcal{X}_{\beta,\beta,r}^{M,A,\varphi}(\varsigma + h, s) g\big(s, \rho(s)\big) d\varphi(s)$$
$$+ \int_0^{\varsigma} \left(\mathcal{X}_{\beta,\beta,r}^{M,A,\varphi}(\varsigma + h, s) - \mathcal{X}_{\beta,\beta,r}^{M,A,\varphi}(\varsigma, s)\right) g\big(s, \rho(s)\big) d\varphi(s).$$

Introduce the below notations:

$$\lambda_1 := \int_{\varsigma}^{\varsigma+h} \mathcal{X}_{\beta,\beta,r}^{M,A,\varphi}(\varsigma + h, s) g\big(s, \rho(s)\big) d\varphi(s),$$
$$\lambda_2 := \int_0^{\varsigma} \left(\mathcal{X}_{\beta,\beta,r}^{M,A,\varphi}(\varsigma + h, s) - \mathcal{X}_{\beta,\beta,r}^{M,A,\varphi}(\varsigma, s)\right) g\big(s, \rho(s)\big) d\varphi(s) .$$

With an easy calculation, one can acquire

$$\|\lambda_1\| \leq \left(L_g\|\rho\|_C + \max_{[0,T]}|g(\varsigma, 0)|\right) \int_{\varsigma}^{\varsigma+h} \left\|\mathcal{X}_{\beta,\beta,r}^{M,A,\varphi}(\varsigma + h, s)\right\| d\varphi(s) \longrightarrow 0,$$
$$\|\lambda_2\| \leq \left(L_g\|\rho\|_C + \max_{[0,T]}|g(\varsigma, 0)|\right) \int_0^{\varsigma} \left\|\mathcal{X}_{\beta,\beta,r}^{M,A,\varphi}(\varsigma + h, s) - \mathcal{X}_{\beta,\beta,r}^{M,A,\varphi}(\varsigma, s)\right\| d\varphi(s) \longrightarrow 0,$$

as $h \longrightarrow 0$. As a result, one acquires

$$\|K_2\rho(\varsigma + h) - K_2\rho(\varsigma)\| \leq \|\lambda_1\| + \|\lambda_2\| \longrightarrow 0 \ \ as \ \ h \longrightarrow 0.$$

$K_2(D_r)$ is uniformly bounded because one easily reach to the following upper bound for all members of $K_2(D_r)$ with the familiar computations,

$$\|K_2\rho\| \leq \left(L_g r + \max_{[0,T]}|g(\varsigma, 0)|\right) \tau\, \mathcal{X}_{\beta,\beta,r}^{\|M\|,\|A\|,\varphi}(\tau, 0).$$

Because of the equicontinuity and uniform boundedness of K_2, Arzela-Ascoli theorem provides K_2 is compact. Due to the fixed-point theorem of Krasnoselskii, K owns a fixed point $\rho \in D_r$.

CONCLUSION

The current paper is, in brief, devoted to investigating the both uniqueness and existence of the solution and examining stability and controllability of the discussed equations. The obtained results are quite comprehensive and cover many studies which are not available in the literature because the Caputo fractional derivative with respect to

another function reduces to the classical Caputo fractional derivative in the case of $\varphi(\varsigma) = \varsigma$ and Hadamard fractional derivate when $\varphi(\varsigma) = \ln \varsigma$. For a next problem, the following neutral fractional system:

$$\begin{cases} {}_{-r^+}^{C}D_{\varphi}^{\beta}\,\rho(\varsigma) - N\,{}_{-r^+}^{C}D_{\varphi}^{\beta}\rho(\varsigma - r) = M\rho(\varsigma) + A\rho(\varsigma - r) + g\big(\varsigma, \rho(\varsigma)\big), & 0 < \varsigma \le T, \quad r > 0, \\ \rho(\varsigma) = \vartheta(\varsigma), & -r \le \varsigma \le 0, \\ \rho(\varsigma_i^+) = \rho(\varsigma_i^-) + f\big(\rho(\varsigma_i)\big) & \varsigma_i \in J \end{cases}$$

where $N \in \mathbb{R}^n$ and the remaining information is given in (1), can be taken into consideration and the stability and controllability of this neutral fractional system can be investigated in addition to the fact that both the uniqueness and existence of its solution are examined.

REFERENCES

Aydin, M., Mahmudov, N. I., Aktuğlu, H., Baytunç, E., & Atamert, M. S. (2022). On a study of the representation of solutions of a Ψ-Caputo fractional differential equations with a single delay. Electronic Research Archive, 30, 1016–1034.

Aydin, M., & Mahmudov, N. I. (2022). Iterative learning control for impulsive fractional order time-delay systems with nonpermutable constant coefficient matrices. International Journal of Adaptive Control and Signal Processing, 36(1), 1419–1438.

Bainov, D. D., & Simeonov, P. S. (1989). Systems with Impulse Effect. Ellis Horwood Series:Mathematics and Its Applications, Ellis Horwood, Chichester.

Bainov, D. D., & Simeonov, P. S. (1993). Impulsive Differential Equations: Periodic Solutions and Applications, Pitman Monographs and Surveys in Pure and Applied Mathematics. (66 vol.). Longman Scientific & Technical, Harlow; JohnWiley & Sons, New York.

Elshenhab, A. M., & Wang, X. T. (2021a). Representation of solutions for linear fractional systems with pure delay and multiple delays. Mathematical Methods in the Applied Sciences, 44, 12835–12850.

Elshenhab, A. M., & Wang, X. T. (2021b). Representation of solutions of linear differential systems with pure delay and multiple delays with linear parts given by non-permutable matrices. *Applied Mathematics and Computation*, 410, 126443. https://doi.org/10.1016/j.amc.2021.126443

Khusainov, D. Y., & Shuklin, G. V. (2005). Relative controllability in systems with pure delay. *International Journal of Applied Mathematics*, 2, 210–221. https://doi.org/10.1007/s10778-005-0079-3

Khusainov, D. Y., & Shuklin, G. V. (2003). Linear autonomous time-delay system with permutation matrices solving. *Stud. Univ. Zilina*, 17, 101–108.

Lakshmikantham, V., Bainov, D. D., & Simeonov, P. S. (1989). Theory of Impulsive Differential Equations, Series in Modern Applied Mathematics. (6 vol.). World Scientific, New Jersy. https://doi.org/10.1142/0906

Liang, C., Wang, J., & O'Regan, D. (2017). Controllability of nonlinear delay oscillating systems. *Electronic Journal of Qualitative Theory of Differential Equations*, 2017, 1–18. https://doi.org/10.14232/ejqtde.2017.1.47

Li, M., & Wang, J. R. (2018). Exploring delayed Mittag-Leffler type matrix functions to study finite time stability of fractional delay differential equations. *Applied Mathematics and Computation*, 324, 254–265. https://doi.org/10.1016/j.amc.2017.11.063

Liu, L., Dong, Q., & Li, G. (2021). Exact solutions and Hyers–Ulam stability for fractional oscillation equations with pure delay. *Applied Mathematics Letters*, 112, 106666. https://doi.org/10.1016/j.aml.2020.106666

Mahmudov, N. I., & Aydın, M. (2021). Representation of solutions of nonhomogeneous conformable fractional delay differential equations. *Chaos Solitons Fractals*, 150, 111190. https://doi.org/10.1016/j.chaos.2021.111190

Mahmudov, N. I. (2022). Multi-delayed perturbation of Mittag-Leffler type matrix functions. *Journal of Mathematical Analysis and Applications*, 505, 125589. https://doi.org/10.1016/j.jmaa.2021.125589

Mahmudov, N. I. (2019). Delayed perturbation of Mittag-Leffler functions and their applications to fractional linear delay differential equations. *Mathematical Methods in the Applied Sciences*, 42, 5489–5497. https://doi.org/10.1002/mma.5446

Mahmudov, N. I. (2018). Representation of solutions of discrete linear delay systems with non permutable matrices. *Applied Mathematics Letters*, 85, 8–14. https://doi.org/10.1016/j.aml.2018.05.015

Samoilenko, A. M., & Perestyuk, N. A. (1995). Impulsive Differential Equations, World Scientific Serieson Nonlinear Science. Series A:Monographs and Treatises, vol. 14, World Scientific, New Jersey, ISBN: 978-981-02-2416-5. https://doi.org/10.1142/2892

Wang, J., Luo, Z., & Feckan, M. (2017). Relative controllability of semilinear delay differential systems with linear parts defined by permutable matrices. *European Journal of Control*, 38, 39–46. https://doi.org/10.1016/j.ejcon.2017.08.002

You, Z., Feckan, M., & Wang, J. (2020). Relative Controllability of Fractional Delay Differential Equations via Delayed Perturbation of Mittag-Leffler Functions. *Journal of Computational and Applied Mathematics*, 378, 112939. https://doi.org/10.1016/j.cam.2020.112939.

KSÜ Mühendislik Bilimleri Dergisi, 26(Özel Sayı), 2023 KSU J Eng Sci, 26(Special Issue), 2023
9th Uluslararası IFS Çağdaş Matematik ve Mühendislik Konferansı Özel Sayısı
9th International IFS Contemporary Mathematics and Engineering Conference Special Issue
Araştırma Makalesi Research Article

Kahramanmaras Sutcu Imam University Journal of Engineering Sciences

Geliş Tarihi : 09.08.2023 Received Date : 09.08.2023
Kabul Tarihi : 25.09.2023 Accepted Date : 25.09.2023

MASKED AND UNMASKED FACE RECOGNITION ON UNCONSTRAINED FACIAL IMAGES USING HAND-CRAFTED METHODS

KISITLANMAMIŞ YÜZ GÖRÜNTÜLERİNDE EL YAPIMI YÖNTEMLERLE MASKELİ VE MASKESİZ YÜZ TANIMA

Ali TORBATİ[1] (ORCID: 0009-0005-5908-5840)
Önsen TOYGAR[1*] (ORCID: 0000-0001-7402-9058)

[1] Eastern Mediterranean University, Computer Engineering Department, Famagusta, North Cyprus, via Mersin 10, Türkiye

*Sorumlu Yazar / Corresponding Author: Önsen Toygar, onsen.toygar@emu.edu.tr

ABSTRACT

In this study, the face recognition task is applied on masked and unmasked faces using hand-crafted methods. Due to COVID-19 and masks, facial identification from unconstrained images became a hot topic. To avoid COVID-19, most people use masks outside. In many cases, typical facial recognition technology is useless. The majority of contemporary advanced face recognition methods are based on deep learning, which primarily relies on a huge number of training examples, however, masked face recognition may be investigated using hand-crafted approaches at a lower computing cost than using deep learning systems. A low-cost system is intended to be constructed for recognizing masked faces and compares its performance to that of face recognition systems that do not use masks. The proposed method fuses hand-crafted methods using feature-level fusion strategy. This study compares the performance of masked and unmasked face recognition systems. The experiments are undertaken on two publicly accessible datasets for masked face recognition: Masked Labeled Faces in the Wild (MLFW) and Cross-Age Labeled Faces in the Wild (CALFW). The best accuracy is achieved as 94.8% on MLFW dataset. The rest of the results on different train and test sets from CALFW and MLFW datasets are encouraging compared to the state-of-the-art models.

Keywords: Masked face recognition, unmasked face recognition, hand-crafted methods.

ÖZET

Bu çalışmada, maskeli ve maskesiz yüzlerde el yapımı yöntemler kullanılarak yüz tanıma görevi uygulanmıştır. COVID-19 ve maskeler nedeniyle, kısıtlanmamış görüntülerden yüz tanıma önemli bir konu haline gelmiştir. COVID-19'dan kaçınmak için çoğu insan dışarıda maske kullanmaktadır. Birçok durumda, tipik yüz tanıma teknolojisi işe yaramaz. Çoğu çağdaş ileri yüz tanıma yöntemi derin öğrenmeye dayanır ve büyük ölçüde birçok eğitim örneğine dayanır, ancak maske takılmış yüz tanıma, derin öğrenme sistemlerini kullanmaktan daha düşük bir hesaplama maliyeti ile el yapımı yaklaşımlar kullanılarak araştırılabilir. Maske takılmış yüzleri tanımak için düşük maliyetli bir sistem oluşturmak ve maske kullanmayan yüz tanıma sistemlerinin performansını karşılaştırma amaçlanmıştır. Önerilen yöntem, öznitelik düzeyi kaynaşım stratejisi kullanarak el yapımı yöntemleri birleştirir. Bu çalışma, maske takılmış ve takılmamış yüz tanıma sistemlerinin performansını karşılaştırmaktadır. Deneyler, maskeli yüz tanıma için erişime açık iki veri kümesi Masked Labeled Faces in the Wild (MLFW) ve Cross-Age Labeled Faces in the Wild (CALFW) üzerinde gerçekleştirilmiştir. En iyi doğruluk oranı, MLFW veri kümesinde %94,8 olarak elde edilmiştir. CALFW ve MLFW veri kümelerinden farklı eğitim ve test kümeleri kullanılarak elde edilen diğer sonuçlar, mevcut en iyi modellere göre cesaret vericidir.

Anahtar Kelimeler: Maskeli yüz tanıma, maskesiz yüz tanıma, el yapımı yöntemler.

ToCite: TORBATİ, A., & TOYGAR, Ö., (2023). MASKED AND UNMASKED FACE RECOGNITION ON UNCONSTRAINED FACIAL IMAGES USING HAND-CRAFTED METHODS. *Kahramanmaraş Sütçü İmam University, Journal of Engineering Sciences*, 26(Özel Sayı), 1133-1139.

INTRODUCTION

The study of computer vision involves developing algorithms and models that can allow computers to interpret, analyze, and understand visual data from the world around them. It involves techniques for analyzing, processing, and understanding images and video data, as well as techniques for recognizing patterns, objects, and features in this data. There are some key differences in the way that computers and humans process images. One major difference is that computers can process images much more quickly and accurately than humans, making them well-suited for tasks such as analyzing large datasets of images or detecting patterns and features in images.

Computers may use a technique called face recognition to identify and authenticate people in images or streaming videos. The ability of computers is what makes it possible to analyze and understand visual data, and it involves developing algorithms and models that can extract and analyze features from images of faces. When it comes to recognizing faces, one of the major obstacles is being able to accurately identify and distinguish one face from another, even when there are variations in lighting, pose, expression, and other factors. To achieve this, face recognition systems typically use a combination of machine learning algorithms and image processing techniques to analyze and compare the unique features of different faces.

Machine learning's ultimate aim is to make it so computers can teach themselves new skills by analyzing existing data and make inferences or choices without being explicitly programmed. It's predicated on the premise that computers can analyze data, spot trends, and decide what to do next.

In this approach, three different hand-crafted methods have been used in order to do the face recognition task, namely Principal Component Analysis (PCA) (Rani et al., 2022), Local Binary Patterns (LBP) (Kulkarni et al., 2017) and Histogram of Oriented Gradients (HOG) (Ahamed et al., 2018). All the experimental works are conducted on state-of-the-art datasets, namely Cross-Age Labeled Faces in the Wild (CALFW) (Zheng et al., 2017) and Masked Labeled Faces in the Wild (MLFW) (Wang et al., 2022). Sample images from both datasets are shown in Figure 1. We propose a feature-level fusion approach using LBP and HOG for the recognition of masked and unmasked facial images.

In the rest of the paper, PCA, LBP and HOG feature extraction methods are explained in the next section. After that, the proposed method using feature-level fusion strategy is discussed. Experimental results and comparison with the state-of-the-art models are given in the next section and finaly, the conclusions are stated in the last section of this paper.

Figure 1. Sample Images from CALFW (top) and MLFW (bottom) Datasets

FEATURE EXTRACTION AND RECOGNITION

In general, feature extraction is the reduction of the complexity of the input images while preserving the most important information for a specific task. There are many feature extraction techniques such as:

• Hand-crafted feature extraction methods that use one's own experience and knowledge to determine which traits are important for a certain job. Examples include Principal Component Analysis, Histograms of Oriented Gradients, Speeded Up Robust Features (SURF), Linear Discriminant Analysis (LDA), Local Binary Patterns, Scale-Invariant Feature Transform (SIFT) and Gabor Filter.

• Deep Learning-based feature extraction approaches that directly discover features from the data using deep neural networks. Convolutional Neural Networks (CNNs) and Recurrent Neural Networks (RNNs) are used often in this circumstance.

• Hybrid feature extraction methods that are about combining traditional feature extraction with that performed by deep neural networks.

Hand-crafted feature extraction methods used in this study are Principal Component Analysis, Local Binary Patterns and Histogram of Oriented Gradients. PCA is a widely used method for feature extraction over a several disciplines, including but not limited to pattern recognition, computer vision, and image processing. The original data are transformed using a linear method into a reduced-dimensional subspace, in which the directions with the highest variance in the data are retained, and the others are discarded (Rani et al., 2022).

In the areas of pattern recognition, computer vision, and image processing, LBP is implemented as a feature extraction approach. It is particularly useful for texture analysis and image classification tasks. LBP's underlying premise is generating a binary pattern for each pixel in a picture based on the surrounding pixels' intensity levels. The LBP operator contrasts a central pixel's intensity value with the intensity values of the pixels around it, and the output is a binary code that represents the local texture around that pixel (Kulkarni et al., 2017).

The feature extraction technique known as HOG is widely utilized in computer vision and pattern recognition, especially for object detection tasks. The primary premise of HOG is to compute the distribution of gradient orientations in an image, which captures the shape and structure of an object (Ahamed et al., 2018).

PROPOSED METHOD

Feature extraction, normalization, standardization, matching and classification are the main components of the proposed method used in this study.

The LBP and HOG approaches are combined to create the feature-level Fusion strategy employed in this research. Initially, HOG and LBP features are retrieved from each image using this handcrafted approach. As we extract different type of features using our methods, normalization is applied to both feature vectors. It helps our data points to be in the same domain so it would be possible to concatenate and compare them with each other. After normalization, concatenation is applied to both normalized feature vectors in order to get a concatenated fused feature vector. Finally, the fusion vector related to each image in the training set is used in the matching process with the test images. Block diagram of the proposed method is shown in Figure 2.

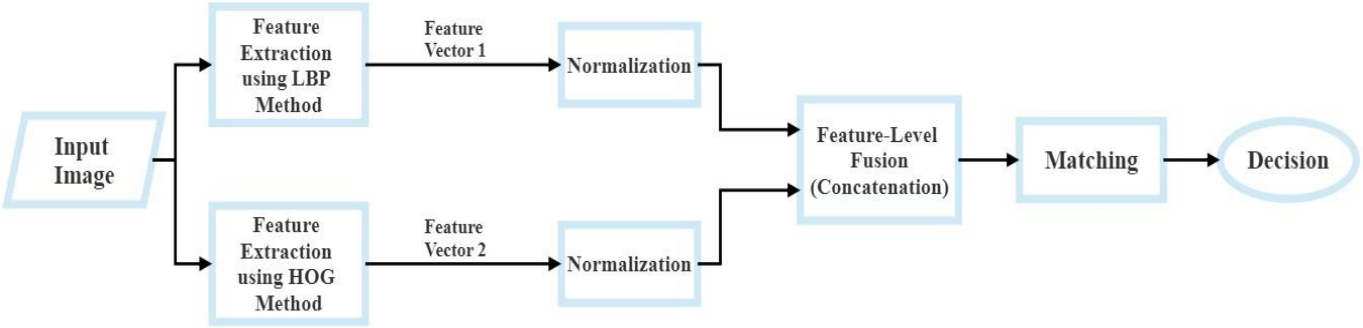

Figure 2. Block Diagram of the Proposed Method

EXPERIMENTAL RESULTS

The experiments are implemented using MATLAB 2022a by a computer with Intel i7 processor (10th gen.) and 16 GB of RAM. The experiments are typically organized into three sections to further illustrate the performance. The first section involves training and testing with masked images of faces. The second section involves training with masked face images and testing with the unmasked ones. The third experiments use unmasked and masked face images for training and evaluation respectively.

Experiments using Different Datasets

The outcomes of the tests, which are carried out on several datasets, are as follows. Every feature extractor is applied on each database in three different experimental setups. Features from each and every train set are retrieved, and a handcrafted classifier is used to match those features. In the first experimental setup, all of the images are from MLFW dataset with 500 images used for train and 500 images used for testing. The total number of images that is used for train and test in the second and the third experimental setups are equal to the numbers used in the first experiments. However, for the second experimental setup, train images are chosen from MLFW dataset, test images are chosen from CALFW dataset and in the 3rd experimental setup it is vice versa. Information about datasets used in this study for three experimental setups are shown in Table 1.

Table 1. Information about Datasets Used in Experimental Setups

Experimental Setup	Train Set	Train Image per Person	Total number of Train Images	Test Set	Test Image per Person	Total number of Test Images	Total number of Individuals	Total number of Images
I	MLFW	1	500	MLFW	1	500	500	1000
II	MLFW	1	500	CALFW	1	500	500	1000
III	CALFW	1	500	MLFW	1	500	500	1000

Experimental Setup I

In the first experimental setup, all feature extraction methods are employed for the masked face recognition after being trained on images of masked faces. Moreover, images for this experimental setup have been chosen from the MLFW dataset. The final results have been measured in both cases so that we can train the program with the first image and test with the second one, or vice versa. Table 2 illustrates the observations.

Table 2. Recognition Rates Using the Experimental Setup I on MLFW Dataset

Feature Extractor	Train Image (MLFW)	Test Image (MLFW)	Accuracy
PCA	1st	2nd	70.2 %
LBP	1st	2nd	93.2 %
HOG	1st	2nd	93.2 %
Proposed Method	1st	2nd	94.2 %
PCA	2nd	1st	68.8 %
LBP	2nd	1st	93.6 %
HOG	2nd	1st	92.8 %
Proposed Method	2nd	1st	94.8 %

It is apparent that in this study, the results from the Proposed, LBP, and HOG methods are all above 90% and very similar to each other, however, the PCA method does not perform well as these three methods. The proposed method has the highest recognition rate in both scenarios, with 1% or more improvement over the other methods.

Experimental Setup II

In the second part of the experiments, all feature extraction methods are used to recognize unmasked faces after being trained on images of faces with masks. Masked face images are chosen from the MLFW dataset in this scenario, while unmasked face images are chosen from the CALFW dataset. Also, images are split evenly so that half are utilized for learning and the other half for testing. Table 3 displays the findings.

Table 3. Recognition Rates Using the Experimental Setup II on MLFW and CALFW Datasets

Feature Extractor	Train Image (MLFW)	Test Image (CALFW)	Accuracy
PCA	Masked	Unmasked	45.6 %
LBP	Masked	Unmasked	57.6 %
HOG	Masked	Unmasked	57.6 %
Proposed Method	Masked	Unmasked	64.8 %

It can be seen that the proposed method has the highest recognition rate with over 7% improvement compared to the accuracy of the other feature extraction methods. Following the proposed method, LBP and HOG methods have the same recognition rate, and finally, PCA method is at the bottom with a recognition rate under 50%.

Experimental Setup III

In the third phase of the experiments, all feature extraction algorithms are utilized to distinguish masked faces following training on images of unmasked faces. In this situation, face images with masks are selected from the MLFW dataset, whereas face images without masks are selected from the CALFW dataset. Table 4 provides a summary of the results.

Table 4. Recognition Rates Using the Experimental Setup III on CALFW and MLFW Datasets

Feature Extractor	Train Image (CALFW)	Test Image (MLFW)	Accuracy
PCA	Unmasked	Masked	30.4 %
LBP	Unmasked	Masked	58.0 %
HOG	Unmasked	Masked	58.0 %
Proposed Method	Unmasked	Masked	58.6 %

In the third experimental setup, when algorithms initially trained by unmasked images and then evaluated on masked ones, the proposed method, along with LBP and HOG methods, produce the best results with a recognition rate of near 60%.

Comparison with State-of-the-Art Models

At the conclusion of these experimental activities, the proposed method results relevant to this study are compared with various state-of-the-art models. These open sourced state-of-the-art deep face recognition methods are as follows: (1) ResNet50 model trained on a private Asia face dataset (Wang et al., 2021) with ArcFace (Deng et al., 2019), (2) ResNet50 model trained on CASIAWebFace database (Yi et al., 2014) with ArcFace (Deng et al., 2019), (3) ResNet50 model trained on VGGFace2 database (Cao et al., 2018) with ArcFace (Deng et al., 2019), (4) ResNet100 model trained on MS1MV2 database (Guo et al., 2016) refined by insightface with ArcFace (Deng et al., 2019), (5) ResNet100 model trained on MS1MV2 database (Guo et al., 2016) with CurricularFace (Huang et al., 2020), (6) ResNet100 model trained on MS1MV2 database (Guo et al., 2016) with SFace (Zhong et al., 2021).

All of these state-of-the-art methods are compared to the proposed method in this study in terms of accuracy using Cross-age LFW (CALFW) and Masked LFW (MLFW) datasets. It is important to note that, for the proposed method, CALFW and MLFW datasets are used in different cases in order to train the model, while for those deep learning methods, different benchmarks using various loss functions were used for this purpose. The comparison results are shown in Table 5.

In the masked face recognition task, the proposed method in this approach has better performance compared to the deep learning methods presented in Table 5. Overall, hand-crafted methods are easier to implement while they need less powerful hardware next to taking less amount of time for doing the different tasks in comparison with the deep learning methods that need much more powerful hardware and also take more time to be implemented and do different tasks. It is clear that deep learning methods are the latest technology that is employed for doing different tasks but it does not mean that it is always better than the traditional or older methods as shown in this study. It is

critical to note that MLFW dataset was used as a training set in this study, as opposed to other datasets which have high computational cost and computation time for training deep learning models.

Table 5. Comparison of the Proposed Method with the State-of-the-Art Models

Reference	Method	Train Set	Accuracy on CALFW	Accuracy on MLFW
Wang et al. (2021)	ResNet50 (ArcFace)	Private-Asia	91.12 %	74.85 %
Yi et al. (2014)	ResNet50 (CosFace)	Casia-WebFace	92.43 %	82.87 %
Cao et al. (2018)	ResNet50 (ArcFace)	VGGFace2	93.72 %	85.02 %
Guo et al. (2016)	ResNet100 (ArcFace)	MS1MV2	95.83 %	90.13 %
Guo et al. (2016)	ResNet100 (Curricularface)	MS1MV2	95.97 %	90.60 %
Guo et al. (2016)	ResNet100 (SFace)	MS1MV2	95.83 %	90.63 %
Proposed Method	Feature-level Fusion of HOG and LBP	MLFW	64.80 %	94.80 %
		CALFW	52.80 %	58.60 %

CONCLUSION

In this approach, an in-depth examination of various analyses of facial recognition algorithms are undertaken by measuring the efficiency of four methods for extracting features, namely Local Binary Patterns (LBP), Histogram of Oriented Gradients (HOG), Principal Component Analysis (PCA) and a custom-designed proposed method using the feature-level fusion of LBP and HOG methods. Furthermore, a handcrafted classifier is applied to assess the precision of the recognition procedure. The experiments are conducted using two benchmark datasets namely, the Cross-Age LFW (CALFW) and Masked Labeled in the Wild (MLFW). These datasets are selected because they are widely employed in the area of facial recognition and offer a trustworthy assessment of the performance of the systems under investigation. The findings are analyzed and compared to determine the effectiveness of each method. The study also aims to identify any potential limitations and areas for further improvement in the field of face recognition.

This study indicates that when it comes to recognizing masked faces using a training set of masked face images, the proposed method outperformed the other feature extraction methods, while HOG and LBP methods have nearly similar performance to the proposed method. In the case of recognizing masked faces using a training set of unmasked face images, the proposed method has the highest performance, followed by Local Binary Patterns and Histogram of Oriented Gradients methods, which have comparable accuracy levels. When it comes to recognizing unmasked faces using a training set of masked faces, the proposed method again is the most accurate one, and the performance of the Local Binary Patterns and Histogram of Oriented Gradients methods are equivalent.

It is important to note that, machine learning and deep learning methodologies are constantly evolving. Regarding future work, it would be beneficial to use more benchmark unmasked and masked face image datasets that include a variety of illumination angles and rotation variations, as well as incorporating other feature extraction methods based on deep learning techniques.

REFERENCES

Ahamed, H., Alam, I. and Islam, M. M. (2018), HOG-CNN Based Real Time Face Recognition, 2018 International Conference on Advancement in Electrical and Electronic Engineering (ICAEEE), 2018, pp. 1-4, doi: 10.1109/ICAEEE.2018.8642989.

Cao, Q., Shen, L., Xie, W., Parkhi, O. M. and Zisserman, A. (2018), VGGFace2: A Dataset for Recognising Faces across Pose and Age, 2018 13th IEEE International Conference on Automatic Face & Gesture Recognition (FG 2018), Xi'an, China, 2018, pp. 67-74, doi: 10.1109/FG.2018.00020.

Deng, J., Guo, J., Xue, N. and Zafeiriou, S. (2019), ArcFace: Additive Angular Margin Loss for Deep Face Recognition, 2019 IEEE/CVF Conference on Computer Vision and Pattern Recognition (CVPR), Long Beach, CA, USA, 2019, pp. 4685-4694, doi: 10.1109/CVPR.2019.00482.

Guo, Y., Zhang, L., Hu, Y., He, X., and Gao, J. (2016), MS-Celeb-1M: A Dataset and Benchmark for Large-Scale Face Recognition, Sep. 17, 2016. https://link.springer.com/chapter/10.1007/978-3-319-46487-9-6

Huang, Y. et al. (2020), CurricularFace: Adaptive Curriculum Learning Loss for Deep Face Recognition, 2020 IEEE/CVF Conference on Computer Vision andPattern Recognition (CVPR), Seattle, WA, USA, 2020, pp. 5900-5909, doi: 10.1109/CVPR42600.2020.00594.

Kulkarni, O. S., Deokar, S. M., Chaudhari, A. K., Patankar, S. S. and Kulkarni, J. V. (2017), Real Time Face Recognition Using LBP Features, 2017 International Conference on Computing, Communication, Control and Automation (ICCUBEA), 2017, pp. 1-5, doi: 10.1109/ICCUBEA.2017.8463886.

Rani, G. E., Suresh, S. M, M. P., Abhiram, M., Surya, K. J. and Kumar, B. Y. A. N. (2022), Face Recognition Using Principal Component Analysis, 2022 2nd International Conference on Advance Computing and Innovative Technologies in Engineering (ICACITE), 2022, pp. 932-936, doi: 10.1109/ICACITE53722.2022.9823434.

Wang, C., Fang, H., Zhong, Y., and Deng, W. (2022), MLFW: A Database for Face Recognition on Masked Faces, In: et al. Biometric Recognition. CCBR 2022. Lecture Notes in Computer Science, vol 13628. Springer, Cham. 2022. doi: 10.1007/978-3-031-20233-9-18.

Wang, Q., Zhang, P., Xiong, H., and Zhao, J. (2021), Face.evoLVe: A High-Performance Face Recognition Library, arXiv.org, Jul. 19, 2021. https://arxiv.org/abs/2107.08621v4

Yi, D., Lei, Z., Liao, S., and Li, S. Z. (2014), Learning Face Representation from Scratch, arXiv.org, Nov. 28, 2014. https://arxiv.org/abs/1411.7923v1

Zheng, T., Deng, W., and Hu, J. (2017), Cross-age LFW: A database for studying cross-age face recognition in unconstrained environments, CoRR, vol. abs/1708.08197, 2017.

Zhong, Y., Deng, W., Hu, J., Zhao, D., Li, X. and Wen, D. (2021), SFace: Sigmoid- Constrained Hypersphere Loss for Robust Face Recognition, in IEEE Transactions on Image Processing, vol. 30, pp. 2587-2598, 2021, doi: 10.1109/TIP.2020.3048632.

KSÜ Mühendislik Bilimleri Dergisi, 26(Özel Sayı), 2023 KSU J Eng Sci, 26(Special Issue), 2023
9th Uluslararası IFS Çağdaş Matematik ve Mühendislik Konferansı Özel Sayısı
9th International IFS Contemporary Mathematics and Engineering Conference Special Issue
Araştırma Makalesi Research Article

Kahramanmaras Sutcu Imam University
Journal of Engineering Sciences

Geliş Tarihi : 09.08.2023 Received Date : 09.08.2023
Kabul Tarihi : 05.09.2023 Accepted Date : 05.09.2023

INVESTIGATION OF THE EFFECT OF NANOPARTICLE ADDITIVES ON THE REFRACTIVE INDEX AND DENSITY OF GASOLINE

NANOPARTİKÜL İLAVESİNİN BENZİNİN KIRILMA İNDİSİ VE YOĞUNLUĞU ÜZERİNDEKİ ETKİSİNİN ARAŞTIRILMASI

Mehmet Selman GÖKMEN [1*] (ORCID: 0000-0001-5943-7504)
Mehmet Fatih PARLAK [2] (ORCID: 0009-0000-8410-6547)
Hasan AYDOĞAN [3] (ORCID: 0000-0003-1404-6352)

[1] Necmettin Erbakan University, Seydişehir Vocational High School, Department of Motor Vehicles and Transportation Technologies., Konya TÜRKİYE
[2] Şifa Kimya Pharmaceuticals Cosmetics Industry and Trade Inc., Manager of Quality Control Department, Konya TÜRKİYE
[3] Selcuk University, Technology Faculty, Department of Mechanical Engineering, Campus, Konya TÜRKİYE

*Sorumlu Yazar / Corresponding Author: Mehmet Selman GÖKMEN, msgokmen@erbakan.edu.tr

ABSTRACT

In this study, the use of Al_2O_3 and TiO_2 nano particles with a size of 12 nm and a purity of 99.9% as gasoline fuel additives was investigated. Fuel mixtures were prepared using a 3-level factorial design technique, and density and refractive index values were determined. Al_2O_3 nano particles, due to their high surface area, increased the density by 0.17% (3.5 ppm) and 1.22% (7 ppm), while TiO_2 nano particles increased the density by 0.22% (3.5 ppm) and 1.26% (7 ppm). It was observed that the nano particle with a higher surface area had a less significant effect on density. The refractive index values decreased by 0.11% (3.5 ppm) and 0.14% (7 ppm) for Al_2O_3 nano particles, and by 0.21% (3.5 ppm) and 0.24% (7 ppm) for TiO_2 nano particles. This study highlighted the importance of particle size, purity, and surface area in the selection of nano particles. Based on the evaluations and preliminary tests, nano particle levels above 15 ppm exhibited a tendency for agglomeration in the fuel. It is crucial to limit the total concentration to 15 ppm, especially for nano particles with a high surface area like Al_2O_3, to achieve homogeneous fuel.

Keywords: Aluminum oxide, titanium dioxide, gasoline additive, refractive ındex, density

ÖZET

Bu çalışmada, 12 nm boyutunda ve %99.9 saflıktaki Al_2O_3 ve TiO_2 nano partiküllerinin benzin yakıt katkı maddesi olarak kullanımı incelenmiştir. Partikül ilave edilen yakıt karışımlarının yoğunluk ve kırılma indisi değerleri benzin yakıtıyla karşılaştırılmıştır. 3 seviyeli faktöriyel tasarım tekniği kullanılarak yakıt karışımları elde edilmiş, yoğunluk ve kırılma indisi değerleri belirlenmiştir. Sonuçlar, Al_2O_3 nano partikülünün yüksek yüzey alanı nedeniyle yoğunluğu %0,17 (3.5 ppm) ve %1,22 (7 ppm) oranında artırdığını göstermiştir. TiO_2 nano partikülünün ise yoğunluğu %0,22 (3.5 ppm) ve %1,26 (7 ppm) oranında artırdığı belirlenmiştir. Yüzey alanı yüksek olan nano partikülün yoğunluk üzerinde daha az etkili olduğu görülmüştür. Kırılma indisi değerleri ise Al_2O_3 nano partikülünde %0,11 (3.5 ppm) ve %0,14 (7 ppm) azalırken, TiO_2 nano partikülünde ise %0,21 (3.5 ppm) ve %0,24 (7 ppm) azaldığı tespit edilmiştir. Bu çalışma, nano partikül seçiminde boyut, saflık ve yüzey alanının önemli olduğunu ortaya koymuştur. Yapılan değerlendirmeler ve ön testler neticesinde, 15 ppm üzerindeki nano partikül seviyelerinin yakıt içerisinde topaklanma eğilimi göstermektedir. Özellikle yüksek yüzey alanına sahip Al_2O_3 gibi nano partiküller için toplam oranın 15 ppm'yi

ToCite: GÖKMEN, M. S., PARLAK, M. F., & AYDOĞAN, H. (2021). INVESTIGATION OF THE EFFECT OF NANOPARTICLE ADDITIVES ON THE REFRACTIVE INDEX AND DENSITY OF GASOLINE. *Kahramanmaraş Sütçü İmam Üniversitesi Mühendislik Bilimleri Dergisi*, 26(Özel Sayı), 1140-1146.

aşmaması homojen bir yakıt elde edilmesi için önemli bir parametredir.

Anahtar Kelimeler: Alüminyuma oksit, titanyum dioksit, benzin katkı maddesi, kırılma indisi, yoğunluk

INTRODUCTION

Globally, the demand for energy is continuously increasing due to the growing world population. Among various energy sources, gasoline fuel derived from the refining of crude oil plays a crucial role as a primary energy source in numerous industrial applications, including automobiles, aircraft, and agricultural machinery. As the world population expands, so does the number of vehicles on the roads. The transportation sector heavily relies on gasoline fuel to meet its energy needs. Automobiles, being the most common mode of transportation, heavily depend on gasoline for their operations. Similarly, aircraft and agricultural machinery also heavily rely on gasoline as their primary fuel source.(Acaroğlu et al., 2018). This situation brings along with it the problems of environmental pollution caused by exhaust emissions, depletion of oil reserves, and disruption of supply-demand balance. The characteristics that fuels should meet are determined by international standards, and gasoline engine manufacturers produce engines that comply with these standards. However, these standards prioritize acceptable engine performance and emission values, focusing on cost-effective production. (Reif, 2015). The reason why different countries worldwide develop their gasoline formulations in their domestic refineries, particularly considering the climatic and geographical conditions of developed countries, is because international standards allow flexibility in gasoline composition. In Europe, for example, there are various gasoline options such as 95, 98, and 100 octane, while in the United States, fuels with higher oxygen content that provide better performance in winter conditions are commercially available. These variations in gasoline formulations allow countries to cater to their specific regional needs and optimize performance under different environmental conditions.

Gasoline additives used in fuel can be categorized based on their properties as anti-knock agents, stabilizers, corrosion inhibitors, combustion enhancers, and detergent additives. (Srivastava & Hancsók, 2014). Although commonly used gasoline additives include chemicals such as aromatics, phenols, phosphorus, and lead tetraethyl, nano particles can also be used as additives in fuel (Kotia et al., 2020). Nano particles with sizes ranging from 1 to 100 nm exhibit extraordinary properties due to their small size and often behave differently from larger structures. As the size decreases, the chemical activation and surface area of the particles increase. Increased chemical activation enhances the particles' ability to interact with the surrounding environment, while increased surface area increases the number of particles per unit volume. Smaller-sized materials also have a reduced number of chemical bonds per unit area. Consequently, as particle size decreases, their melting points significantly decrease. For example, the melting temperature of gold in bulk structures is 1337 K, whereas for particles with a size of 6 nm, it decreases by approximately 200 K. (Naito et al., 2018). One of the most important factors contributing to the increased chemical activation of materials as their size decreases is the increase in surface area. The increased surface area enhances the material's propensity for reactions and chemical behavior, making nano-sized materials much more reactive compared to bulk materials. Therefore, the addition of a small amount of nanoparticle can effectively enhance the properties of fuels (Khan et al., 2022; Dehhaghi et al., 2021; Hatami et al., 2020; Karmakar, 2012).

Density is one of the properties that gasoline fuel needs to meet, which measures the amount of substance within a given volume. Density is directly proportional to the amount of substance in a given volume. Refractive index, on the other hand, is a parameter that measures the amount of reflection or transmission of electromagnetic waves by a fuel (Gahlyan et al., 2020). This parameter is related to the dielectric function of the fuel, and the value of the dielectric function is dependent on the density of the fuel's electric polarization. This means that the reflection or transmission of electromagnetic waves by fuels is dependent on their densities. Generally, denser fuels have lower refractive indices because dense materials have more intense electric polarizations, resulting in less reflection or transmission of waves (Nita et al., 2016; Nikolaev et al., 2015). Similarly, less dense fuels have higher refractive indices because the electric polarizations of less dense materials are less intense, resulting in more reflection or transmission of waves.

There is insufficient research available in the literature regarding the density and refractive index of nano-particles added to gasoline fuel. Density, which is an important property providing information about fuel classification, calorific value, and knock resistance, along with the refractive index value that provides information about hydrocarbon content, were determined through measurements using fuel blends obtained by adding Al_2O_3 and TiO_2

nano-particles in different proportions to gasoline fuel. The aim of this study was to elucidate the effects of nano-particle additives on the density and refractive index values of gasoline.

MATERİAL AND METHOD

Fuel blends were prepared using 12 nm-sized Al_2O_3 particles and TiO_2 particles with a purity of 99.9%. Pre-screening tests were conducted to determine the fuel ratios, and the total particle concentration was limited to a maximum of 14 ppm due to observed agglomeration when exceeding 15 ppm. Ultrasonic homogenizer and mechanical mixer were used during the preparation of the blends to ensure the uniform dispersion of particles in the fuel. As shown in Table 1, a factorial design method with 3 levels was used for each nano-particle, resulting in 8 mixtures containing particles. Shell's FuelSave unleaded gasoline was used as the base fuel for comparison. The fuel and particle specifications used in the tests are provided in Table 2.

Table 1: Nano Particle Blending Ratios

Factors	***Levels***		
Al_2O_3 (ppm)	*0*	*3.5*	*7*
TiO_2 (ppm)	*0*	*3.5*	*7*

Table 2: Fuel Specifications

Feature	**Gasoline**	**Aluminium Oxide**	**Titanium Dioxide**
Molecular Formula	C_XH_Y	Al_2O_3	TiO_2
Molecular Weight (g/mol)	-	101.96	79.86
Density (g/cm³)	0,740	3.94	4.23
Flashing Point (°C)	<-40	-	-
Auto Ignition Point (°C)	>250	-	-
Octane Number	95	-	-
Thermal Conductivity (W/mK)	120	30	11.8
Boiling Point (°C)	47	2977	2972
Lov Heat Value (kJ/kg)	43430	-	-

The density measurements of the 8 different fuel blends containing nano particles were conducted at 20°C using a Mettler Toledo DensitoPro device and compared to standard gasoline, as provided in Table 3. Additionally, the refractive index values of the fuel blends were measured using a Rudolph Research J357 refractometer with the specifications given in Table 4. All measurements were performed with 5 repetitions, and the averages were calculated.

Table 3: Density Measurement Device Specifications

Feature	**Attribute**
Model	MT DensitoPro
Measurement Range	0 - 3 g/cm³
Sensitivity	±0,001 g/cm³
Repeatability	±0,0005 g/cm³
Resolution	0,0001 g/cm³
Sample Temp Range	0 - 50 °C

Table 4: J357 Refractometer Specifications

Feature	Attribute
Model	RR J357 Refraktometre
Measurement Range	1.26 - 1.72
Resolution	0.00001
Repeatability	±0.00002
Sensitivity	±0.00002
Optical Wave Length	589.3 nm
Prism Structure	Synthetic Sapphire
Temp Control Range	10º C - 100º C
Temp Control Sensitivity	±0.05º C
Ambiennt Temp Limit	5ºC - 40º C

Research Findings

According to the measurements, for both nano particles, it was observed that the density value of the fuel without Al_2O_3nano particles (gasoline) was 0.7402 g/cm3, while it increased to 0.7415 g/cm3 with a nano particle concentration of 3.5 ppm, as shown in Figure 1. This indicates an increase in density by 0.17%. When the nano particle concentration was increased to 7 ppm, the density value reached 0.7493 g/cm3, corresponding to a 1.22% increase. Regarding the refractive index values, it was found that the highest value was 1.42302 for the gasoline fuel. In the fuel blend with 3.5 ppm Al_2O_3 nano particles (Fuel 2), this value decreased by 0.11% to 1.42134. In the fuel blend with 7 ppm Al_2O_3 (Fuel 3), there was a 0.14% decrease, and the refractive index level was measured as 1.42096.

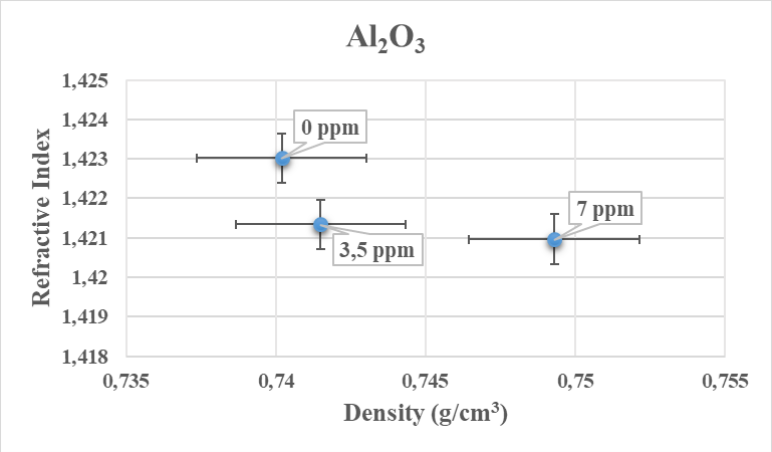

Figure 1: The Effect of Al_2O_3 Nano Particles on Refractive İndex and Density

According to Figure 2, the effect of TiO_2 nano particles on the refractive index and density values is presented. The fuel with 3.5 ppm TiO_2 nano particles showed an increase in density by 0.22% compared to gasoline fuel, with a measured value of 0.7419 g/cm3. In the fuel with 7 ppm TiO_2, the density value further increased by 1.26% to reach 0.7496 g/cm3. The refractive index value decreased by 0.21% in the fuel with 3.5 ppm TiO_2 nano particles, measuring 1.41997, and decreased by 0.24% in the fuel with 7 ppm TiO_2 nano particles, measuring 1.41959. Considering the current situation, the changes in density and refractive index caused by both nano particle additives are within the acceptable range and in compliance with ASTM standards.

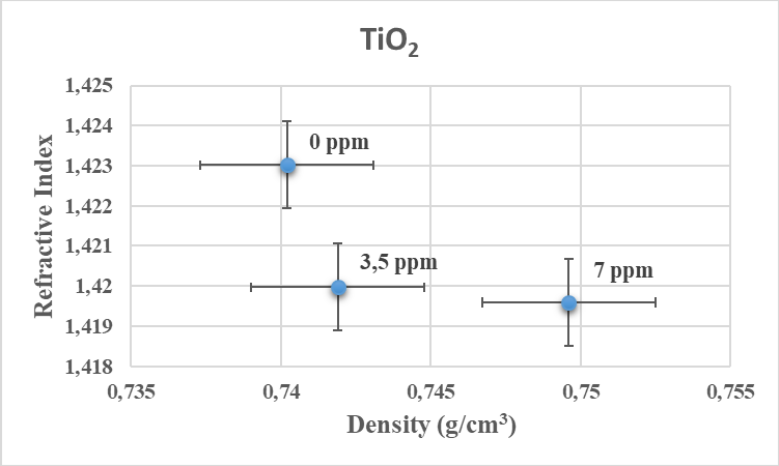

Figure 2: The Effect of TiO_2 Nano Particles on Refractive İndex and Density

All measurements conducted for the mixture quantities obtained through the 3-level factorial design technique are presented in Table 5. Prediction functions were derived from the data obtained in the table using the 3-level factorial design technique. These equations enable the prediction of density and refractive index values. The 1st equation, derived as a function of nano particle quantities, allows for the prediction of density values, while the 2nd equation enables the prediction of refractive index values with an accuracy of over 90%.

Table 5: Measurement Results of All Blends

Fuel	Al_2O_3 (ppm)	TiO_2 (ppm)	Density (g/cm³)	Ref. Index
Gasoline	0	0	0.7402	1.42302
Fuel 1	3.5	0	0.7415	1.42134
Fuel 2	7	0	0.7493	1.42096
Fuel 3	0	3.5	0.7419	1.41997
Fuel 4	3.5	3.5	0.7444	1.41989
Fuel 5	7	3.5	0.7468	1.41982
Fuel 6	0	7	0.7496	1.41959
Fuel 7	3.5	7	0.7501	1.41929
Fuel 8	7	7	0.7518	1.41813

$$Density = 0{,}74211 + 0{,}00216327 * Al_2O_3 + 0{,}000196599 * TiO_2 - 0{,}000132945 * {Al_2O_3}^2 - 0{,}000142274 * Al_2O_3 * TiO_2 + 0{,}0000833819 * TiO2^2 \quad (1)$$

$$Refraktive\ Index = 1{,}42256 - 0{,}000260476 * Al_2O_3 - 0{,}000721429 * TiO_2 + 0{,}00000612245 * {Al_2O_3}^2 + 0{,}0000122449 * Al_2O_3 * TiO_2 + 0{,}0000404082 * {TiO_2}^2 \quad (2)$$

RESULTS

In this study, fuel mixtures were prepared by mixing Al_2O_3 and TiO_2 nano particles with particle sizes of 12 nm and purity of 99.9%, and surface areas of 378.80 m2/g and 48.8 m2/g, respectively, with gasoline at concentrations of 0, 3.5, and 7 ppm. The refractive index and density values of the fuel mixtures were compared with those of gasoline. The quantities of the fuel mixtures were determined using the 3-level factorial design technique, and prediction functions were obtained. The comparison revealed that the Al_2O_3 nano particle with higher surface area increased the density by 0.17% at the 3.5 ppm level and by 1.22% at the 7 ppm level. On the other hand, the TiO_2 nano particle with lower surface area increased the density by 0.22% at the 3.5 ppm level and by 1.26% at the 7 ppm level. Despite having the same particle size and

purity ratios, the different surface areas of the nano particles caused variations in their densities, with the higher surface area particle having a lower impact on density. The refractive index values decreased by 0.11% and 0.14% at the 3.5 ppm and 7 ppm levels, respectively, for the Al_2O_3 nano particle. Similarly, for the TiO_2 nano particle, there was a decrease of 0.21% and 0.24% at the 3.5 ppm and 7 ppm levels, respectively. These results fall within the acceptable range according to ASTM standards. This study highlighted the importance of particle size, purity, and surface area in the selection of particles added to gasoline. Preliminary screening tests revealed a tendency for particle aggregation in gasoline at levels above 15 ppm. Particularly, ensuring that the total ratio of high-surface-area nano particles does not exceed 15 ppm can prevent aggregation. The study demonstrated that the use of Al_2O_3 and TiO_2 nano particles can affect fuel properties in internal combustion engines, emphasizing the need for further research. The findings will contribute to a better understanding of how the addition of nano particles to gasoline can affect engine performance and emissions.

FUNDİNG

This study was supported by the Scientific Research Projects Coordinatorship of Selçuk University with the project number *21211039*.

REFERANCES

Acaroğlu, M., Aydoğan, H., & Özçelik, A. E. (2018). *Yakıtlar ve Yanma*. Nobel Akademi Yayıncılık.

Dehhaghi, M., Kazemi Shariat Panahi, H., Aghbashlo, M., Lam, S. S., & Tabatabaei, M. (2021). The effects of nanoadditives on the performance and emission characteristics of spark-ignition gasoline engines: A critical review with a focus on health impacts. *Energy*, *225*. https://doi.org/10.1016/j.energy.2021.120259

Gahlyan, S., Bhagat, P., Devi, R., Verma, S., Rani, M., & Maken, S. (2020). Thermodynamics of ternary mixtures with gasoline additive: Volumetric, acoustic and optical properties. *Journal of Molecular Liquids*, *304*. https://doi.org/10.1016/j.molliq.2020.112740

Hatami, M., Hasanpour, M., & Jing, D. (2020). Recent developments of nanoparticles additives to the consumables liquids in internal combustion engines: Part I: Nano-fuels. *Journal of Molecular Liquids*, *318*, 114250. https://doi.org/10.1016/j.molliq.2020.114250

Karmakar, S. (2012). *Energetic Nanoparticles as Fuel Additives for Enhanced Performance in Propulsion Systems* (Issue August) [Doctoral Dissertation]. Lousiana State University.

Khan, S., Dewang, Y., Raghuwanshi, J., Shrivastava, A., & Sharma, V. (2022). Nanoparticles as fuel additive for improving performance and reducing exhaust emissions of internal combustion engines. In *International Journal of Environmental Analytical Chemistry* (Vol. 102, Issue 2, pp. 319–341). Taylor and Francis Ltd. https://doi.org/10.1080/03067319.2020.1722810

Kotia, A., Chowdary, K., Srivastava, I., Ghosh, S. K. ve Ali, M. K. A., 2020, Experimental investigation the effect of Mn2O3 nanoparticle on the performance and emission of SI gasoline fueled with mixture of ethanol and gasoline, Journal of Molecular Liquids, 310.

Naito, M., Yokoyama, T., Hosokawa, K., & Nogi, K. (2018). Nanoparticle Technology Handbook. In *Elseiver* (3.). Elsevier.

Nikolaev, V. F., Tabrisov, I. I., Penkovsky, A. I., & Sultanova, R. B. (2015). Express method for total content assessment of aromatic hydrocarbons and oxygen in finished gasolines by refractometry and densimetry. *Fuel*, *142*, 94–101. https://doi.org/10.1016/j.fuel.2014.10.042

Nita, I., Iulian, O., Geacai, E., & Osman, S. (2016). Physico-chemical Properties of the Pseudo-binary Mixture Gasoline + 1 - Butanol. *Energy Procedia*, *95*, 330–336. https://doi.org/10.1016/j.egypro.2016.09.017

Reif, K. (2015). Gasoline Engine Management Systems and Components. In *Springer Vieweg*. Springer Vieweg.

Srivastava, S. P., & Hancsók, J. (2014). Fuels and Fuel-Additives. In *John Wiley & Sons*. John Wiley & Sons.

KSÜ Mühendislik Bilimleri Dergisi, 26(Özel Sayı), 2023 KSU J Eng Sci, 26(Special Issue), 2023
9th Uluslararası IFS Çağdaş Matematik ve Mühendislik Konferansı Özel Sayısı
9th International IFS Contemporary Mathematics and Engineering Conference Special Issue
Araştırma Makalesi Research Article

Kahramanmaras Sutcu Imam University Journal of Engineering Sciences

Geliş Tarihi : 09.08.2023 Received Date : 09.08.2023
Kabul Tarihi : 08.09.2023 Accepted Date : 08.09.2023

ENDÜSTRİ 4.0 TEMELİNDE ONLİNE ALIŞVERİŞ SİTELERİNİN SEÇİMİNDE DİKKATE ALINACAK KRİTERLERİN DEMATEL YÖNTEMİ İLE DEĞERLENDİRİLMESİ

EVALUATION OF THE CRITERIA TO BE CONSIDERED WHEN SELECTING ONLINE SHOPPING SITES BASED ON INDUSTRY 4.0 WITH DEMATEL METHOD

Zeynep DURMAZ[1*] (ORCID: 0000-0002-6777-5770)
Erdem AKSAKAL[2] (ORCID: 0000-0003-0746-5727)

[1]Atatürk Üniversitesi, Endüstri Mühendisliği Bölümü, Erzurum, Türkiye
[2] Atatürk Üniversitesi, Endüstri Mühendisliği Bölümü, Erzurum, Türkiye

*Sorumlu Yazar / Corresponding Author: Zeynep DURMAZ, zeynepdurmaz325@gmail.com

ÖZET

Son yıllarda teknolojinin hızla gelişmesi ve internet kullanımının artmasıyla birlikte online alışveriş sitelerine olan ilgi daha da artmaktadır. Artan bu tüketici ilgisi göz önüne alındığında, online alışveriş siteleri arasındaki rekabet de her geçen gün artmaktadır. Bu rekabet ortamında tüketicilerin ilgisini çeken ve tercih edilen bir platform olmak büyük önem taşımaktadır. Bu çalışmada Endüstri 4.0 temelinde online alışveriş sitelerinin tercih edilmesinde etkili olan kriterlerin değerlendirilme süreci ele alınmaktadır. Çalışmada dikkat edilecek kriterler; ürün bilgisi ve çeşitliliği, zamanında ve doğru teslimat, web sitesi tasarımı ve performansı, güvenilirlik/gizlilik ve müşteri memnuniyetidir. Bu kriterlerin ilişkilerinin ve önemlerinin belirlenmesinde Çok Kriterli Karar Verme (ÇKKV) yöntemlerinden DEMATEL yöntemi kullanılmıştır. Böylelikle online rekabet ortamında dikkate alınması gereken kriterlerin belirlenme süreci gösterilmiş ve buna katkı sağlayacağı varsayılan kriterler değerlendirilmiştir. Bu değerlendirmeler sonucunda, online alışveriş sitelerinin mevcut durumlarını, Endüstri 4.0 temelinde iyileştirmelerine yönelik öneriler sunulmuştur.

Anahtar Kelimeler: Online alışveriş siteleri, Endüstri 4.0, Çok kriterli karar verme, DEMATEL yöntemi.

ABSTRACT

In recent years, with the rapid development of technology and the increase in internet usage, the interest in online shopping sites is increasing. Considering this increasing consumer interest, competition between online shopping sites is increasing day by day. In this competitive environment, it is of great importance to be a platform that attracts the attention of consumers and is preferred. In this study, the evaluation process of the criteria that are effective in choosing online shopping sites on the basis of Industry 4.0 is discussed. Criteria to be considered in the study; product information and variety, on-time and accurate delivery, website design and performance, reliability/confidentiality and customer satisfaction. DEMATEL method, one of the Multi-Criteria Decision Making (MCDM) methods, was used to determine the relationships and importance of these criteria. Thus, the process of determining the criteria that should be taken into account in the online competitive environment is shown and the criteria that are assumed to contribute to this are evaluated. As a result of these evaluations, suggestions were made to improve the current situation of online shopping sites on the basis of Industry 4.0.

ToCite: DURMAZ, Z., & AKSAKAL, E., (2023). ENDÜSTRİ 4.0 TEMELİNDE ONLİNE ALIŞVERİŞ SİTELERİNİN SEÇİMİNDE DİKKATE ALINACAK KRİTERLERİN DEMATEL YÖNTEMİ İLE DEĞERLENDİRİLMESİ. *Kahramanmaraş Sütçü İmam Üniversitesi Mühendislik Bilimleri Dergisi*, 26(Özel Sayı), 1147-1155.

Keywords: Online shopping sites, Industry 4.0, Multi-criteria decision making, DEMATEL method.

GİRİŞ

Son yıllarda hızla gelişerek günlük hayatımızın önemli bir parçası haline gelen ve dünyada kullanıcı sayısını her geçen gün gittikçe arttırarak faaliyet alanını da devamlı genişleten internet, günümüzde insanların kullandığı iletişim araçlarının en önemlilerinden biri haline gelmiştir. İnternet, bilgisayar sistemlerinin birbirine bağlandığı, tüm dünya çapında kullanımı olan ve sürekli büyümekte olan bir iletişim ağı şeklinde ifade edilmektedir (Yalçın, 2012). Özellikle de genç neslin sıklıkla kullandığı ve vazgeçilmezi olan internet günlük hayatımız içerisinde önemini ve kullanım oranını her geçen gün artırmaktadır.

İnternetin hızla gelişimine bağlı olarak tüketiciler 7/24 alışveriş yapabilecekleri online alışverişe ilgi göstermeye başlayınca, geleneksel alışveriş mağazaları da online ortamda satış yapmaya yönelmişlerdir (Cheung ve Lee, 2006). Bu hızlı değişimle beraber işletmeler, üstün bir başarı elde etmek için birçok farklı konuda kararlar almak zorunda kalmışlardır. Bu süreçte, karar vericilerin, doğru ve güvenilir bilgilere ve değerlendirme tekniklerine ihtiyacı vardır. Çok sayıda alternatif arasında en uygun olan alternatifin seçilmesi sürecinde çelişen ve çok sayıda kriter olduğu için de Çok Kriterli Karar Verme yöntemleri kullanılmaktadır (Soner ve Önüt, 2006).

Gelişen teknolojiye bağlı olarak internet kullanımının artması ve yaşanan Covid-19 pandemi süreci ile birlikte, tüketicilerin alışveriş davranışlarında değişiklikler meydana gelmiş ve online alışverişe olan ilgileri daha da artmıştır. Online alışverişe karşı artan bu ilgi akademisyenler ve sektör içindeki işletmeler tarafından ilgiyle takip edilmiş ve giderek önem kazanan bir konu haline gelmiştir. Yaşanan bu değişim ve gelişim süreci, geleneksel işletmelerin online ortama yönelmesini zorunlu hale getirmiştir. Gerçekleşen bu yönelim doğrultusunda, internet dünyasında hızla büyümekte ve gelişmekte olan online alışveriş siteleri arasındaki rekabet de gün geçtikçe artmaktadır.

Rekabet ortamında, tüketicilerin ürün veya hizmet satın alma sürecini etkileyen faktörleri analiz etmek ve bu analizler doğrultusunda alışveriş sitelerinde iyileştirmeler yapmak sürdürülebilir bir başarıyı yakalayabilmek için çok önemlidir. Bu bağlamda rekabeti yakalayabilmenin en temel yolu ise, çağımızın büyük devrimlerinden biri olan Endüstri 4.0 temelinde alışveriş sitelerini değerlendirip bu doğrultuda iyileştirmeler uygulamaktır. Bu uygulamalar sayesinde, işletmeler online ortamda sürdürülebilir bir başarı avantajı elde edebilecek ve varlıklarını devam ettirebileceklerdir.

Endüstri 4.0 aslında dijital sanayi devrimi şeklinde ifade edilen bilişim teknolojilerinin ve endüstrinin ortaklaşa bir bütünü şeklinde tanımlanabilir. Bir bütün haline gelen ve dijital dönüşümü ifade eden bu kavram ile beraber üretimde verimlilik ve maliyet avantajı gibi işletme düzeyindeki olumlu sonuçlar elde edilmesini sağlamanın yanı sıra, stratejik büyüme, insan kaynağı istihdamı ve yönetimi, eğitim, yatırım gibi uzun vadeli sonuçların ortaya çıkmasına da temel oluşturmaktadır (TÜSİAD, 2016). Endüstri 4.0 ve onun bileşenleri sayesinde teknolojiyi de arkasına alarak yatırım yapan ve finansman sağlayan ülkelerin ve işletmelerin; gelişmişlik düzeylerinde önemli düzeyde artış, çalışanların mesleklerinde ciddi bir farklılaşma ve değişim yaşanacağı öngörülmektedir. Gelecekte ise bu durumun çeşitli sosyal, siyasi ve ekonomik sonuçlar doğuracağı ve böylece her türlü ortamda ilişkileri farklılaştıracağı düşünülmektedir (Petekçi, 2021).

Çalışmanın ilk bölümünde, online alışveriş sitelerinin günümüzdeki öneminden ve çalışma kapsamından söz edilmektedir. Çalışmanın ikinci bölümünde, Çok Kriterli Karar Verme yöntemlerinden yararlanılarak online alışveriş sitelerinin değerlendirilmesi hakkında literatür taramasına yer verilmektedir. Çalışmanın üçüncü bölümünde kullanılan yöntemler açıklanmakta, dördüncü bölümünde ise uygulama adımlarından bahsedilmekte ve son olarak sonuç ve tartışmalar bölümünde ise online alışveriş siteleri için Endüstri 4.0 uygulamaları ile yapılabilecek iyileştirme önerileri yer almaktadır.

LİTERATÜR TARAMASI

Literatürde, online alışveriş sitelerinin değerlendirilmesi farklı yöntemler kullanılarak ele alınmıştır. Bu çalışmalara ilişkin bilgiler aşağıda sırasıyla verilmiştir.

Dündar vd. (2007) çalışmalarında Fuzzy TOPSIS yöntemi ile ilgili bilgiler vermişler ve yöntemin işleyişine açıklık kazandırmak için sanal mağazaların alışveriş sitelerinin değerlendirilmesine yönelik bir uygulama yapmışlardır.

Zhang vd. (2008) çalışmalarında, bir değerlendirme indeks sistemi formüle ederek TOPSIS yönteminin bir uzantısını geliştirmişler ve bu yöntem ile e-ticaret alışveriş sitelerini değerlendirmişlerdir.
Çabuk vd. (2012) çalışmalarında, uzman karar vericilerden oluşan bir grup ile belirlenen kriterler doğrultusunda, özel alışveriş sitelerinin Bulanık TOPSIS yöntemi ile sıralamasını yapmışlardır. İlk sıradaki alışveriş sitesi %67 puanla beğeni alırken, ikinci alışveriş sitesi %66 puanla, 3. ve 4. alışveriş siteleri %59'luk puanla eşdeğer düzeyde beğeni almıştır.

Cavlak (2012) çalışmasında, online alışveriş sitelerinin tercihinde etkili olan kriterlerin önem ağırlıklarını AHP yöntemiyle elde etmiştir. Elde edilen sonuca göre en önemli kriter güvenilirlik/gizlilik olarak bulunmuştur.

Özgüven (2012) çalışmasında, hangi alışveriş sitesinin diğer sitelere göre daha etkin olduğunu belirlerken çok kriterli karar verme yöntemlerinden PROMETHEE yöntemini kullanmıştır.

Nilashi (2015) çalışmasında, en güvenilir alışveriş sitesini seçerken çok kriterli karar verme yaklaşımlarından Analitik Ağ Süreci (AAS) ve Yapay Zeka (AI) yaklaşımlarından bulanık mantığı kullanmıştır.

Gök ve Perçin (2016) çalışmalarında, hizmet kalitesi performansına göre alışveriş sitelerinin tercihinde etkili olan kriterin ağırlıklarını DEMATEL yöntemi ile hesaplayıp AAS yöntemine aktarmışlardır. AAS yönteminden elde edilen verilere göre VIKOR yöntemiyle alışveriş sitelerinin sıralamasını elde etmişlerdir.

Çakır vd. (2018) çalışmalarında, özel alışveriş sitelerinin değerlendirilmesi sürecinde kullanılacak olan kriterlerin ağırlıklarını SWARA yöntemi ile belirlemişler daha sonra sıralama işlemini ise WASPAS yöntemi ile ele almışlardır. Elde edilen sıralama sonucunda en iyi özel alışveriş sitesini kullanıcılara önermişlerdir.

Nguyen (2019) çalışmasında, e-ticaret tasarım platformlarının değerlendirilmesi sürecinde Bulanık VIKOR yöntemini uygulamış ve sayısal bir simülasyon ile süreci göstermiştir.

Li ve Sun (2020) çalışmalarında, başarılı bir B2C e-ticaret alışveriş sitesini tasarlamak için, kriter değerlendirme sürecinde herhangi bir belirsizliği ve griliği en aza indirmek için Bulanık AHP ve TOPSIS-Grey yöntemlerini kullanmışlardır.

Agrawal vd. (2020) çalışmalarında, müşteri memnuniyeti kriterlerine dayalı olarak e-ticaret alışveriş sitelerini Bulanık Analitik Hiyerarşi Süreci (BAHP), Bulanık TOPSIS ve PROMETHEE II yöntemleri ile değerlendirmişlerdir.

Bayır (2020) çalışmasında, uzman karar vericilerin görüşleri ve literatür taramaları neticesinde online alışveriş sitelerini değerlendirmeye yönelik seçim kriterlerini belirlemiştir. Belirlenen kriterlerin ağırlıklarını ise AHP yöntemi ile tespit edip sıralamıştır.

Kaur ve Gupta (2021) çalışmalarında, bir web sitesinin tasarım kalitesini dizin değeri biçiminde ölçmek için Kalite Endeksi Değerlendirme Yöntemi temelli bir yapı oluşturmuşlardır. Çalışmada, tasarım kalitesi hususlarının yeni bir sınıflandırmasını önermiş ve Bulanık DEMATEL yöntemi ile ağırlıklandırma uygulaması yapmışlardır.

Lu vd. (2022), tüketicilerin sınır ötesi e-ticaret platformlarını kullanım niyetlerini etkileyen kriterleri belirlemeye çalışmışlardır. Çalışmalarında DEMATEL ve EDAS yöntemlerini bütünleşik olarak kullanmışlardır.

Tsai vd. (2023), bir gıda dağıtım platformunun değerlendirilmesi ve seçilmesi sürecini DEMATEL, DANP ve modifiye edilmiş VIKOR yöntemi temelinde ele almışlardır.

MATERYAL ve YÖNTEM

Bu çalışmada, literatür araştırması sonucunda online alışveriş sitelerinin tercihinde etkili olacağı düşünülen kriterler "ürün bilgisi ve çeşitliliği", "zamanında ve doğru teslimat", "web sitesi tasarımı ve performansı",

"güvenilirlik/gizlilik" ve "müşteri memnuniyeti" olarak belirlenmiştir (Dündar vd., 2007; Çabuk vd., 2012; Cavlak, 2012; Ömürbek ve Şimşek, 2014; Çakır vd., 2018). Belirlenen bu kriterler, ÇKKV yöntemlerinden DEMATEL yöntemi kullanılarak değerlendirilmiştir.

DEMATEL Yöntemi

Çok kriterli karar verme yöntemlerinden biri olan DEMATEL (The Decision Making Trial and Evaluation Laboratory) Yöntemi; karışık ve iç içe geçmiş problem kümelerindeki kriterlerin birbirleri arasındaki ilişkilerinin tespit edilmesi ve uygulanabilir çözümlerin belirlenmesi amacıyla 1972-1976 yılları arasında Cenevre Battelle Memorial Enstitüsü tarafından geliştirilen bir yaklaşımdır (Li ve Tzeng, 2009). Sebep-sonuç kriterleri arasındaki ilişkiyi sistemin anlaşılır bir yapısal modeline dönüştüren DEMATEL yöntemi, aynı zamanda diğer kriterleri etkileyen en önemli kriterleri önermeye imkân tanımaktadır.

DEMATEL Yöntemi adımları aşağıda gösterilmiştir (Hori ve Shimizu, 1999; Seyed-Hosseini vd., 2005; Chiu vd., 2006 ; Hung vd., 2006 ; Wu ve Lee, 2007 ; Tzeng vd., 2007; Tsai ve Chou, 2009; Aksakal ve Dağdeviren, 2010 ; Derse, 2020).

Adım 1: Direkt-İlişki Matrisinin Oluşturulması

Öncelikle Tablo 1'de gösterilmekte olan ikili karşılaştırma skalası kullanılarak Direkt-İlişki Matrisi (A) elde edilir.

Tablo 1. Karşılaştırma Skalası

Sayısal Değer	Tanım
0	Etkisiz
1	Düşük Etki
2	Orta Etki
3	Yüksek Etki
4	Çok Yüksek Etki

Adım 2: Normalleştirilmiş Direkt-İlişki Matrisinin Oluşturulması

Direkt-İlişki Matrisi (A)'dan yararlanılarak ve aşağıdaki (1) ve (2) eşitlikleri, satır ve sütundaki en küçük değer (k) kullanılarak, esas köşegen değerleri 0 olan Normalleştirilmiş Direkt-İlişki Matrisi (M) elde edilir.

$$M = kxA \tag{1}$$

$$k = Min\left(\frac{1}{\max\limits_{1\leqslant i\leqslant n}\sum_{j=1}^{n}|a_{ij}|}, \frac{1}{\max\limits_{1\leqslant j\leqslant n}\sum_{i=1}^{n}|a_{ij}|}\right) \quad i,j \in \{1,2,3,\dots,n\} \tag{2}$$

Adım 3: Toplam İlişki Matrisinin Elde Edilmesi

Normalleştirilmiş ilişki matrisinin elde edilmesinden sonra Toplam İlişki Matrisi (S), (3) eşitliği kullanılarak elde edilir. Eşitlik içerisinde kullanılan (I) birim matrisi ifade etmektedir.

$$S = M + M^2 + M^3 \dots = \sum_{i=1}^{\infty} M^i = M(I-M)^{-1} \tag{3}$$

Adım 4: Gönderici Grubu ve Alıcı Grubu Hesaplanması

Toplam ilişki matrisindeki sütunlar toplamı (R) ve satırlar toplamı (D) ile ifade edilir. (4), (5) ve (6) eşitliklerinin hesaplamaları ile her bir kriterin diğerlerine olan etki seviyesi ve diğerleriyle ilişki seviyesini belirten D+R ve D-R değerleri elde edilir. Eğer bir kriterin D-R değeri pozitif ise gönderici olarak adlandırılır ve diğer kriterleri daha çok etkileyen gruptadırlar. Ayrıca daha yüksek önceliğe sahiptirler. Eğer D-R değeri negatif ise alıcı olarak adlandırılır ve diğer kriterlerden daha fazla etkilenen gruptadırlar. Ayrıca daha düşük önceliğe sahiptirler. İlaveten D+R değerleri

her bir kriterin diğer kriterlerle arasındaki etkileşim düzeyini göstermektedir. D+R değeri yükseldikçe kriterler arasındaki etkileşim yükselmekte, D+R değeri azaldıkça kriterler arasındaki etkileşim de azalmaktadır.

$$S = \left[s_{i,j}\right]_{nxn}, \quad i,j \in \{1,2,3,\dots,n\} \tag{4}$$

$$D = \sum_{j=1}^{n} s_{i,j} \tag{5}$$

$$R = \sum_{i=1}^{n} s_{i,j} \tag{6}$$

Adım 5: Eşik Değerinin Belirlenmesi ve Etki-Yönlü Graf Diyagramının Elde Edilmesi

Bu adımda, karar verici veya uzmanlardan etki seviyesi için bir eşik değer belirlenmesi istenir ve toplam ilişki matrisinde bu eşik değerinden daha büyük olan değerler seçilir. Böylece, dikey ekseni D-R ve yatay ekseni D+R değerlerinden oluşan Etki-Yönlü Graf Diyagramı elde edilir.

Adım 6: Kriterlerin Ağırlıklarının Belirlenmesi

D+R ve D-R değerleri yardımıyla eşitlik (7) kullanılarak, her bir kriterin ağırlığı bulunur.

$$w_i = \frac{\sqrt{(D+R)^2+(D-R)^2}}{\sum_{i=1}^{n}\sqrt{(D+R)^2+(D-R)^2}} \quad , \quad W = \{w_i\}_{1xn} \tag{7}$$

BULGULAR

Çalışma kapsamında yapılan literatür araştırmaları sonucunda, online alışveriş sitelerinin tercihinde etkili olan kriterler; ürün bilgisi ve çeşitliliği (C_1), zamanında doğru teslimat (C_2), web sitesi tasarımı ve performansı (C_3), güvenilirlik/gizlilik (C_4), ve müşteri memnuniyeti (C_5) olarak belirlenmiştir. Belirlenen bu kriterlerin, birbirleri arasındaki ilişkiler ve önem dereceleri 2 uzman görüşü dikkate alınarak DEMATEL yöntemi ile hesaplanmıştır.

İkili karşılaştırma skalasından faydalanılarak uzman görüşlerinin geometrik ortalaması alınmış ve Tablo 2'deki direkt ilişki matrisi elde edilmiştir.

Tablo 2. Direkt İlişki Matrisi

	C_1	C_2	C_3	C_4	C_5
C_1	0,000	3,464	2,449	2,000	4,000
C_2	2,000	0,000	3,000	3,000	4,000
C_3	3,464	2,449	0,000	4,000	2,449
C_4	1,414	2,449	4,000	0,000	4,000
C_5	1,414	1,732	2,449	2,449	0,000

Direkt-ilişki matrisinin elde edilmesinden sonra, Normalleştirilmiş Direkt-İlişki Matrisi ve Toplam İlişki Matrisi sırasıyla (1), (2) ve (3) eşitlikleri kullanılarak elde edilmiştir. Toplam ilişki matrisinin oluşturulmasından sonra (4), (5) ve (6) eşitlikleri kullanılarak D+R ve D-R değerleri tespit edilmiştir. Tablo 3'de D+R, D-R değerleri ve Toplam İlişki Matrisi gösterilmiştir.

Tablo 3. D+R, D-R Değerleri ile Toplam-İlişki Matrisi

	C_1	C_2	C_3	C_4	C_5	$D+R$	$D-R$
C_1	0,429	0,693	0,733	0,698	0,905	6,024	0,891
C_2	0,555	0,500	0,768	0,755	0,908	6,468	0,503
C_3	0,651	0,678	0,629	0,830	0,874	7,181	0,140
C_4	0,526	0,640	0,813	0,583	0,899	6,895	0,028
C_5	0,406	0,471	0,578	0,568	0,498	6,604	-1,563

Elde edilen sonuçlara baktığımız zaman kriterler arası ilişkiyi gösteren D+R değerlerinde sırasıyla 3., 4. ve 5. kriterlerin diğer kriterler ile daha fazla ilişkide olduğu görülmüştür. Etkilenen veya alıcı olarak adlandırılan, daha

düşük önceliğe sahip ve diğer kriterlerden daha çok etkilenen D-R (negatif) değerlerinde ise 5. kriterin diğer kriterlere göre daha fazla etkilendiği tespit edilmiştir.

Etkileyici veya gönderici olarak adlandırılan, daha yüksek etkiye sahip ve daha yüksek önceliğe sahip olan D-R (pozitif) değerlerinde ise sırasıyla 1., 2., 3. ve 4. kriterlerin diğer kriterlere nispeten daha çok etkilediği görülmüştür. Şekil 1'de Tablo 3'de elde edilen D+R ve D-R değerleri kullanılarak, kriterlerin birbirleri arasındaki etkileşimlerini ortaya koyan etki-yönlü graf diyagramı çizilmiştir.
Kriterler arası ilişkinin ortaya konulmasında kullanılacak eşik değeri uzman karar vericiler tarafından 0,7 olarak belirlenmiştir. Eşik değeri toplam ilişki matrisindeki değerlere uygulanmış, gönderici grubu ve alıcı grubu hesaplamaları yapılarak Şekil 2'de gösterilen ilişki bulunmuştur.

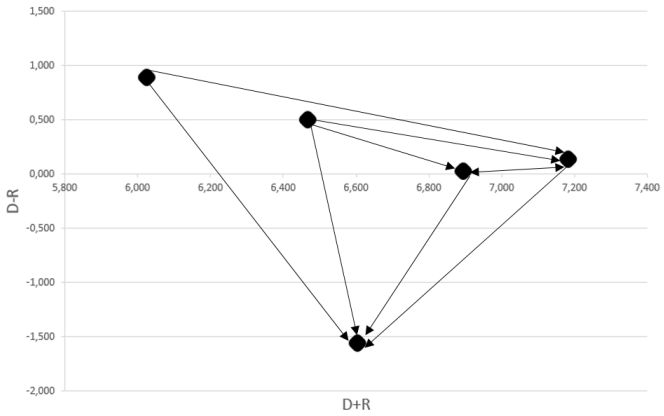

Şekil 1. Etki-Yönlü Graf Diyagramı

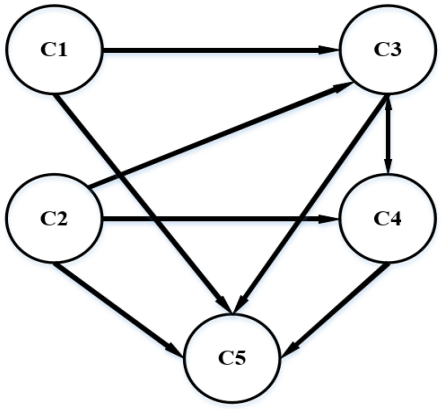

Şekil 2. Kriterlerarası İlişki

Eşitlik (7) kullanılarak hesaplanan kriter ağırlıkları Tablo 4'te gösterilmektedir.

Tablo 4. Kriter Ağırlıkları

KRİTERLER	w_i
Ürün bilgisi ve çeşitliliği	0,182
Zamanında doğru teslimat	0,195
Web sitesi tasarımı ve performansı	0,214
Güvenilirlik/gizlilik	0,205
Müşteri memnuniyeti	0,204

Online alışveriş siteleri için önem derecesi en büyük olan kriter 0,214 değeri ile "web site tasarımı ve performansı" olarak bulunmuştur. Sıralama "güvenilirlik/gizlilik", "müşteri memnuniyeti", "zamanında doğru teslimat" ve "ürün bilgisi ve çeşitliliği" olarak devam etmektedir.

TARTIŞMA ve SONUÇ

Günümüzde, teknoloji ve internetin gelişimine bağlı olarak, online alışveriş yapan tüketicilerin giderek daha da artmasıyla birlikte rekabet de artmıştır. Artan bu rekabetle baş edebilmek için online alışveriş sitelerinin, internet çağının getirmiş olduğu yenilikler dahilinde geliştirilmesi ve iyileştirilmesi gerekmektedir. Online alışveriş siteleri, kar optimizasyonu için, teknoloji ile yaşamayı bilmeli ve Endüstri 4.0 uygulamalarını sistemlerine entegre etmelidirler. Bu bağlamda, online alışveriş siteleri Endüstri 4.0 uygulamaları ile; daha az zaman ve maliyet ile müşteri memnuniyetini arttırabilir, piyasa koşullarına daha kolay adapte olabilir ve uzun vadede pazarlama etkinliklerini arttırabilirler.

Bu çalışmada, online alışveriş siteleri tercih edilirken hangi kriterlerin ne derecede önemli olduğu DEMATEL yöntemi ile tespit edilmiştir. Kriter ağırlıkları sıralaması; web sitesi tasarımı ve performansı, güvenilirlik/gizlilik, müşteri memnuniyeti, zamanında doğru teslimat ve ürün bilgisi ve çeşitliliği şeklinde olmuştur.

Sıralamada en önemli bulunan kriter, web sitesi tasarımı ve performansıdır. Tüketiciler için karmaşık site tasarımı ve site sayfalarının yavaş yüklenmesi oldukça büyük bir sorundur. Alışveriş sitelerinin oldukça sade, yalın ve yüksek performanslı olarak tasarlanması gerekmektedir. Böylece, olabildiğince az işlem adımıyla, tüketicinin istediği ürüne ulaşması sağlanacaktır. Bu bağlamda, online alışveriş siteleri yapay zeka, nesnelerin interneti ve bulut bilişim gibi Endüstri 4.0 uygulamalarıyla uyumlu olarak dizayn edilmelidir. Müşterinin aradığını daha rahat bulabilmesi için yapay zekâ kullanılarak görsel arama motorları siteye eklenebilir. Görüntü işleme algoritmalarına dayanmakta olan bu sistem web site tasarımını geliştirerek müşteri hizmetlerinin iyileştirilmesine yardımcı olabilir.

Güvenilirlik/gizlilik kriteri ikinci sıradadır. İnsanlar online alışveriş yaparken, kişisel bilgilerini ve kredi kartı bilgilerini paylaşma konusunda kendini güvende hissetmemektedirler. Online alışveriş siteleri, bu sorunları engellemek için SSL (Secure Sockets Layer) ve 3D Güvenlik uygulamaları gibi önlemler almaktadır. Ancak tüketicileri tatmin etmek için bu önlemleri sürekli olarak geliştirmeli ve tüketiciyle paylaşmalıdır. Bu bağlamda, işletmeler, siber güvenlik sistemleri ve makine öğrenimi algoritmaları kullanarak, güvenlik tehditleri ve açıklıklarını kolay ve hızlı bir şekilde tespit edebilirler. Böylece, sitelerini güvende tutmak için uygun güvenlik çözüm önerilerine rahatça erişebilirler.

Üçüncü sırada müşteri memnuniyeti kriteri vardır. Müşteriler alışveriş yaparken karşılaşmış olduğu sıkıntı veya şikâyet gibi durumlarda 7/24 alışveriş sitesiyle iletişim kurmak istemektedir. Aldığı ürün veya hizmet için satış sonrası hizmet sağlanması da müşteriler için oldukça önemlidir. Online alışveriş siteleri, müşteri memnuniyetini artırmak için yapay zekâ ve makine öğrenimi teknikleri kullanılarak geliştirilen sohbet ve canlı destek robotları kullanabilir. Bu robotların insan gibi davranma ve öğrenme yeteneği vardır. Böylelikle, müşterilerle daha hızlı bir şekilde iletişime geçilebilir.

Zamanında doğru teslimat kriteri dördüncü sıradadır. Tüketici satın aldığı ürünün eksiksiz, hasarsız bir şekilde ve vaat edilen zaman içinde teslimatını beklemektedir. İşletmeler, Endüstri 4.0 uygulamalarını sitemlerine entegre ederek insani hataları hemen hemen sıfıra indirebilir. Otonom robotlar ve drone teknolojisi kullanılarak ürün teslimat süreçleri kısaltılabilir.

Sıralamada son sıradaki kriter ürün bilgisi ve çeşitliliği olarak bulunmuştur. Tüketici almak istediği ürünün tüm özelliklerini açık bir şekilde site sayfasında görmek istemektedir. Ayrıca ürün çeşitliliği bir avantaj olarak görülse de çoğu zaman müşterinin aklını karıştırmaktadır. Müşterinin alışveriş sitesindeki davranışlarıyla ilgili verilerin analizinde makine öğrenimi algoritmaları kullanılabilir. Bu sayede, müşterinin almak istediği ürün tahmin edilebilir ve en uygun ürünler önerilebilir.

Gelecekte yapılacak olan çalışmalarda, öncelikle kriter sayısının artırılması ile uygulama yapılabilir. Böylece farklı durumların ve yaklaşımların göz önüne alınması ile problemin içeriği gelişecek ve zenginleşecektir. Ayrıca çalışmaya konu olacak kriterlerin bulanık olma durumları dikkate alınarak çalışma farklı bir bakış açısına sahip olacak şekilde geliştirilebilir. Alışveriş sitelerinin seçim sürecinin ele alınacağı bir problem yapısı ile birleştirilerek Çok Ölçütlü Karar Verme Teknikleri kullanılarak çözümleme yapılması da seçenekler arasında olacaktır.

KAYNAKLAR

Agrawal, V., Seth, N., & Dixit, J. K. (2020). A combined AHP–TOPSIS–DEMATEL approach for evaluating success factors of e-service quality: an experience from Indian banking industry. *Electronic Commerce Research*, 1-33. https://doi.org/10.1007/s10660-020-09430-3

Aksakal, E., & Dağdeviren, M. (2010). ANP ve DEMATEL yöntemleri ile personel seçimi problemine bütünleşik bir yaklaşım. *Gazi Üniversitesi Mühendislik Mimarlık Fakültesi Dergisi*, 25(4), 905-913.

Bayır, T. (2020). B2C Online Alışveriş Sitelerinin Seçim Kriterlerinin AHP Yöntemi ile Belirlenmesi. *Kesit Akademi Dergisi*, 6 (25), 641-653.

Çabuk, S., Doğan-Südaş, H., & Bulğurcu B. (2012). Bulanık bir model ile özel alışveriş sitelerinin değerlendirilmesi. *Cag University Journal of Social Sciences*, 9(2), 35-47.

Çakır, E., Akel A., & Doğaner, D. (2018). Türkiye'de faaliyet gösteren özel alışveriş sitelerinin bütünleşik SWARA -WASPAS yöntemi ile değerlendirilmesi. *Uluslararası İktisadi ve İdari İncelemeler Dergisi*, 599-616. https://doi.org/10.18092/ulikidince.347658

Cavlak, E. (2012). Online alışveriş sitesi tercihinde etkili olan kriterlerin belirlenmesine ve önceliklendirilmesine yönelik bir karar modeli. Doktora Tezi, İstanbul Teknik Üniversitesi Fen Bilimleri Enstitüsü Endüstri Mühendisliği Anabilim Dalı, İstanbul 95s.

Cheung, C. M., & Lee, M. K. (2006). Understanding consumer trust in Internet shopping: A multidisciplinary approach. *Journal of the American society for Information Science and Technology*, 57(4), 479-492. https://doi.org/10.1002/asi.20312

Chiu, Y. J., Chen, H. C., Tzeng, G. H., & Shyu, J. Z. (2006). Marketing strategy based on customer behaviour for the LCD-TV. *International journal of management and decision making*, 7(2-3), 143-165. https://doi.org/10.1504/IJMDM.2006.009140

Derse, O. (2022). DEMATEL Tabanlı TOPSIS yöntemi ve küme kapsama modeli ile afet lojistiği için depo yeri seçimi: Ege Bölgesi örneği. *Kahramanmaraş Sütçü İmam Üniversitesi Mühendislik Bilimleri Dergisi*, 25(4), 702-713. https://doi.org/10.17780/ksujes.1159925

Dündar, S., Fatih, E., & Özdemir, Ş. (2007). Fuzzy TOPSIS yöntemi ile sanal mağazaların web sitelerinin değerlendirilmesi. *Atatürk Üniversitesi İktisadi ve İdari Bilimler Dergisi*, 21(1), 287-305.

Gök, A. C., & Perçin, S. (2016). Elektronik alışveriş (e-alışveriş) sitelerinin e-hizmet kalitesi açısından değerlendirilmesinde DEMATEL-AAS-VIKOR yaklaşımı. *Anadolu Üniversitesi Sosyal Bilimler Dergisi*, 16(2), 131-144. https://doi.org/10.18037/ausbd.389223

Hori, S., & Shimizu, Y. (1999). Designing methods of human interface for supervisory control systems. *Control engineering practice*, *7*(11), 1413-1419. https://doi.org/10.1016/S0967-0661(99)00112-4

Hung, Y. H., Chou, S. C. T., & Tzeng, G. H. (2006). Using a fuzzy group decision approach-knowledge management adoption. *APRU DLI 2006 Conference*, 48-52.

Kaur, S., & Gupta, S. K. (2021). A fuzzy-based framework for evaluation of website design quality index. *International Journal on Digital Libraries*, 22, 15-47. https://doi.org/10.1007/s00799-020-00292-6

Li, C. W., & Tzeng, G. H. (2009). Identification of a threshold value for the DEMATEL method using the maximum mean de-entropy algorithm to find critical services provided by a semiconductor intellectual property mall. *Expert Systems with Applications*, 36(6), 9891-9898. https://doi.org/10.1016/j.eswa.2009.01.073

Li, R., & Sun, T. (2020). Assessing factors for designing a successful B2C E-Commerce website using fuzzy AHP and TOPSIS-Grey methodology. *Symmetry*, 12(3), 363. https://doi.org/10.3390/sym12030363

Lu, Y. H., Yeh, C. C., & Liau, T. W. (2022). Exploring the key factors affecting the usage intention for cross-border e-commerce platforms based on DEMATEL and EDAS method. *Electronic Commerce Research*, 1-23. https://doi.org/10.1007/s10660-022-09548-6

Nguyen, P. A. H. (2019, July). Evaluating E-commerce Design Platforms by a Fuzzy VIKOR Approach. *2019 International Conference on System Science and Engineering*, 397-400, IEEE. DOI: 10.1109/ICSSE.2019.8823443

Nilashi, M., Ibrahim, O., Mirabi, V. R., Ebrahimi, L., & Zare, M. (2015). The role of security, design and content factors on customer trust in mobile commerce. *Journal of Retailing and Consumer Services*, 26, 57-69. https://doi.org/10.1016/j.jretconser.2015.05.002

Ömürbek, N., & Şimşek, A. (2014). Analitik hiyerarşi süreci ve analitik ağ süreci yöntemleri ile online alişveriş site seçimi. *Journal of Management and Economics Research*, *12*(22), 306-327. https://doi.org/10.11611/JMER214

Özgüven, N. (2012). PROMETHEE sıralama yöntemi ile özel alışveriş siteleri üzerine bir araştırma. *Selçuk Üniversitesi Sosyal Bilimler Enstitüsü Dergisi*, (27), 195-201.

Petekçi, A. R. (2021). Endüstri 4.0: Fırsat mı tehlike mi?. *Bilgisayar Bilimleri ve Teknolojileri Dergisi*, 2(1), 7-15.

Seyed-Hosseini, S. M., Safaei, N., & Asgharpour, M. J. (2006). Reprioritization of failures in a system failure mode and effects analysis by decision making trial and evaluation laboratory technique. *Reliability engineering & system safety*, 91(8), 872-881. https://doi.org/10.1016/j.ress.2005.09.005

Soner, S., & Önüt, S. (2006). Multi-criteria supplier selection: An ELECTRE-AHP application. *Sigma*, 4, 110-120.

Tsai, P. H., Hsiao, W. H., & Chen, C. J. (2023). Which food delivery platforms are winning the restaurant food delivery wars? Analysis from a consumer perspective. *International Journal of Consumer Studies*, 47(1), 155-176. https://doi.org/10.1111/ijcs.12816

Tsai, W. H., & Chou, W. C. (2009). Selecting management systems for sustainable development in SMEs: A novel hybrid model based on DEMATEL, ANP, and ZOGP. *Expert systems with applications*, 36(2), 1444-1458. https://doi.org/10.1016/j.eswa.2007.11.058

TÜSİAD. Türkiye'nin sanayi 4.0 dönüşümü. (2016). https://tusiad.org/tr/yayinlar/raporlar/item/8671-turkiyenin-sanayi-40-donusumu/ Erişim 02.08.2023.

Tzeng, G. H., Chiang, C. H., & Li, C. W. (2007). Evaluating intertwined effects in e-learning programs: A novel hybrid MCDM model based on factor analysis and DEMATEL. *Expert systems with Applications*, 32(4), 1028-1044. https://doi.org/10.1016/j.eswa.2006.02.004

Wu, W. W., & Lee, Y. T. (2007). Developing global managers' competencies using the fuzzy DEMATEL method. *Expert systems with applications*, 32(2), 499-507. https://doi.org/10.1016/j.eswa.2005.12.005

Yalçın, F. (2012). İnternet pazarlamasında müşteri memnuniyeti: Günün fırsatları üzerine bir uygulama. Yüksek Lisans Tezi. Atılım Üniversitesi, Sosyal Bilimler Enstitüsü, İşletme Ana Bilim Dalı, Ankara 143s.

Zhang, X., Liu, P., & Du, Z. (2008). Research on E-commerce website evaluation with hybrid decision-making index and extension of the TOPSIS method. *2008 Third International Conference on Pervasive Computing and Applications*, 1, 106-109, IEEE. DOI: 10.1109/ICPCA.2008.4783556

KSÜ Mühendislik Bilimleri Dergisi, 26(Özel Sayı), 2023 KSU J Eng Sci, 26(Special Issue), 2023
9th Uluslararası IFS Çağdaş Matematik ve Mühendislik Konferansı Özel Sayısı
9th International IFS Contemporary Mathematics and Engineering Conference Special Issue
Araştırma Makalesi Research Article

Kahramanmaras Sutcu Imam University
Journal of Engineering Sciences

Geliş Tarihi : 09.08.2023 Received Date : 09.08.2023
Kabul Tarihi : 18.09.2023 Accepted Date : 18.09.2023

EFFECTS OF COMPLETE AND PARTIAL CYLINDRICAL FIN CONFIGURATIONS ON THERMOHYDRAULIC PERFORMANCE OF A MINICHANNEL HEAT SINK

TAM VE PARÇALI SİLİNDİRİK KANATÇIK KONFİGÜRASYONLARININ BİR MİNİKANALLI ISI ALICININ TERMOHİDROLİK PERFORMANSI ÜZERİNDEKİ ETKİLERİ

Buğra SARPER[1*] (ORCID: 0000-0001-7554-6575)
Döndü Nur TÜRK[2] (ORCID: 0009-0004-4144-5361)
Kayhan DAĞIDIR[1] (ORCID: 0000-0003-0499-1764)
Orhan AYDIN[3] (ORCID: 0000-0002-2492-8212)

[1] Tarsus University, Mechanical Engineering Department, Mersin, Turkey
[2] Tarsus University, Outomotive Engineering Department, Mersin, Turkey
[3] Karadeniz Technical University, Mechanical Engineering Department, Trabzon, Turkey

*Sorumlu Yazar / Corresponding Author: Buğra SARPER, bugrasarper@tarsus.edu.tr

ABSTRACT

In this numerical investigation, the impacts of complete and partial cylindrical fin configurations on the thermohydraulic performance of a minichannel heatsink are studied. ANSYS Fluent software is used to conduct numerical analyses for four distinct mass flow rates ranging from 0.00265 kg/s to 0.0045 kg/s and three distinct fin positions. The effects of various configurations on velocity and temperature fields, average Nusselt number, Nusselt number ratio, friction coefficient, and performance evaluation coefficient are analyzed. According to the study's findings, using partial cylindrical fins has a substantial impact on both heat transfer and pressure drop. When evaluating heat transfer, MCHS-R2a produces the greatest results, but this configuration greatly raises flow resistance. MCHS-R2c was found to have substantial potential when evaluated in terms of thermohydraulic performance.

Keywords: Minichannel heat sink, partial cylindrical fin, thermohydraulic performance.

ÖZET

Bu çalışmada, tam ve parçalı silindirik kanatçık konfigürasyonlarının bir minikanallı ısı alıcının termohidrolik performansına etkileri sayısal olarak incelenmiştir. Bu amaçla, 0.00265 kg/s ile 0.0045 kg/s aralığında dört farklı debi ve üç farklı kanatçık konumu için sayısal çalışmalar ANSYS Fluent yazılımı kullanılarak gerçekleştirilmiştir. Farklı konfigürasyonların hız ve sıcaklık alanlarına, ortalama Nusselt sayısına, Nusselt sayısı oranına, sürtünme katsayısına ve ısı alıcının performans katsayısına olan etkileri değerlendirilmiştir. Çalışma sonucunda, parçalı silindirik kanatçık kullanımının ısı transferi ve basınç düşümü üzerinde önemli etkilerinin olduğu, ısı transferi açısından değerlendirildiğinde MCHS-R2a'nın en iyi sonucu verdiği fakat bu konfigürasyonun akışa karşı olan direnci önemli ölçüde artırdığı belirlenmiştir. Termohidrolik performans açısından değerlendirildiğinde ise MCHS-R2c'nin önemli sonuçlar vadettiği ortaya konmuştur.

Anahtar Kelimeler: Minikanallı ısı alıcı, parçalı silindirik kanatçık, termohidrolik performans.

ToCite: SARPER, B., TÜRK, D.N., DAĞIDIR, K. & AYDIN, O., (2023). EFFECTS OF COMPLETE AND PARTIAL CYLINDRICAL FIN CONFIGURATIONS ON THERMOHYDRAULIC PERFORMANCE OF A MINICHANNEL HEAT SINK. *Kahramanmaraş Sütçü İmam Üniversitesi Mühendislik Bilimleri Dergisi*, 26 (Özel Sayı), 1156-1170.

INTRODUCTION

Changing manufacturing techniques and advancing technology have enabled the design and production of compact heat exchangers with reduced volume and greater efficiency. Minichannel heat sinks (MCHSs), a type of compact heat exchangers, have attracted the attention of researchers due to their compact structure, effective thermal performance, and growing application possibilities. As a result of advancements in materials technology, MCHSs have been used as a practical apparatus to remove excessive heat from systems since the mid-1990s (Bowers and Mudawar, 1994). Their prevalence has increased due to their widespread application in electronics cooling.

To meet the ever-increasing demand for cooling, MCHSs have modified to incorporate fins, which contribute to the enhancement of heat transfer characteristics (Naphon and Wongwises, 2010). However, while fins positioned in the flow field increase heat transfer, they negatively affect the pressure drop. This has led to the necessity of addressing the issue in terms of both heat transfer and pressure drop. Researchers have investigated a variety of configurations in channel structure and flow pattern so as to enhance the system's efficiency in terms of both heat transfer and pressure drop. Table 1 provides a summary of various configurations of channel structures and flow patterns reported in the literature.

Table 1. Some Studies on Channel Structures and Flow Patterns in The Literature

Reference	Content of the study
Bi et al. (2013)	The channel with narrow dimples, cylindrical grooves and fins smaller than the channel height.
Wang et al. (2013)	The rectangular straight and expanding cross section of the channel.
Di Maio et al. (2014)	The straight and ribbed channel.
Ghobadi and Muzychka (2014)	The channel with 90° curved and spiral geometry.
Li et al. (2015)	The channel with smooth and grooved surfaces.
Xu et al. (2016)	The channel with three and five ports.
Saeed and Kim. (2016)	The channel with variable fin spacing, thickness and height.
Ma et al. (2016)	The channel with corrugated fins.
Liu and Yu (2016)	The channel with obstacles in the flow direction.
Kim et al. (2017)	The channel with variable widht and length.
Tang (2017)	The channel with layered structure.
Saeed and Kim (2017)	The channel with different configurations of distributors and collectors at the inlet and outlet.
Imran et al. (2018)	The channel with variable inlets and outlets.
Kumar and Singh (2019)	The channel with variable distributor and collector positions.
Abdulhaleem et al. (2019)	The channel with straight and wavy cross sections.
Lim and Lee (2019)	The channel with parallel and opposing flow directions.
Song et al. (2019)	Flow-regulating distributor and collector with trapezoidal and rectangular fins.
Tikadar et al. (2019);	The channel with parallel and opposing flow directions.
Mitra and Ghosh (2020)	The channel with variable fin thickness, number and channel depth.
Xiao et al. (2020)	The channel with rough surface.
Dabrowski (2020)	The channel with rectangular, trapezoidal, triangular or concave configurations.
Cao et al. (2020)	The channel with curved structure with variable inlets and outlets.
Deng et al. (2020)	The channel with horizontal and vertical slots.
Kilic et al. (2020)	The channel with circular fins.
Tikadar (2020);	The channel with transition zones.
Azadi et al. (2020)	The channel containing fins with trapezoidal, square, triangular and sine profiles.

It is clear that the various types of channel structures and flow patterns presented in the literature have an impact on the performance of MCHSs. However, selection of the most effective configuration among many potential configurations is a unique area. Recent studies have examined the effects of both fin and channel forms on heat transfer and pressure drop for optimal heat sink design. Al-Hasani and Freegah (2022) numerically investigated the use of dual outlets and secondary flow lines at various angles to improve the efficiency of a water-cooled MCHS. They reported that combining the secondary flow with pin fins improved thermal and hydraulic performance, and achieved that a performance improvement of up to 47%. Mahmood and Freegah (2022) numerically examined the effect of counterflow formation and dimpled ribs on thermohydraulic performance of a serpentine MCHS. The results

of the study showed that the overall performance of MCHS was significantly improved. Bessanane et al. (2022) numerically investigated the effects of the use of rectangular mini-channels and diamond-shaped fin arrangements in a split pattern on flow and heat transfer in a MCHS. Chen et al. (2022) numerically studied the effects of triangular prisms on thermal and hydraulic performances of a MCHS. The results of the study showed that the highest Nusselt number and coefficient of friction were reached in the MCHS with a backward triangular prism. Khadir (2023) numerically investigated the performance of a finned MCHS with elliptical, circular and V-shaped cross-sections in terms of velocity distribution uniformity and heat sink surface temperature reduction. As a result of the study, it was reported that the lowest flow disturbance and surface temperature were obtained for the channel with elliptical fins. Zhang et al. (2023) numerically investigated the thermohydraulic performance of a MCHS, which contains various mini channel structures with different fin and cavity forms. The results showed that the addition of fins to the mini channel increased heat transfer and flow resistance. In addition, it was stated that the combined use of fin and cavity structures provided 60% improvement in terms of thermohydraulic performance. Accordingly, it is considered that studies on an optimum finned MCHS design in terms of heat transfer and pressure drop will contribute to the literature. The aim of this study is to numerically examine the effects of the use of complete and partial cylindrical fins on thermohydraulic performance of a MCHS. Thus, numerical studies are carried out for the mini channel heat sink designs including reference case (MCHS), complete cylindrical fins (MCHS-R) and partial cylindrical fins (MCHS-R2) under same operating conditions.

NUMERICAL STUDY

Problem Geometry

A schematic illustration of the MCHS containing seven minichannels is shown in Fig. 1. The length (L), width (W), and height (H) of MCHS are 75, 50, and 5 mm, respectively. The minichannels' widths (w_{ch}) and heights (h_{ch}) are 4.2 mm and 2 mm, respectively, and the walls separating them have the thickness (t_w) of 1.77 mm. The distance between the centers of the first and last fins and the channel inlets-outlets is 10 mm. The diameter of each fin is 2 mm, and the distance between each fin (s) is 13.75 mm.

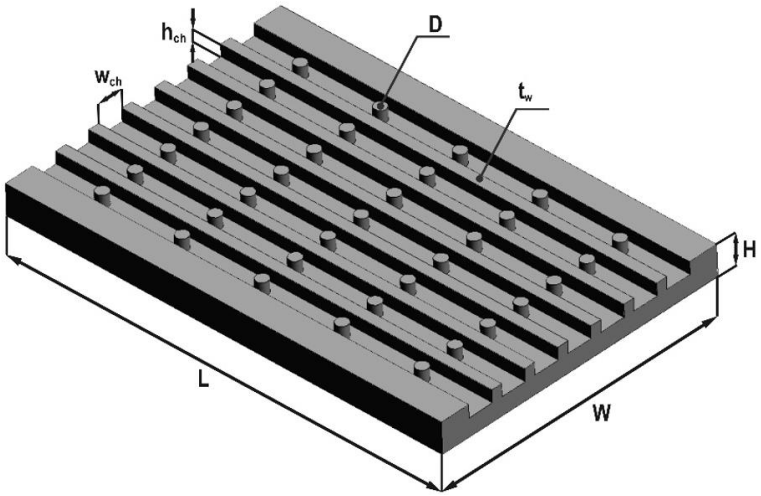

Figure 1. Schematic Illustration of The Minichannel Heat Sink with Complete Cylindrical Fins (MCHS-R)

The study covers five different cases, including the reference case (MCHS). In the reference case, no fin is utilized in the minichannels. In addition, the details of configurations designated MCHS-R, MCHS-R2a, MCHS-R2b, and MCHS-R2c are shown in Fig 2. These different MCHS configurations are analyzed for various flow rates. In MCHS-R2a, the partial fins are concentrically arranged, whereas in MCHS-R2b and MCHS-R2c, the distance between the center of the partial fins is 3.44 mm and 6.88 mm, respectively.

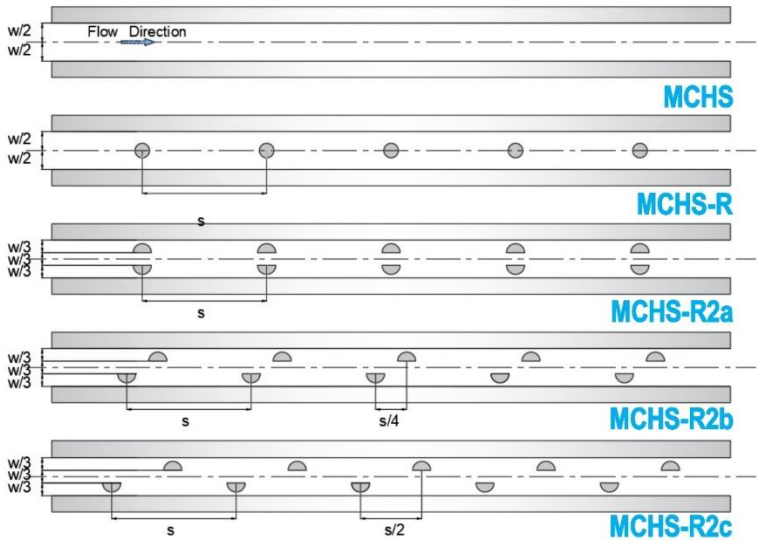

Figure 2. Schematic Illustration of The Studied Cases

Numerical Method and Boundary Conditions

The simulations are conducted using ANSYS Fluent, a finite volume solver. The thermophysical properties of the fluid (water) and heat sink are considered to be constant throughout the numerical solutions, while the flow is at laminar and steady-state conditions. In the numerical solutions, the discretization of the governing equations are performed by the second order upwind scheme, while the SIMPLE algorithm is preferred for the coupling of velocity and pressure (Ansys Inc., 2021).

The governing equations under these assumptions are as follows (Imran et al., 2018):

Continuity equation:

$$\frac{\partial u}{\partial x}+\frac{\partial v}{\partial y}+\frac{\partial w}{\partial z}=0 \tag{1}$$

x-momentum equation:

$$u\frac{\partial u}{\partial x}+v\frac{\partial u}{\partial y}+w\frac{\partial u}{\partial z}=-\frac{1}{\rho}\frac{\partial p}{\partial x}+\vartheta\left(\frac{\partial^2 u}{\partial x^2}+\frac{\partial^2 u}{\partial y^2}+\frac{\partial^2 u}{\partial z^2}\right) \tag{2}$$

y-momentum equation:

$$u\frac{\partial v}{\partial x}+v\frac{\partial v}{\partial y}+w\frac{\partial v}{\partial z}=-\frac{1}{\rho}\frac{\partial p}{\partial y}+\vartheta\left(\frac{\partial^2 v}{\partial x^2}+\frac{\partial^2 v}{\partial y^2}+\frac{\partial^2 v}{\partial z^2}\right) \tag{3}$$

z-momentum equation:

$$u\frac{\partial w}{\partial x}+v\frac{\partial w}{\partial y}+w\frac{\partial w}{\partial z}=-\frac{1}{\rho}\frac{\partial p}{\partial z}+\vartheta\left(\frac{\partial^2 w}{\partial x^2}+\frac{\partial^2 w}{\partial y^2}+\frac{\partial^2 w}{\partial z^2}\right) \tag{4}$$

Energy equation in flow domain:

$$u\frac{\partial T_f}{\partial x}+v\frac{\partial T_f}{\partial y}+w\frac{\partial T_f}{\partial z}=\alpha\left(\frac{\partial^2 T_f}{\partial x^2}+\frac{\partial^2 T_f}{\partial y^2}+\frac{\partial^2 T_f}{\partial z^2}\right) \tag{5}$$

Energy equation in solid domain:

$$\frac{\partial^2 T_s}{\partial x^2} + \frac{\partial^2 T_s}{\partial y^2} + \frac{\partial^2 T_s}{\partial z^2} = 0 \quad (6)$$

Here, u, v, and w represent the velocity components in the x, y, and z directions, while T_f and T_s represent the temperature of the fluid and solid. ρ represents the density of the fluid, while ϑ and α denote its kinematic viscosity and thermal diffusivity.

The velocity inlet boundary condition is employed at the minichannel inlets, and the water temperature is 298 K. The pressure outlet boundary condition is employed at the minichannel outlets. The base of the MCHS is heated with a constant heat flux of 20000 W/m^2, while minichannel and fin surfaces in contact with water have coupled boundary condition and hydrodynamically no-slip boundary condition. The heat sink's top and side faces are perfectly insulated. The boundary conditions are given in Fig. 3.

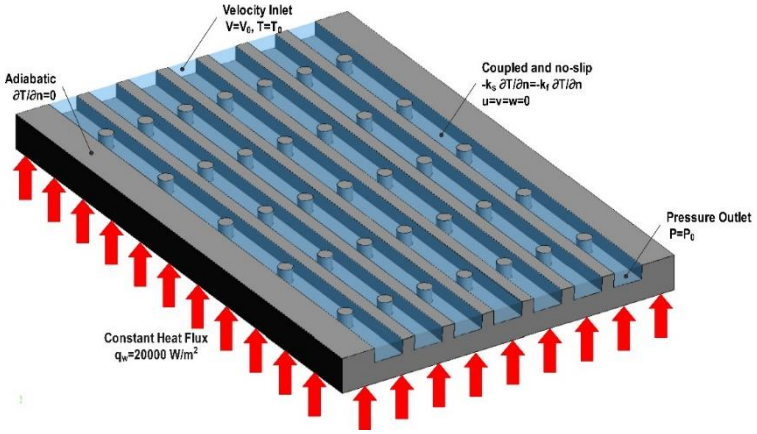

Figure 3. Boundary Conditions Utilized in Numerical Simulations

Data Analysis

As the effects of the above-described configurations on flow and heat transfer characteristics at varying flow rates are evaluated, the following performance parameters are calculated within the scope of the study.

The heat gained by the cooling fluid is calculated as follows (Al-Hasani and Freegah, 2022):

$$\dot{Q} = \dot{m}_f c_{p,f} \Delta T_f = \bar{h} A_c (T_{base,ave} - T_f) \quad (7)$$

where $\dot{m}_f$, $c_{p,f}$, and ΔT_f denote the mass flow rate, specific heat, and temperature rise of water, respectively. A_c denote the effective surface area, while $T_{base,ave}$ and T_f denote the average surface temperature of the base and film temperature, respectively.

The film temperature is calculated as follows:

$$T_f = \frac{T_{f,in} + T_{f,out}}{2} \quad (8)$$

where $T_{f,in}$ and $T_{f,out}$ denote the inlet and outlet temperatures of the water, respectively.

The average heat transfer coefficient is calculated as follows (Imran et al., 2018):

$$\bar{h} = \frac{\dot{m}_f c_{p,f} \Delta T_f}{A_c (T_{base,ave} - T_f)} \quad (9)$$

The average Nusselt number is calculated as follows:

$$Nu_{ave} = \frac{\bar{h}.D_h}{k_f} \tag{10}$$

where k_f is the thermal conductivity of water.

The Nusselt number ratio is calculated as follows:

$$Nu_r = \frac{Nu_{ave,i}}{Nu_{ave,ref}} \tag{11}$$

The hydraulic diameter of the minichannels is calculated as follows:

$$D_h = \frac{2 \times w_{ch} \times h_{ch}}{w_{ch} + h_{ch}} \tag{12}$$

The total pressure drop between the inlet and outlet of the heat sink is calculated as follows:

$$\Delta P = P_{in} - P_{out} \tag{13}$$

The friction coefficient is calculated as follows:

$$f = \frac{2\Delta P D_h}{L\rho_f u_{in}^2} \tag{14}$$

The performance evaluation coefficient, which represents the thermohydraulic performance of the heat sink, is calculated as follows (Zhang et al., 2023):

$$PEC = \frac{Nu_{ort,i}/Nu_{ort,ref}}{(f_i/f_{ref})^{1/3}} \tag{15}$$

where $Nu_{ort,i}$ and $Nu_{ort,ref}$ denote the average Nusselt number for any configuration and reference case, respectively. f_i and f_{ref} denote the friction coefficient for any configuration and reference case, respectively.

Grid Structure

A polyhedral grid design is employed for this research. A grid independence study is conducted for five distinct cell numbers, and the values of average Nusselt numbers and friction coefficients are compared for each grid design to identify the grid design to be employed in the final simulations. When average Nusselt number and friction coefficient are examined simultaneously, as shown in Fig. 4, it is determined that the grid design with 3914104 cells is sufficient for the final simulations.

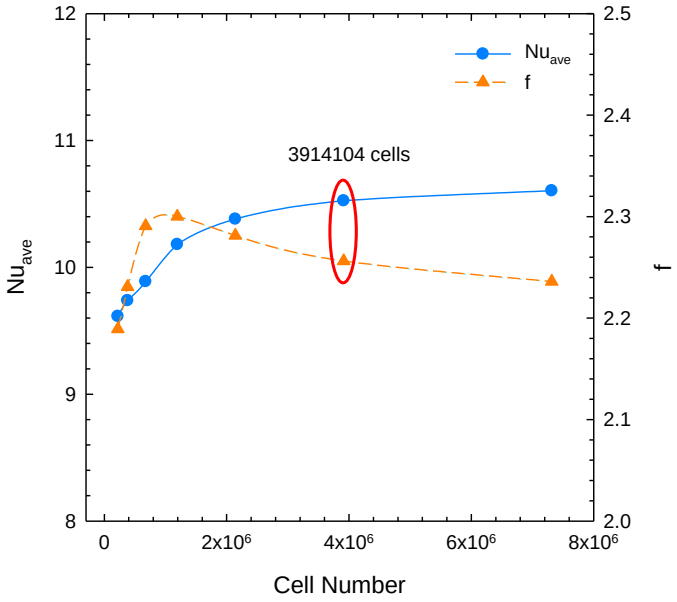

Figure 4. Results of The Grid Independence Study

Validation of the Study

The numerical results of this study are compared to data shared by Al-Hasani and Freegah (2022) for the validation of numerical solution model used in this study. The average Nusselt number and pressure drop characteristics of the MCHS are used for the validation. The relevant data are obtained for different mass flow rates. Accordingly, it is determined that the results of this study is consistent with the data of Al-Hasani and Freegah (2022). Results of the validation study is shown in Fig. 5.

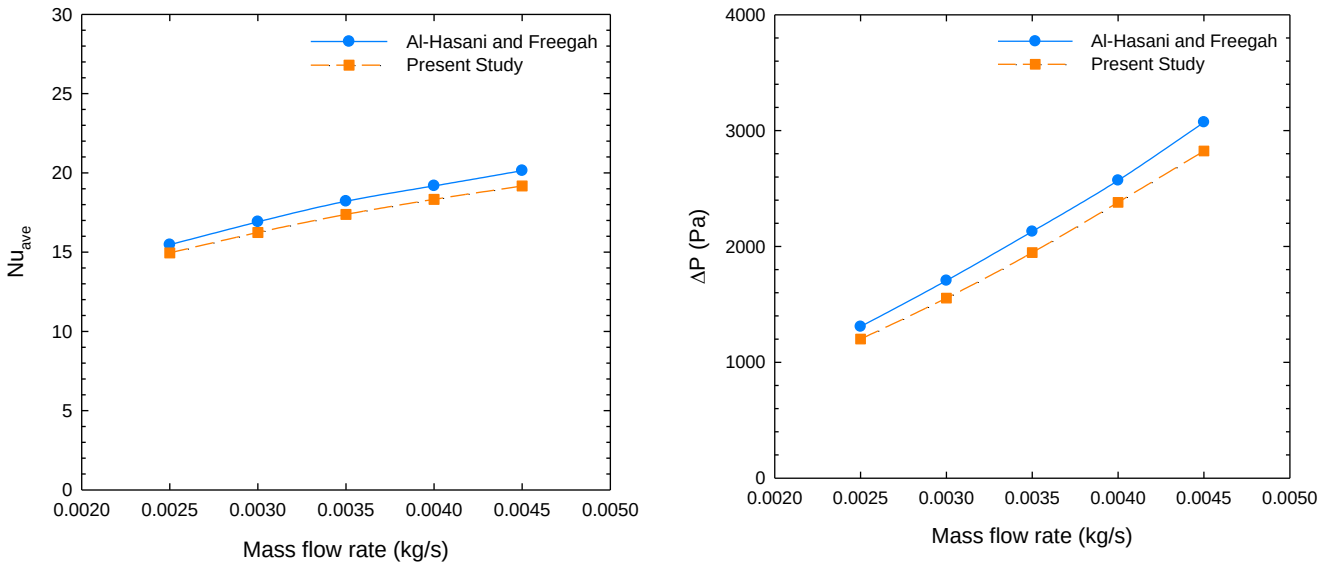

Figure 5. Validation of The Present Study against The Study of Al-Hasani and Freegah (2022)

RESULTS AND DISCUSSION

The impacts of various fin designs on the thermohydraulic performance of a MCHS are numerically studied in this work. The effects of partial and complete cylindrical fins at various flow rates on the flow and heat transfer characteristics of the MCHS are investigated for this purpose. The key performance metrics of the heat sink, such as average Nusselt number, Nusselt number ratio, friction coefficient, and performance evaluation coefficient, are examined in addition to the velocity and temperature fields.

Figures 6 and 7 depict the velocity and temperature fields at the center of the minichannels (at y=4 mm) for various configurations at $\dot{m}_f$=0.002625 kg/s and 0.0045 kg/s, respectively. The flow in MCHS is parallel to the channel walls, as evidenced by the contour plots for both flow rates. In MCHS-R, high velocities occur due to the narrowing of the cross-section in the regions where the fins are placed, while reverse flow occurs downstream of the fins. In MCHS-R2a, the high velocity fluid flows through the partial fins. In MCHS-R2b and MCHS-R2c, the mixing within the flow domain is higher, while local velocities are lower behind the fins and along the channel walls. When the temperature contours are analyzed, the thermal boundary layer thickens towards the exit due to the decreased cooling capacity of the fluid, convective heat transfer diminishes, and the local temperatures of the heat sink increase in MCHS. The addition of fins, on the other hand, increases the heat transfer surface area, allowing the water to remove more heat from the heat sink. The partial fin form also allows for more heat transfer surface area. As a result, the fin temperatures rise towards the outlet, and in all configurations, the temperatures of the fins and fluid are relatively close towards the outlet.

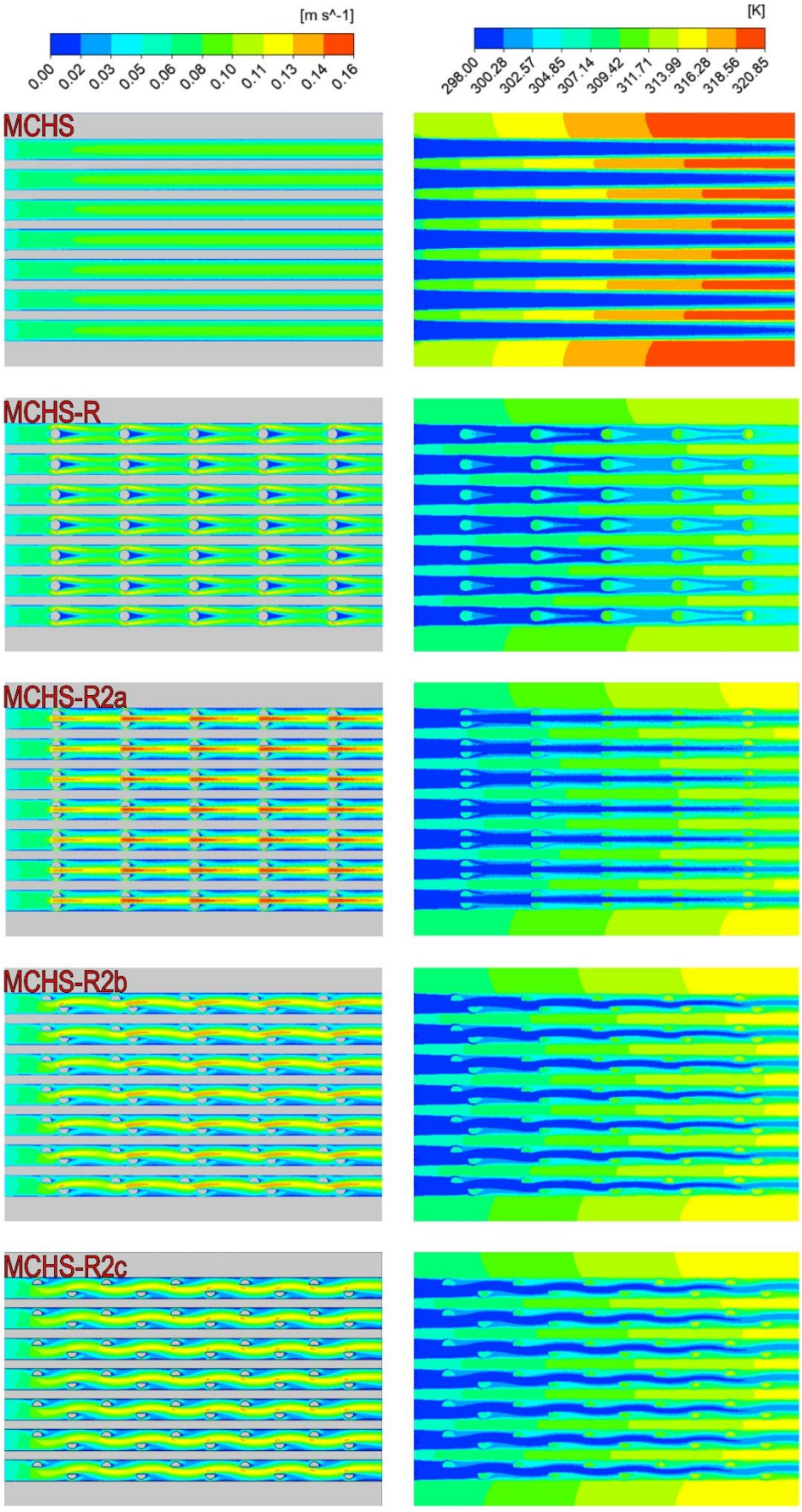

Figure 6. Velocity and Temperature Fields at $\dot{m}_f$=0.002625 kg/s

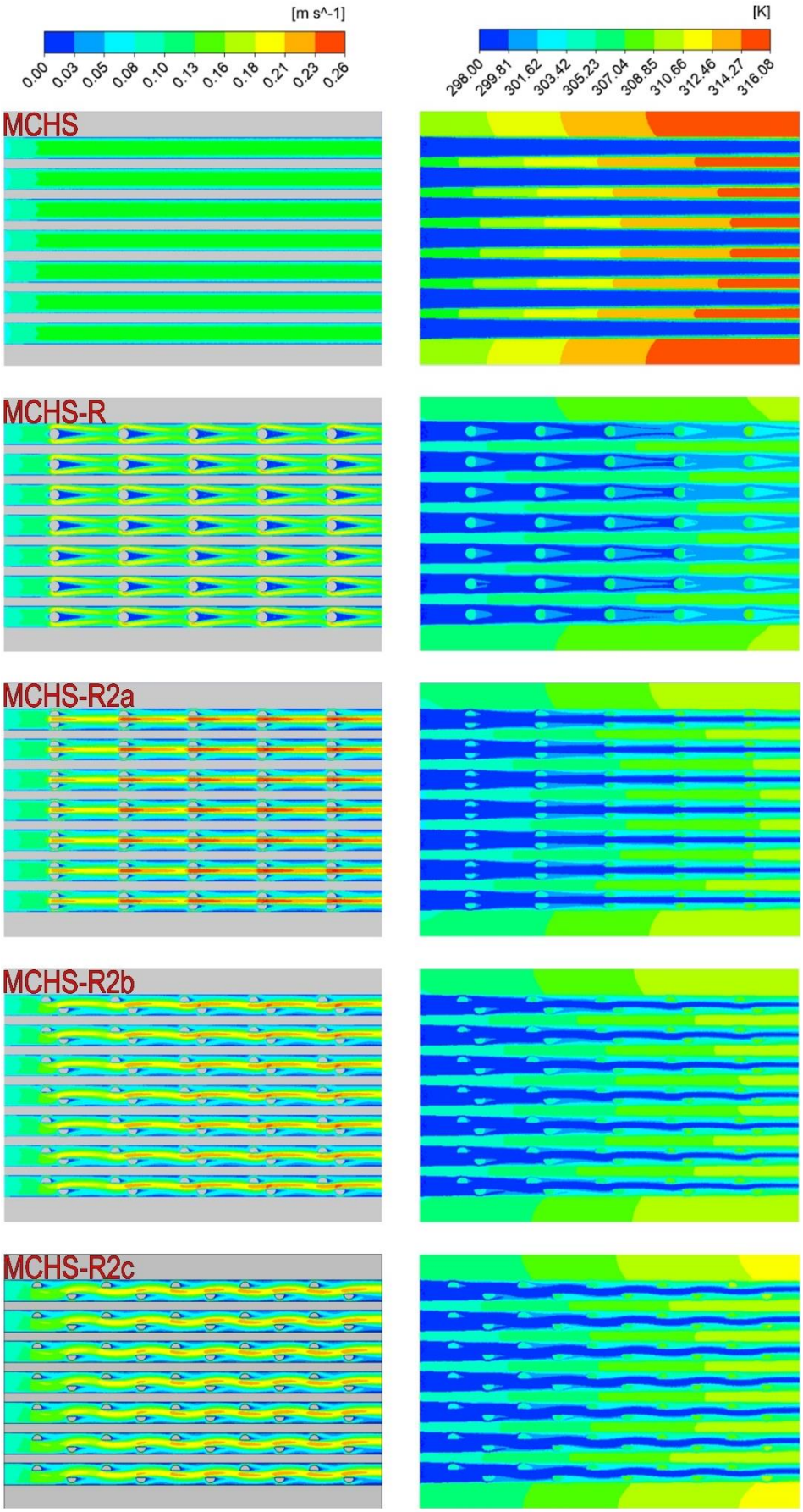

Figure 7. Velocity and Temperature Fields at $\dot{m}_f$=0.0045 kg/s

Figures 8 and 9 depict the Nu_{ave} and Nu_r variations with mass flow rate for the reference case and various fin configurations. Convective heat transfer is the weakest in the reference case, as predicted. In terms of convective heat transfer, however, MCHS-R2a is seen to be the best configuration. At all flow rates, the convective heat transfer rates for MCHS-R2b and MCHS-R2c are quite close to each other. However, the Nu_{ave} for MCHS-R2c is lower than that of the MCHS-R2a. The variation of Nu_r, as shown in Fig. 9, also confirms the preceding conclusions. At all flow rates, the increase in Nu_r is maximum for MCHS-R2a. Nu_r values are close for MCHS-R2b and MCHS-R2c and the increase in MCHS-R2c becomes more apparent as the flow rate increases. Furhermore, MCHS-R is regarded the worst scenario in terms of Nu_r increase and is nearly unaffected by the change in mass flow rate.

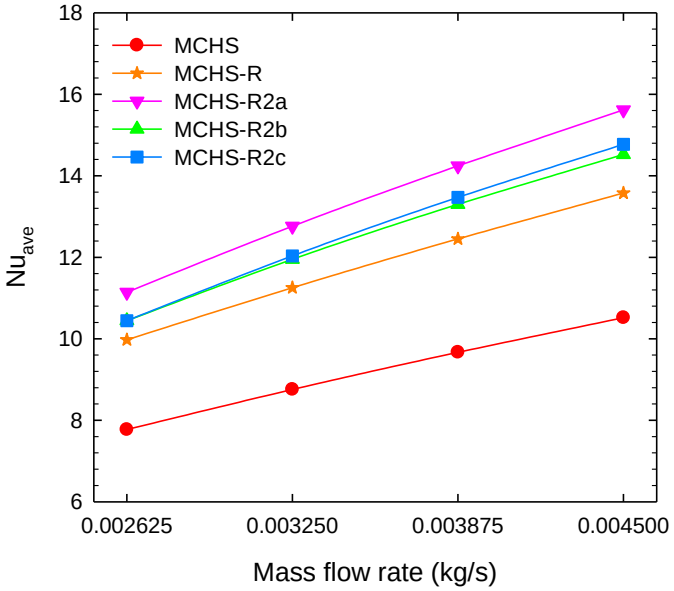

Figure 8. Average Nusselt Number Variation Versus Mass Flow Rate for Different Configurations

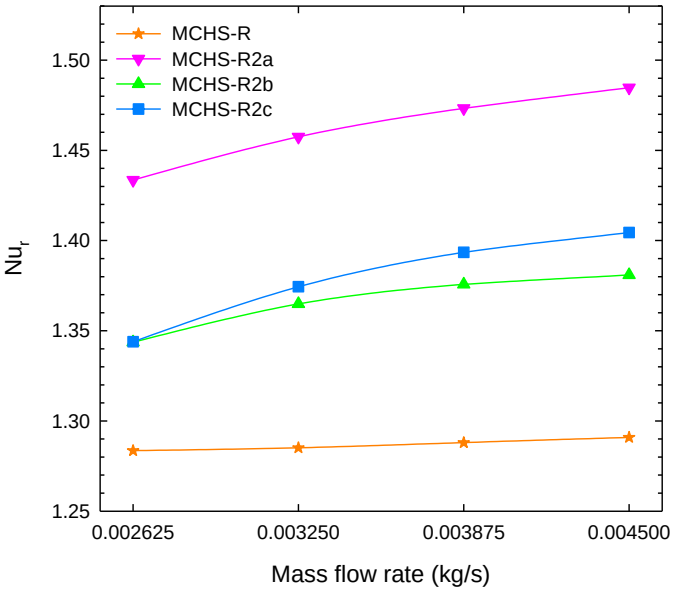

Figure 9. Nusselt Number Ratio Variation Versus Mass Flow Rate for Different Configurations

Figure 10 depicts the relationship between the f and mass flow rate for various fin configurations and the reference case. As anticipated, the f for the reference case (MCHS) is quite low, whereas the utilization of fins considerably increases the f. MCHS-R2a has the greatest flow resistance. MCHS-R2b and MCHS-R2c, whose fins are staggered, have a lower f than that of MCHS-R and MCHS-R2a at all flow rates. When fin configurations are evaluated, increasing the distance between the partial fins substantially decreases the f, and MCHS-R2c has the lowest f values. On the other hand, Fig. 11 illustrates the effects of various fin configurations on the PEC. Analyzing the variation of

PEC with mass flow rate reveals that the thermohydraulic performance of MCHS-R is unfavorable at low mass flow rates, but slightly exceeds 1 as the flow rate increases. MCHS-R2a provides the highest f. Although MCHS-R2c does not provide the greatest convective heat transfer rate, its thermohydraulic performance is significantly higher than the other configurations due to its reduced flow resistance.

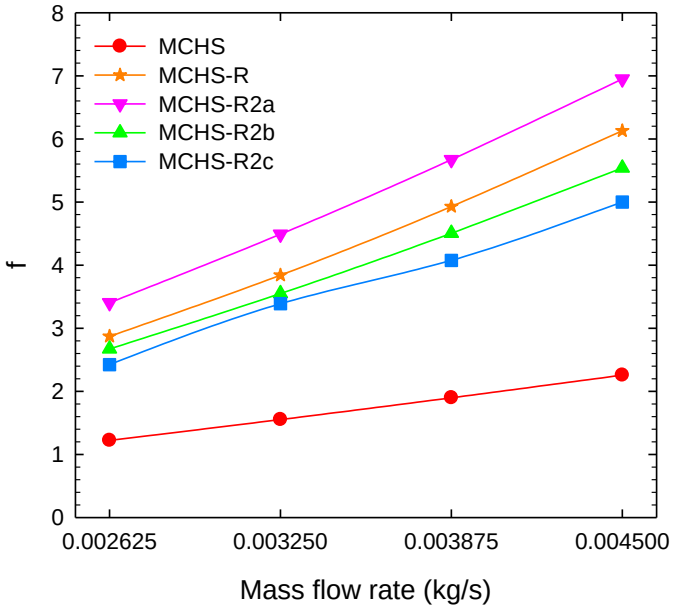

Figure 10. Friction Coefficient Variation Versus Mass Flow Rate for Different Configurations

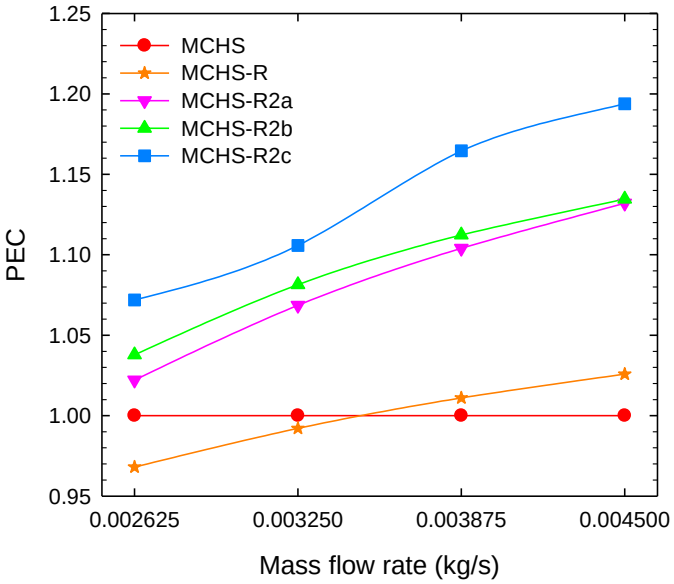

Figure 11. Performance Evaluation Coefficient Variation Versus Mass Flow Rate for Different Configurations

CONCLUSIONS

In this study, the effects of using complete and partial cylindrical fins on thermohydraulic performance of a MCHS are numerically investigated. Additionally, three different partial circular fin forms are proposed as an alternative to the use of traditional cylindrical fins. As a result, the detected findings are as follows:

- It is ensured that the water removes more heat from the heat sink as the heat transfer surface area increases owing to the use of fins. At the same time, the partial fin form further increases the heat transfer surface area.
- It is obtained that the best design in terms of convective heat transfer is the MCHS-R2a configuration. Additionally, MCHS-R2a has the greatest flow resistance.
- It is seen that the use of eccentric partial fins significantly reduces the flow resistance.

- It is observed that the MCHS-R2c configuration provides the best result in terms of thermohydraulic performance. Compared to MCHS, PEC is increased up to 19.4% in MCHS-R2c.

REFERENCES

Abdulhaleem, A. A., Jaffal, H. M., & Khudhur, D. S. (2019). Performance optimiation of a cylindrical mini-channel heat sink using hybrid straight-wavy channel. *International Journal of Thermal Sciences*, *146*, 106111. https://doi.org/10.1016/j.ijthermalsci.2019.106111

Al-Hasani, H. M., & Freegah, B. (2022). Influence of secondary flow angle and pin fin on hydro-thermal evaluation of double outlet serpentine mini-channel heat sink. *Results in Engineering*, *16*, 100670. https://doi.org/10.1016/j.rineng.2022.100670

Ansys Inc. (2021). ANSYS Fluent, Release 21 R2, Theory Guide.

Azadi, M., Hosseinirad, E., Hormozi, F., & Rashidi, S. (2020). Second law analysis for nanofluid flow in mini-channel heat sink with finned surface: a study on fin geometries. *Journal of Thermal Analysis and Calorimetry*, *140*(4), 1883-1895. https://doi.org/10.1007/s10973-019-08921-2

Bessanane, N., Si-Ameur, M., & Rebay, M. (2022). Numerical Study of the Temperature Effects on Heat Transfer Coefficient in Mini-Channel Pin-Fin Heat Sink. *International Journal of Heat and Technology*, *40*(1), 247-257. https://doi.org/10.18280/ijht.400129

Bi, C., Tang, G. H., & Tao, W. Q. (2013). Heat transfer enhancement in mini-channel heat sinks with dimples and cylindrical grooves. *Applied Thermal Engineering*, *55*(1-2), 121-132. https://doi.org/10.1016/j.applthermaleng.2013.03.007

Bowers, M. B., & Mudawar, I. (1994). High flux boiling in low flow rate, low pressure drop mini-channel and micro-channel heat sinks. *International Journal of Heat and Mass Transfer*, *37*(2), 321-332. https://doi.org/10.1016/0017-9310(94)90103-1

Cao, X., Liu, H., Shao, X., Shen, H., & Xie, G. (2020). Thermal performance of double serpentine minichannel heat sinks: Effects of inlet-outlet arrangements and through-holes. *International Journal of Heat and Mass Transfer*, *153*, 119575. https://doi.org/10.1016/j.ijheatmasstransfer.2020.119575

Chen, Z., Feng, Z. F., Zhang, Q. Y., Zhang, J. X. & Guo, F. W. (2022). Effects of regular triangular prisms on thermal and hydraulic characteristics in a minichannel heat sink, *Internatıonal Journal of Heat And Mass Transfer*, *188*. https://doi.org/10.1016/j.ijheatmasstransfer.2022.122583.

Dabrowski, P. (2020). Thermohydraulic maldistribution reduction in mini heat exchangers, *Applıed Thermal Engıneerıng*, *173*. https://doi.org/10.1016/j.applthermaleng.2020.115271.

Deng, Z. Y., Shen, J., Dai, W., Liu, Y., Song, Q., Gong, W., Li, K., & Gong, M. (2020). Flow and thermal analysis of hybrid mini-channel and slot jet array heat sink. *Applied Thermal Engineering*, *171*, 115063. https://doi.org/10.1016/j.applthermaleng.2020.115063

Di Maio, E., Mastrullo, R., Mauro, A. W., & Toto, D. (2014). Thermal management of a multiple mini-channel heat sink by the integration of a thermal responsive shape memory material. *Applied Thermal Engineering*, *62*(1), 113-122. https://doi.org/10.1016/j.applthermaleng.2013.08.039

Ghobadi, M., & Muzychka, Y. S. (2014). Heat transfer and pressure drop in mini channel heat sinks. *Heat Transfer Engineering*, *36*(10), 902-911. https://doi.org/10.1080/01457632.2015.965097

Imran, A. A., Mahmoud, N. S., & Jaffal, H. M. (2018). Numerical and experimental investigation of heat transfer in liquid cooling serpentine mini-channel heat sink with different new configuration models. *Thermal Science and Engineering Progress*, *6*, 128-139. https://doi.org/10.1016/j.tsep.2018.03.011

Khdair, A. I. (2023). Numerical simulation of heat transfer of two-phase flow in mini-channel heat sink and investigation the effect of pin-fin shape on flow maldistribution. *Engineering Analysis with Boundary Elements*, *150*, 385-393. https://doi.org/10.1016/j.enganabound.2023.02.017

Kilic, M., Aktas, M., Sevilgen, G., (2020). Thermal assessment of laminar flow liquid cooling blocks for led circuit boards used in automotive headlight assemblies. *Energies*, *13*(5), 1202-1202. https://doi.org/10.3390/en13051202

Kim, Y., Kim, M., Ahn, C., Kim, H. U., Kang, S. W., & Kim, T. (2017). Numerical study on heat transfer and pressure drop in laminar-flow multistage mini-channel heat sink. *International Journal of Heat and Mass Transfer*, *108*, 1197-1206. https://doi.org/10.1016/j.ijheatmasstransfer.2016.12.025

Kumar, S., & Singh, P. K. (2019). Effects of flow inlet angle on flow maldistribution and thermal performance of water cooled mini-channel heat sink. *International Journal of Thermal Sciences*, *138*, 504-511. https://doi.org/10.1016/j.ijthermalsci.2019.01.014

Li, R. R., Zhang, Y. H., Wang, Y. F., & Wang, L. B. (2015). Convective heat-transfer characteristics of a channel with one surface having mini-grooves in the flow direction and a plain surface located at a mini-distance. *IEEE Transactions on Components, Packaging and Manufacturing Technology*, *5*(1), 65-74. https://doi.org/10.1109/tcpmt.2014.2373054

Lim, K., & Lee, J. (2019). 1-D two-phase flow analysis for interlocking double layer counter flow mini channel heat sink. *International Journal of Heat and Mass Transfer*, *135*, 305-317. https://doi.org/10.1016/j.ijheatmasstransfer.2019.01.092

Liu, X. Q., & Yu, J. (2016). Numerical study on performances of mini-channel heat sinks with non-uniform inlets. *Applied Thermal Engineering*, *93*, 856-864. https://doi.org/10.1016/j.applthermaleng.2015.09.032

Ma, L., Zhao, X., Sun, H., Wu, Q., & Liu, W. (2016). Experimental study of single phase flow in a closed-loop cooling system with ıntegrated mini-channel heat sink. *Entropy*, *18*(6), 128. https://doi.org/10.3390/e18060128

Mahmood, H., & Freegah, B. (2022). Investigating the effect of counter flow formation, ribs and dimples on the hydrothermal performance of the serpentine Mini-Channel Heat Sink (SMCHS). *International Communications in Heat and Mass Transfer*, *139*, 106490. https://doi.org/10.1016/j.icheatmasstransfer.2022.106490

Mitra, I., & Ghosh, I. (2020). Mini-channel heat sink parameter sensitivity based on precise heat flux re-distribution. *Thermal Science and Engineering Progress*, *20*, 100717. https://doi.org/10.1016/j.tsep.2020.100717

Naphon, P., & Wongwises, S. (2010). Investigation on the jet liquid impingement heat transfer for the central processing unit of personal computers. *International Communications in Heat and Mass Transfer*, *37*(7), 822-826. https://doi.org/10.1016/j.icheatmasstransfer.2010.05.004

Saeed, M., & Kim, M. H. (2016). Numerical study on thermal hydraulic performance of water cooled mini-channel heat sinks. *International Journal of Refrigeration*, *69*, 147-164. https://doi.org/10.1016/j.ijrefrig.2016.05.004

Saeed, M., & Kim, M. H. (2017). Header design approaches for mini-channel heatsinks using analytical and numerical methods. *Applied Thermal Engineering*, *110*, 1500-1510. https://doi.org/10.1016/j.applthermaleng.2016.09.069

Song, J. Y., Hah, S., Kim, D., & Kim, S. M. (2019). Enhanced flow uniformity in parallel mini-channels with pin-finned inlet header, *Applied Thermal Engineering*, *152*, 718-733. https://doi.org/10.1016/j.applthermaleng.2019.02.069

Tang, B., Zhou, R., Bai, P., Fu, T., Lu, L., & Zhou, G. (2017). Heat transfer performance of a novel double-layer mini-channel heat sink. *Heat and Mass Transfer*, *53*(3), 929-936. https://doi.org/10.1007/s00231-016-1869-3

Tikadar A., Paul, T. C., Oudah, S. K., Abdulrazzaq, N. M., Salman, A. S., & Khan, J. A. (2020). Enhancing thermal-hydraulic performance of counter flow mini-channel heat sinks utilizing secondary flow: Numerical study with experimental validation. *International Communications in Heat and Mass Transfer*, *111*, 104447. https://doi.org/10.1016/j.icheatmasstransfer.2019.10444

Tikadar, A., Oudah, S. K., Paul, T. C., Salman, A. S., Morshed, A. K. M. M., & Khan, J. A. (2019). Parametric study on thermal and hydraulic characteristics of inter-connected parallel and counter flow mini-channel heat sink. *Applied Thermal Engineering*, *153*, 15-28. https://doi.org/10.1016/j.applthermaleng.2019.02.007

Wang, H. L., Wu, H. C., Wang, S. K., Hung, T. C., & Yang, R. J. (2013). A study of mini-channel thermal module design for achieving high stability and high capability in electronic cooling. *Applied Thermal Engineering*, *51*(1-2), 1144-1153. https://doi.org/10.1016/j.applthermaleng.2012.10.007

Xiao, H., Liu, Z., & Liu, W. (2020). Turbulent heat transfer enhancement in the mini-channel by enhancing the original flow pattern with v-ribs. *International Journal of Heat and Mass Transfer*, *163*, 120378. https://doi.org/10.1016/j.ijheatmasstransfer.2020.120378

Xu, S., Yang, L., Li, Y., Wu, Y., & Hu, X. (2016). Experimental and numerical investigation of heat transfer for two-layered microchannel heat sink with non-uniform heat flux conditions. *Heat and Mass Transfer*, *52*(9), 1755-1763. https://doi.org/10.1007/s00231-015-1691-3

Zhang, Q. Y., Li, Z. Z., Feng, Z. F, Chen, Z., Zhang, J. X. & Guo, F. W. (2023). Effects of combination modes of different cavities and ribs on performance in mini-channels - A comprehensive study. *International Communications in Heat and Mass Transfer*, *142*, 106633. https://doi.org/10.1016/j.icheatmasstransfer.2023.106633

KSÜ Mühendislik Bilimleri Dergisi, 26(Özel Sayı), 2023 KSU J Eng Sci, 26(Special Issue), 2023
9th Uluslararası IFS Çağdaş Matematik ve Mühendislik Konferansı Özel Sayısı
9th International IFS Contemporary Mathematics and Engineering Conference Special Issue
Araştırma Makalesi Research Article

Kahramanmaras Sutcu Imam University Journal of Engineering Sciences

Geliş Tarihi : 11.08.2023 Received Date : 11.08.2023
Kabul Tarihi : 27.09.2023 Accepted Date : 27.09.2023

HİGROSKOPİK MADDELERİN ÜRETİMİNDE KULLANILABİLİR SICAKLIK, BASINÇ VE KARIŞTIRMA KONTROLLÜ ULTRASONİK PİLOT REAKTÖR TASARIMI

ULTRASONIC PILOT REACTOR DESIGN: TEMPERATURE, PRESSURE AND ROTARY CONTROL CAN BE USED IN THE PRODUCTION OF HYGROSCOPIC MATERIALS

Sinan KÖSE [1*] (ORCID: 0000-0002-6224-3388)
Fatma ULUSAL [2] (ORCID: 0000-0001-6926-6251)
Salih Hakan YETGİN [3] (ORCID: 0000-0002-6068-9204)

[1] Tarsus Üniversitesi, Makine ve Metal Teknolojileri Bölümü, Mersin, Türkiye
[2] Tarsus Üniversitesi, Kimya ve Kimyasal İşleme Teknolojileri Bölümü, Mersin, Türkiye
[3] Tarsus Üniversitesi, Makine Mühendisliği Bölümü, Mersin, Türkiye

*Sorumlu Yazar / Corresponding Author: Sinan KÖSE, sinankose@tarsus.edu.tr

ÖZET

Çinko klorür, sodyum hidroksit, magnezyum oksit, kalsiyum oksit gibi maddeler kimyasal yapıları gereği kristalleri içerisine difüzyon/absorpsiyon gibi yollarla su tutarlar. Bu maddeler, higroskopik maddeler olarak adlandırılıp sıvı ve katılar maddelerden su uzaklaştırmak amacıyla kullanılmaktadır. Üretimleri amacıyla özel kapalı sistemler kullanılması gerekmekle birlikte ortama giren veya maddenin absorpladığı suyun ortamdan uzaklaştırılması ve kalsinasyon işlemleri için yüksek sıcaklıklarda tepkime odaları gerekmektedir. Higroskopik maddelerin tepkimesi sırasında ortaya çıkan gazların ortamdan uzaklaştırılması veya ürünün nemlenmesi önlemek için su buharının sistemden uzaklaştırılması gerekmektedir. Piyasada yer alan reaktörler incelendiğinde başta topaklanma, hantal yapıları, yüksek enerji gereksinimleri ve paketlenme süreçlerinde havayla temas gibi olumsuzluklar göstermektedirler. Bu çalışma ile kalsiyum oksit ve magnezyum oksit temel alınmak üzere, ilgili kimyasalların üretim prosesinde ve kimyasal tepkimelerinde kullanılmak amacıyla yeni bir pilot reaktör ünitesinin sınır şartlarının belirlenmesi ve 3B tasarımlarının yapılması amaçlanmıştır. Piyasada yaygın kullanımı olan reaktörler incelenerek sınır şartları belirlenmiştir. Belirlenen ihtiyaçlara göre 3 boyutlu tasarımları gerçekleştirilmiştir olup elde edilen verilere göre mevcut sistemlere göre %42 daha hafif, %50 daha küçük yeni bir sistem tasarlanmıştır. Çalışma ile en az %38 daha fazla ürün işleme kapasitesine sahip olup %25 oranında enerji kullanımını azaltan bileşenlerden oluşan yeni bir reaktörün tasarımı gerçekleşmiştir.

Anahtar Kelimeler: Higroskopik madde, reaktör tasarımı, higroskopik madde boyutlandırıcısı

ABSTRACT

Substances such-as zinc-chloride, sodium-hydroxide, magnesium-oxide, calcium-oxide retain water in-their crystals by means of diffusion/absorption due-to their chemical structure. These substances're called hygroscopic substances and are-used to remove water from liquids/solids. Although special closed systems're required for their production, reaction chambers at-high temperatures're required for the removal of-water that enters the environment or absorbed by material from environment and for calcination processes. It's necessary to remove gases formed during reaction of hygroscopic-substances from environment or to-remove water vapor from system to-prevent product from getting humid. When reactors in market're examined, they show negative aspects such-as clumping, bulky structures, high

ToCite: KÖSE, S., ULUSAL, F & YETGİN, S. H., (2023). HİGROSKOPİK MADDELERİN ÜRETİMİNDE KULLANILABİLİR SICAKLIK, BASINÇ VE KARIŞTIRMA KONTROLLÜ ULTRASONİK PİLOT REAKTÖR TASARIMI. *Kahramanmaraş Sütçü İmam Üniversitesi Mühendislik Bilimleri Dergisi*, 26(Özel Sayı), 1171-1176.

energy requirements and contact with air during packaging processes. In this study, it's aimed to determine boundary conditions and 3D designs of new pilot reactor unit to be used in-production process and chemical reactions of related chemicals, based-on calcium/magnesium oxide. Boundary conditions were determined by examining reactors that are widely used in market. 3D designs were made according to determined needs and according to data obtained, new system's designed, that is 42% lighter and 50% smaller than conventional systems. With study, new reactor was designed with components that have at-least 38% more product processing capacity and reduce energy use by 25%.

Keywords: Hygroscopic materials, reactor design, hygroscopic material sizing

GİRİŞ

Katı kimyasal maddelerin bir kısmı kimyasal yapıları gereği daha kararlı hale geçebilmek için kristalleri içerisine difüzyon ve absorpsiyon gibi yollarla su tutarlar. Çinko klorür, sodyum klorür, sodyum hidroksit, magnezyum oksit, kalsiyum oksit gibi maddeler bu kimyasal bileşiklere örnek verilebilir ve bu maddeler, higroskopik maddeler olarak adlandırılıp hem sıvı hem de katılar için ortamdan nemin ve suyun uzaklaştırılması için kullanılmaktadır. Higroskopik maddeler, normal şartlarda hava sıcaklığına ve ortam şartlarına bağlı olarak havada kütlece yüzde 0,2-4,0 kadar bulunan su buharı içeren hava ile temas ettiğinde su buharını absorplayarak nemlenmektedir. Nemlenme işleminin süresi, maddenin kimyasal yapısına ve bünyesine aldığı su miktarına bağlı olarak değişmektedir. Bazı maddeler bu suyu birkaç günde bünyesine alırken bazı maddeler birkaç saniye süreyle hava ile temas ettiğinde bile nemlenmektedir. Bazı durumlarda bu işlem zararsız olsa da bazen su ile higroskobik maddelerin teması aşırı ısınma, patlama gibi sonuçlarla tamamlanabilmektedir. Haliyle bu olumsuzluklar higroskopik maddelerin üretilmesi, depolanması ve kullanılmasını oldukça zorlaştırarak dezavantajları oluşturmaktadır. Higroskopik maddelerin üretimi amacıyla özel kapalı sistemler kullanılması gerekmekle birlikte ortama giren veya maddenin absorpladığı suyun ortamdan uzaklaştırılması ve kalsinasyon işlemleri için yüksek sıcaklıklarda tepkime odaları gerekmektedir (Liang vd., 2021; Deng vd., 2021; Wang vd., 2012; Olalekan ve Simonson, 2006). Higroskopik malzemeler suyu sadece "H2O" şeklinde bünyesinde kristal suyu veya nem olarak absorplayabilecekleri gibi bazen de bu su ile tepkime vererek başka bir maddeye dönüşmektedir. Eğer madde suyu, kristal suyu veya nem olarak absorplarsa 70-80 ºC gibi düşük sıcaklıklarda bile bu su desorplanarak madde eski haline döndürülebilmektedir. Buna örnek olarak sodyum asetat ($NaCH_3COO$) katısı verilebilir. Sodyum asetat kristal yapısında 3 tane su molekülü bulundurmaktadır ve 130 ºC üzerinde kristal suyunu kaybederek susuz formunu oluşturur (Sharma vd., 1991). Ancak kalsiyum oksit (CaO) gibi maddeler su ile ısı vererek tepkimeye girip kalsiyum hidroksit (Ca(OH)2) oluşturmaktadır. Yeni oluşan ürünün fiziksel ve kimyasal birçok özelliği değişerek tamamen farklı bir madde gibi davranabilir.

Higroskopik malzemelerin absorpladıkları suyun uzaklaştırılması için en temel teknik ısıtmadır. Ancak ısıtma sonunda elde edilen susuz ürünün su veya nem ile aniden karşılaşması patlama gibi durumlara neden olabileceği için kapalı sistemlerin kullanılması gerekmektedir (Kallenberger ve Fröba, 2018). Bununla birlikte homojen bir ısıtma ve kurutma sırasında kalıplaşmanın/topaklaşmanın önüne geçebilmek amacıyla mekanik karıştırma sistemi bulunmalıdır. Higroskopik maddelerin tepkimesi sırasında ortaya çıkan gazların ortamdan uzaklaştırılması veya ürünün nemlenmesini önlemek için su buharının sistemden uzaklaştırılması veya inert bir gaz ile sirkülasyon yapılması gerekmektedir. Higroskopik maddelerin hem kristal suyu olarak yapılarına aldıkları hem de tepkime vererek yapılarına kattıkları suyun uzaklaştırılması için silindirik yapıdaki mekanik karıştırma sistemleri ön plana çıkmaktadır. Bu amaçla helis sistemler veya basit çubuklu karıştırıcılar kullanılmaktadır (He vd., 2021). Bu sistemlerin ısıtmalı ve ısıtmasız olanları mevcut olmakla birlikte bünyesine aldığı suyla tepkimeye giren malzemelerin susuzlaştırılması için yüksek sıcaklıklar gerekmektedir. Kalsiyum hidroksit gibi bir malzemenin susuzlaştırılması için en az 650 ºC, lityum hidroksit 780 ºC, sodyum hidroksit için 700 ºC üzerine çıkılması gerekmektedir (Kiat vd., 1998).

Kimyasal tozların susuzlaştırılması için çeşitli yöntemler geliştirilmiştir. CN218047746 (U) ― 2022-12-16 patentte helis yapısında geliştirilmiş sistemler kullanılmış, helis sistemde karıştırma işlemi gerçekleştirilmiştir (European Patent Office, 2023a). Ancak kullanılan sistem taneciklerin istenen nem oranına kadar susuzlaştırılması için yetersiz kalmış ve bunun yanında katı tanecikleri topaklanarak istenmeyen boyutlara kadar büyümüştür. CN217662704 (U) ― 2022-10-28 patent başvurusunda yapılan çalışmada karıştırma işlemi mekanik bir çubuk ile gerçekleştirilmiş ısıtma modülünün yanında işlem sonrası soğutma modülü de eklenmiştir (European Patent Office, 2023b). Sistemin temelini silindirik bir yapı oluşturmakla birlikte homojen özelliklere sahip topaklanma olmayan tozların üretilmesi için yetersiz olduğu görülmüştür. Bunun temel nedeni ise mekanik karıştırma sırasında kör cephelerdeki yapışan maddelerin topaklanmasıdır. Örnekleri verilen sistemlerde topaklanma, homojen karışmama, yetersiz oranda susuzlaştırmanın yanı sıra yüksek enerji ve imalat maliyetleri de dezavantajları oluşturmaktadır.

Bu çalışmada higroskopik nano/mikropartiküllerin homojen karışmasını sağlayacak, istenen oranda susuzlaştırma sağlayacak mekanik karıştırmaya alternatif yeni bir yöntemin kullanıldığı silindirik borulardan meydana gelmiş ısıtma bileşenlerinin ortam içerisinde konumlandırıldığı ve bu borulardan yüksek hızla hareket eden hava ile homojen karıştırma sağlayan yeni bir reaktör sistemi geliştirilmiştir. Geliştirilen sistem sayesinde topaklanma olmaksızın homojen karışmanın sağlandığı modüler yapıda soğutma, paketleme granülleştirme ünitelerinin yer aldığı prosesler için kesintisiz işlem yapmayı sağlayan bir sistemin tasarımı elde edilmiştir.

MATERYAL VE YÖNTEM

Higroskopik maddelerin üretimi, stoklanması ve tepkimeleri incelendiğinde havadaki su buharının oldukça hızlı bir şekilde tepkime vermesiyle maddenin bozunduğu veya tepkimenin gerçekleşmesini engellediği görülmektedir. Bu amaçla tasarlanan ve kullanılan reaktörler incelendiğinde genelde kapalı ısıtma sisteminin varlığı söz konusudur. Bu sistemlerde 800-950 ºC gibi yüksek sıcaklıklarda çalışma yapıldığı ve maddenin spesifik özelliğinden kaynaklı tanecik boyutunun ayarlanması ve tepkime süresince mekanik karıştırma proseslerinin topaklanma vb., sorunlara neden olduğu görülmektedir. Ayrıca ülkemizde higroskopik madde tepkimelerinin yapılabileceği bir cihazın üretimi de söz konusu değildir.

Çalışmada piyasada yaygın olarak kullanılan konvansiyonel higroskopik madde reaktörleri incelenmiştir. Çukurova Teknoloji Geliştirme Bölgesinde faaliyet gösteren Kimya Vadisi A.Ş pilot tesisinde yer alan çok fonksiyonlu higroskopik madde üretim reaktörü (Şekil 1) incelenmiştir. Operatörler ve teknik datalar üzerinden sistemin dezavantajlı durumları tespit edilerek tasarlanacak olan yeni reaktörün sınır şartlarının oluşturulmasında bu veriler kullanılmıştır.

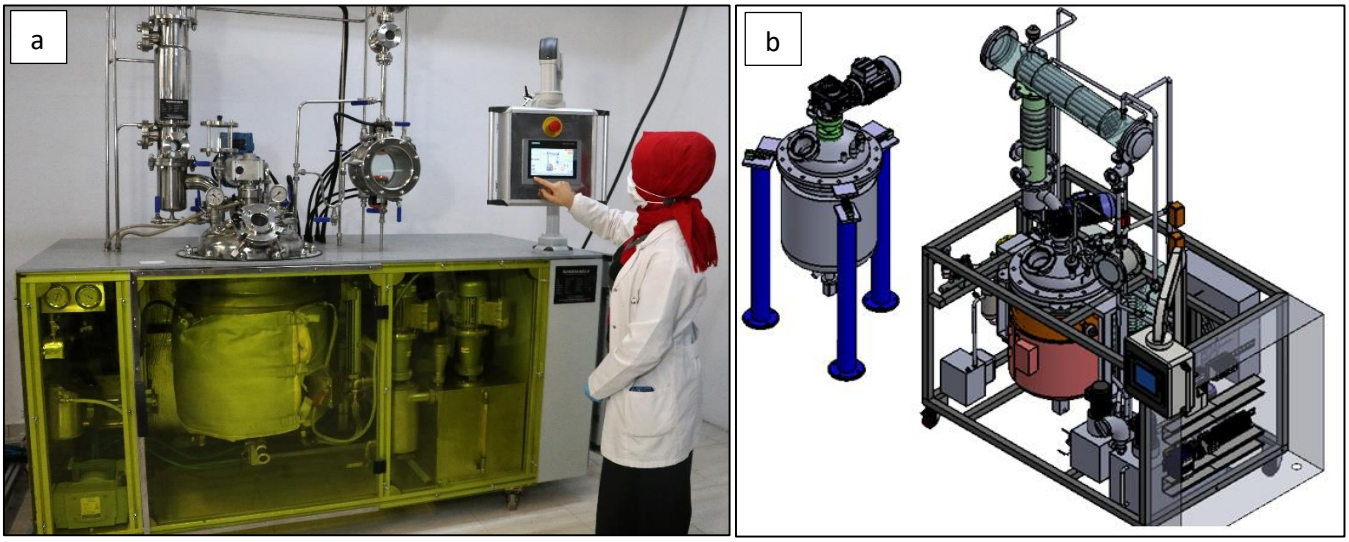

Şekil 1. a. Ultra Fonksiyonlu Higroskopik Madde Reaktörü, **b.** Reaktör Teknik Resmi

Şekil 1'de yer alan ve Kimya Vadisi A.Ş pilot tesisinde kullanılmakta olan higroskopik reaktörüne karşı piyasada konumlanmış ilgili ürüne rakip reaktörlerde incelenmiştir. GEA Group (Germany) büyesinde üretilen reaktörlerde incelenerek elde edilen veriler dahilinde 3 boyutlu tasarım aşamasına geçilmiştir.

Bilgisayar destekli (Computer Aided Design) programı için Solidworks 2018 (v2018, Groupe Industriel Marcel Dassault SAS, France) katı modelleme yazılımı kullanılmıştır. Katı modelleme programı ile farklı tasarımlar geliştirilmiş olup ön prototip öncesi kullanılacak olan teknik resim detayları elde edilmiştir. Elde edilen veriler ve tasarımların fikri ve sınai mülkiyet haklarının korunabilmesi amacıyla Türk Patent Enstitüsü (TPE- 2023/002235) nezdinde patent başvurusu yapılmıştır.

BULGULAR

Piyasada kullanılmakta olan ürünler incelendiğinde başta topaklanma (Şekil 2) olmak üzere hantal yapıları, sistemi oluşturan bileşen sayılarının (component) fazlalığı, karıştırmada homojenlik problemi, topaklanma kaynaklı büyük

tanecik boyutları, mekanik karıştırıcıdan kaynaklı ürünün cidarlara yapışma sorunu, yüksek maliyetler, yüksek enerji tüketimi, yetersiz susuzlaştırma oranı, paketleme ve diğer prosedürler için kısıtlı fonksiyonlar ön plana çıkmıştır.

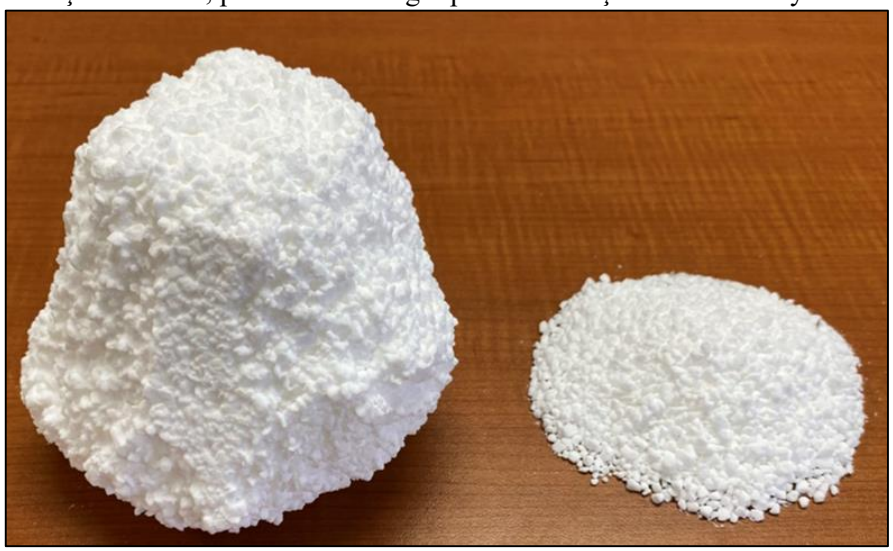

Şekil 2. Hidratize Olmuş Higroskopik Maddelerin Topaklanması

Tasarım öncesi mekanik karıştırma ünitesi yerine sıcak hava kullanılarak higroskopik maddelerin karıştırılması üzerine odaklanılmıştır. Bu amaçla mekanik karıştırma yönteminin aksine sıcak hava ile karıştırma tüpleri içerisinde higroskopik maddelerin karıştırılmasına odaklanılmıştır (Şekil 3). Bu tüpleri AISI 304 paslanmaz çelik malzemelerden tasarlanmış olup, sektörlere bağlı olarak oluşabilecek basınçlara karşı oldukça dirençlidir. Organik kimyasallara, inorganik kimyasallara ve renkli boyalara karşı dayanıklıdır. Karıştırma borularının et kalınlığı 2 mm alınarak sistemin tasarımı gerçekleştirilmiştir. Ayrıca ısıtıcılar konvansiyonel sistemlerdeki gibi dış ünite çeperine yerleştirilmeden karıştırma boruları içerisine konumlandırılmıştır. Mevcut sistemlerdeki bir diğer sorun olan topaklanma için karıştırma boruları tarafına sonikatörler yerleştirilerek titreşim yayları ile sistem içerisinde yer alan tozların birbirleriyle çarpışmaları ve cidara yapışmalarının önüne geçilmesi amaçlanmıştır.

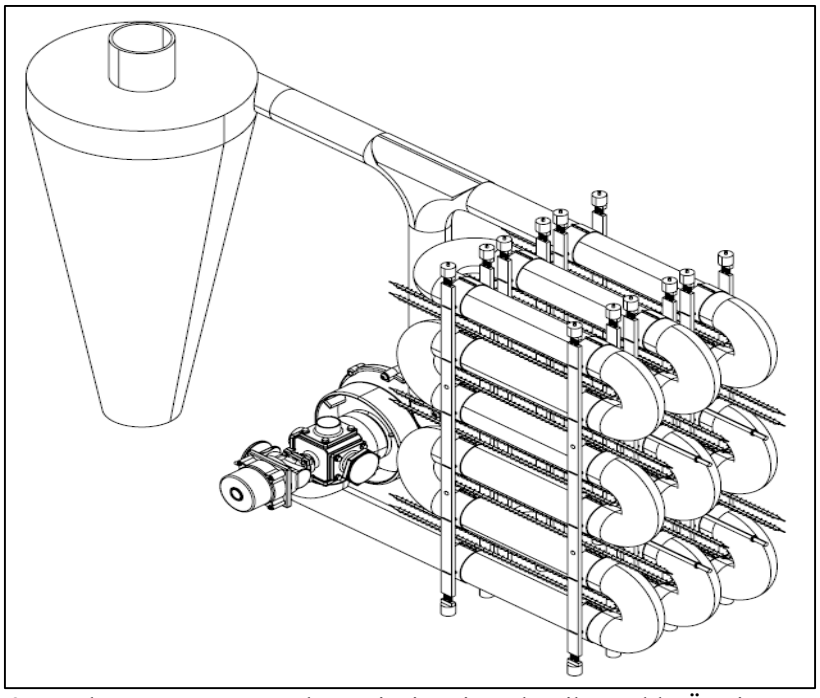

Şekil 3. Sıcak Hava Karıştırmalı Yeni Tip Higroskopik Madde Üretim Reaktörü

Tasarım süreçlerinde piyasada kullanılan reaktörlerin kapasiteleriyle birebir uyumlu sistem tasarımı gerçekleştirilmiştir. Kimya Vadisi AŞ Pilot Tesiste yer alan 50 litre işleme kapasiteli ürüne göre tasarım çalışması yapılmıştır (Şekil 4 a). Bu tasarım için mekanik sistem yerine kullanılan boru tipi karıştırma ünitesi (Şekil 4 b) sistemin boyutlarının yaklaşık %50'lik küçülmesine imkân sağlamıştır. Karıştırma boruları içerisine

konumlandırılmış metal yapraklar proses süresinde boru içerisinde sıcak hava ile hareket etmekte olan higroskopik tozların birbirlerine çarpmasına ve topaklanmalarının önlenmesine neden olmaktadır. Yapraklar 1mm kalınlıkta paslanmaz çelik malzemelerden olup boruların dirsek bölgeleri dışındaki düz hatlarının içerisine kendi eksenleri etrafında açı verilerek şekillendirilmiş üç kanatlı yapı formunda konumlandırılmıştır. Bu yapraklar boru içerisinde yüksek hızlarda hareket eden tozların dağınık hareket ederek birbirlerine çarpmasını sağlamaktadır. Böylece topaklanama başta olmak üzere cidara yapışmanın da önüne geçilmektedir. Ayrıca cidara yapışmakta olan tozlar sonikatörler ile sistemin akış hattına dahil edilmektir.

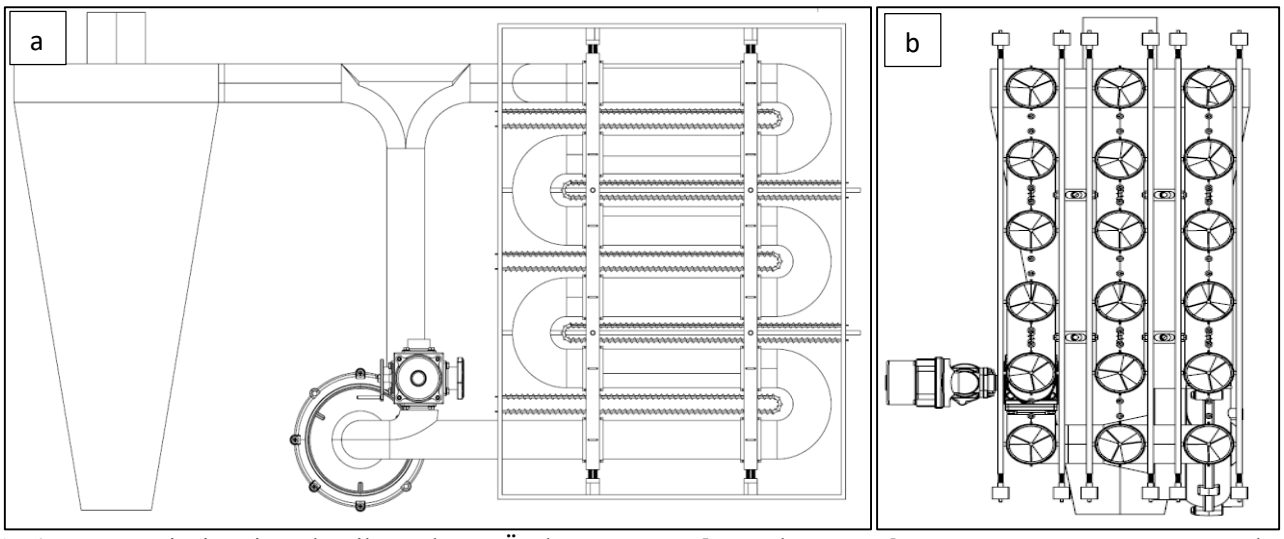

Şekil 4. a. Yeni Tip Higroskopik Reaktörü Önden Görünüş, **b.** Reaktör Yandan Görünüşü, Karıştırma Boruları

Sistemin tasarım süreçlerinde malzeme atamaları yapılarak elde edilen reaktör tasarımının yaklaşık ağırlığı hesaplanmıştır. Sistemde kullanılan bileşenler sadeleştirilerek (vakum pompası ve bileşenleri, koruyucu kabin, mekanik karıştırıcı ve haznesi, inert gaz haznesi ve bileşenleri kullanılmamıştır) sistemin ağırlığı %42 oranında azaltılmıştır. Sistemde kullanılan pompalar, motorlar ve ısıtıcıların enerji tüketimleri hesaplanmış olup konvansiyonel reaktörlere oranla %25 daha az enerji maliyeti ortaya çıkacağı hesaplanmıştır. Mevcut yapıların ürün işleme kapasitelerine (50 litrelik işleme haznesine göre) göre yapılan tasarımlar ayrıca boyutsal denkliğe göre de gerçekleştirilmiştir. Sistem işleme haznesine konulan tozların tamamı aynı anda prosese dahil edilebilir yapıdadır. Tasarımımızın piyasada kullanılan ve karşılaştırma amacıyla kullandığımız ürünler ile aynı boyutlara sahip olması durumunda ise (mm cinsinden (uzunluk*yükseklik*genişlik), 1906*2450*1069) ürün işleme kapasitesi asgari %38 oranında daha yüksek olduğu hesaplanmıştır.

TARTIŞMA VE SONUÇ

Higroskopik maddelerin üretimi, stoklanması ve tepkimeleri incelendiğinde havadaki su buharının oldukça hızlı bir şekilde tepkime vermesiyle maddenin bozunduğu veya tepkimenin gerçekleşmesini engellediği görülmektedir. Bu amaçla tasarlanan ve kullanılan reaktörler incelendiğinde genelde kapalı ısıtma sisteminin varlığı söz konusudur. Bu sistemlerde 800-950 ºC gibi yüksek sıcaklıklarda çalışma yapıldığı ve maddenin spesifik özelliğinden kaynaklı topaklanma, tanecik boyutunun ayarlanması ve tepkime süresince mekanik karıştırma prosesi büyük sorunlara neden olabilmektedir.

Mevcut reaktörler ile karşılaştırıldığında ortaya konan bu çalışma öncelikle karıştırma metodolojisi ile özgünlüğünü ortaya koymaktadır. Piyasada kullanılan konvansiyonel higroskopik madde üretim reaktörlerinin mekanik karıştırma yöntemine bağlı olarak üretilmeleri başta ürün çıktıları üzerine (topaklanma, cidara yapışma, maddeden yeterli düzeyde nem/su uzaklaştırılamama vd.,) çeşitli sorunları ortaya çıkarmaktadır. Bu sorunların giderilebilmesi için mevcut sistemlerde iyileştirmelerin yanı sıra higroskopik madde üretimi için alternatif karıştırma ünitelerinin de tasarımı önem kazanmaktadır. Bu çalışma ile özellikle karıştırma ünitesinde yeniliğe gidilmiş bilgisayar ortamında elde edilen veriler ile piyasada kullanılan konvansiyonel reaktörlerin karşılaştırılması yapılmıştır. Elde edilen karşılaştırma verilerinin doğruluğu için tasarımı ve teknik resimleri oluşturulan yeni tip reaktörün prototip imalatı gerçekleştirilerek bu çalışmadaki sonuçlar ile karşılaştırılması yapılmalıdır.

TEŞEKKÜR

Bu çalışma Tarsus Üniversitesi Bilimsel Araştırma Projeleri (BAP) kapsamında OSB.22.005 proje numarasıyla desteklenmiştir.

KAYNAKLAR

Deng, F., Wang, C., Xiang, C. and Wang, R. (2021). Bioinspired topological design of super hygroscopic complex for cost-effective atmospheric water harvesting. *Nano Energy*, 90, B. https://doi.org/10.1016/j.nanoen.2021.106642.

Europen Patent Office. (2023a). https://worldwide.espacenet.com/patent/search/family/083712025/publication/CN217662704U?q=num%20%3D%20%22CN217662704%22. Accessed 10.08.23

Europen Patent Office. (2023b). https://worldwide.espacenet.com/patent/search/family/083712025/publication/CN217662704U?q=num%20%3D%20%22CN217662704%22

He, F., Weon, S., Jeon, W. et al. (2021). Self-wetting triphase photocatalysis for effective and selective removal of hydrophilic volatile organic compounds in air. *Nat Commun*, 12, 6259. https://doi.org/10.1038/s41467-021-26541-z

Kallenberger, P. A., Fröba, M. (2018). Water harvesting from air with a hygroscopic salt in a hydrogel–derived matrix. *Commun Chem*, 1, 28. https://doi.org/10.1038/s42004-018-0028-9.

Kiat, J. M., Boemare, G., Rieu, B. and Aymes, D. (1998). Structural evolution of LiOH: evidence of a solid–solid transformation toward Li2O close to the melting temperature. *Solid State Communications*, 108, 4, 241-245, https://doi.org/10.1016/S0038-1098(98)00346-9.

Liang, J., Zhang, X., Ji, J. (2021). Hygroscopic phase change composite material—A review. *Journal of Energy Storage*, 36. https://doi.org/10.1016/j.est.2021.102395

Osanyintola, O. F. and Simonson, J. C. (2006). Moisture buffering capacity of hygroscopic. 38, 1270-1282,. https://doi.org/10.1016/j.enbuild.2006.03.026.

Sharma, S. K., Jotshi, C. K., and Kumar, S. (1991). Kinetics of dehydration of sodium salt hydrates. *Thermochimica Acta*, 184(1), 9–23. https://doi.org/10.1016/0040-6031(91)80130-b.

Wang, W., Wu, L., Li, Z., Fang, Y., Ding, J. and Xiao, J. (2013) An overview of adsorbents in the rotary desiccant dehumidifier for air dehumidification. *Drying Technology*, 31, 12, 1334-1345. https://doi.org/10.1080/07373937.2013.792094.

KSÜ Mühendislik Bilimleri Dergisi, 26(Özel Sayı), 2023 KSU J Eng Sci, 26(Special Issue), 2023
9th Uluslararası IFS Çağdaş Matematik ve Mühendislik Konferansı Özel Sayısı
9th International IFS Contemporary Mathematics and Engineering Conference Special Issue
Araştırma Makalesi Research Article

Kahramanmaras Sutcu Imam University
Journal of Engineering Sciences

Geliş Tarihi : 09.08.2023 Received Date : 09.08.2023
Kabul Tarihi : 25.09.2023 Accepted Date : 25.09.2023

CLASSIFICATION OF BRAIN TUMORS ON MRI IMAGES USING DEEP LEARNING ARCHITECTURES

DERİN ÖĞRENME MİMARİLERİ KULLANILARAK MRI GÖRÜNTÜLERİ ÜZERİNDE BEYİN TÜMÖRÜ SINIFLANDIRMASI

Samaneh SARFARAZI[1] (ORCID: 0009-0007-5139-5662)
Önsen TOYGAR[2*] (ORCID: 0000-0001-7402-9058)

Computer Engineering Department, Faculty of Engineering, Eastern Mediterranean University, 99628, Famagusta, North Cyprus, via Mersin 10, Turkey

*Sorumlu Yazar / Corresponding Author: Önsen TOYGAR, onsen.toygar@emu.edu.tr

ABSTRACT

A brain tumor is a dangerous neural illness produced by the strict growth of prison cells in the brain or head. The segmentation, analysis, and separation of unclean tumor parts from Magnetic Resonance Imaging (MRI) images are the main sources of anxiety. To report the segmented MRI images including tumor, the usage of computer-assisted methods is necessary. In this paper, a Convolutional Neural Network (CNN) approach is applied to identify brain cancers in MRI images. Two datasets are used in this study, namely Kaggle Brain MRI database and Figshare Brain MRI database. Models of deep CNN, consisting of VGG16, AlexNet, and ResNet, are utilized to extract deep features. The classification accuracies of the aforementioned Deep Learning (DL) networks are used to measure the efficiencies of the implemented systems. For the Kaggle database, AlexNet achieves 98% accuracy, VGG16 has 97% accuracy and ResNet has 66% accuracy. Among these networks, AlexNet has provided the highest level of accuracy. In the Figshare dataset, AlexNet and VGG16 both achieve 99% accuracy, and ResNet has 96% accuracy. In terms of accuracy, AlexNet and VGG16 outperform ResNet. These performances aid in the early detection of cancers before they cause physical harm such as paralysis and other complications.

Keywords: Brain tumor classification, convolutional neural networks, deep learning

ÖZET

Beyin tümörü, beyindeki veya kafadaki hapishane hücresinin katı bir şekilde büyümesiyle üretilen tehlikeli bir nöral hastalıktır. Manyetik Rezonans Görüntüleme (MRI) görüntülerinden temiz olmayan tümör parçalarının segmentasyonu, analizi ve ayrılması kaygının ana kaynağıdır. Tümör içeren MRI görüntülerinin raporlanabilmesi için bilgisayar destekli yöntemlerin kullanılması gerekli hale gelmiştir. Bu makalede, MRI görüntülerinde beyin tümörlerini tanımlamak için Evrişimli Sinir Ağları (CNN) yaklaşımı kullanılmıştır. Bu çalışma için Kaggle Brain MRI veri kümesi ve Figshare Brain MRI veri kümesi olmak üzere iki veri kümesi kullanılmıştır. Derin öznitelikleri çıkarmak için VGG16, AlexNet ve ResNet'ten oluşan derin CNN modelleri kullanılmıştır. Söz konusu Derin Öğrenme (DL) modellerinin sınıflandırma doğrulukları, uygulanan sistemlerin verimliliklerini ölçmek için kullanılmıştır. Kaggle veri kümesi için AlexNet %98, VGG16 %97 ve ResNet %66 doğruluk elde etmiştir. Bu ağlar arasında AlexNet en yüksek düzeyde doğruluk sağlamıştır. Figshare veri kümesinde ise, AlexNet ve VGG16'nın her ikisi de %99, ResNet ise %96 doğruluk elde etmiştir. Doğruluk açısından AlexNet ve VGG16, ResNet'ten daha iyi performans göstermiştir. Bu performanslar, kanserlerin felç ve diğer komplikasyonlar gibi fiziksel zararlara yol açmadan önce erken teşhis edilmesine yardımcı olacaktır.

Anahtar Kelimeler: Beyin tümörü sınıflandırması, evrişimli sinir ağları, derin öğrenme

ToCite: SARFARAZI, S., & TOYGAR, Ö., (2023). CLASSIFICATION OF BRAIN TUMORS ON MRI IMAGES USING DEEP LEARNING ARCHITECTURES. *Kahramanmaraş Sütçü İmam University, Journal of Engineering Sciences*, 26(Özel Sayı), 1177-1186.

INTRODUCTION

A brain tumor is an imbalanced type of cell in the human brain. The brain of a human is surrounded by a firm head. Slight development in such a minor part will cause intense problems. Tumors of brain may be malignant and nonmalignant. The gravity inside the head will increase such as nonthreatening or malicious cancers progress. This will result in enduring head damage or death of the person. Experts and investigators have been studying complex methods and approaches aimed at diagnosing tumors of brain. While MRI image depictions and Tomography of Computer (CT) are the two approaches with broad usage in which both aimed at clarifying the anomalies in form, mass, or brain materials place, that help doctors in identifying cancers; MRI image is preferred more than the aforementioned methods by the specialists. Therefore, experts and scientists have used MRI images. However, automatic methods, mostly applied by computer-assisted medicinal image processing methods, exist progressively helping surgeons to notice tumors of brain. Handcrafted methods with Machine Learning (ML) classifiers are developed for training data examples.

Medicinal image processing includes pre-processing and post-processing. These stages may be applied through the Handcrafted methods as perfect as the method of deep learning. In handcrafted methods, features are extracted to get consequences from images of the test and the procedure is quick. In the DL methods, networks are adjusted through properly choosing the sum of layers, activation function, and pooling. But, in both methods, new algorithms are possible to be employed to increase the system's accuracy in a wider viewpoint. DL techniques for identifying brain cancers in MRI scans are the topic of this paper. The main part of this paper focuses on finding tumors of brain through MRI images using methods of DL. Consequently, this paper will offer the anticipated result i.e., an effective DL method to distinguish tumors of brain by MRI images that will contribute to medical experts to run appropriate cures. Sample MRI images on both Kaggle (Kaggle Brain Tumor Dataset, 2020) and Figshare (Figshare Brain Tumor Dataset, 2018) datasets for healthy and unhealthy brains are demonstrated in Figure 1 and Figure 2, respectively.

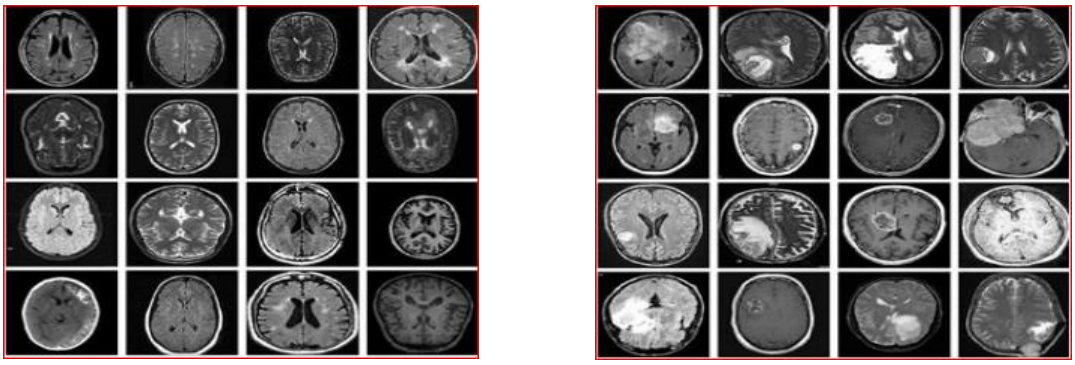

(a) (b)

Figure 1. a. Samples of Kaggle Database Healthy Brain MRI and **b.** Unhealthy Brain MRI Images

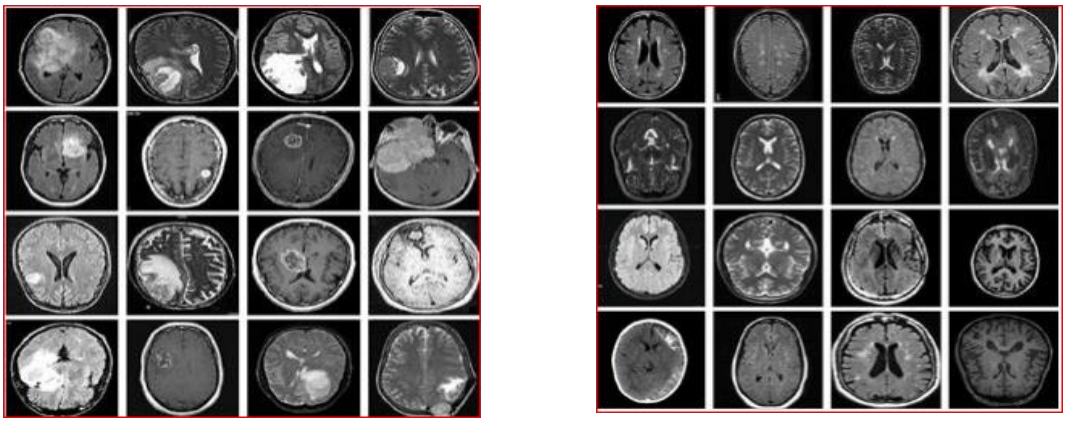

(a) (b)

Figure2. a. Samples of Figshare Database Healthy Brain MRI and **b.** Unhealthy Brain MRI Images

The following is the structure of the paper. Background on brain tumor classification and the works done by other researchers using handcrafted and DL methods are presented in Section 2. In Section 3, the paper methodology and metrics for evaluations are presented. Section 4 presents the experimental results, discussion and comparison with the state-of-the-art. Lastly, Section 5 gives the conclusions of this paper and future directions.

RELATED WORK

This section in brief deliberates the research that is shown to distinguish tumors of brain using the dissimilar advanced know-how. Rehman et al. (2021) recommended a different knowledge-founded technique for mini tumor of brain finding and type of tumor classification. The initial stage of their study focused on using a 3D CNN to abstract tumors in the brain, which were then transferred to a CNN model having already received training to abstract model features. The features that have been extracted are carried out to a correlation-based election procedure, and the greatest characteristics are selected in place of the outcome. In the last classification, with the usage of Feed Forward Neural Network (FFNN), the elected features are tested.

Amin et al. (2018) used a Deep Neural Network (DNN) based design for brain tumor segmentation. The suggested model has seven layers in the classification stage, including three ReLU layers, three convolutional layers, and a SoftMax layer. On the other hand, Kebir & Mekaoui (2018) suggested an approach that is supervised for identifying the anomalies of brain through the MRI images in several phases. The initial stage is to change a DL based CNN model, and after that, a subclass of MRI brain images is completed via the k-mean process conformed by the factor of brain grouping as standard or nonstandard groups in accordance with the advanced CNN model.

Alternatively, Vinoth & Venkatesh (2018) introduced a CNN-based automatic separation technique. At this point, classification was done with kernels, and Support Vector Machine (SVM) classification was done with computed variables. Furthermore, MATLAB is used to extract and recognize malignancies from MRI images of the brain. A CNN founded as a model of DL was effectively connected to the regarded issue of tumor of brain classification. Classifiers based on CNN constructions have the advantage of not requiring bodily sectioned tumor zones.

Talo et al. (2019) classified normal and pathological Brain MRI images with 100% accuracy by means of the ResNet34 pre-trained CNN model through a data augmentation technique of transfer learning. On the other hand, a model of the pre-trained ResNet50 CNN was updated (Çınar & Yıldırım, 2020) by eliminating the preceding five levels and replacing them with eight new layers, matching the accuracy of prior pre-trained patterns as ResNet50, AlexNet, and GoogleNet. The reconstructed ResNet50 pattern achieved 97.2% accuracy indicating real repercussions. There are several ML approaches for brain tumor classification and segmentation using MRI in scientific literature.

Hasan et al. (2019) suggested an image of an MRI brain scan categorization system based on deep and custom features. Preprocessed MRI image is useful for an altered Gray Level Co-occurrence Matrix (GLCM) for extraction of statistical features. CNN extracts features automatically. SVM classification with 10-fold Cross-validation performed 99.30% based on 600 sagittal MRI scans. While likened to new networks of transfer learning, such as GoogleNet and AlexNet, the recommended method performed fine on the other hand by means of combining CNN and GLCM features.

In another study, a Naive Bayes based brain cancer identification approach employed a maximum entropy segmentation (Zaw et al., 2019). The REMBRANDT dataset, which includes 114 MRI images, is used to examine the system. The recommended system has the advantage of detecting tumors anywhere in the brain, such as the temporal lobe. On the other hand, Sert et al. (2019) proposed a different scheme aimed at detecting brain tumors using a combination of CNN and advanced segmentation techniques utilizing maximum fuzzy entropy to improve the resolution of MRI, the super resolution of a single image is employed. Pre-trained ResNet architecture is used to extract features. SVM with binary classification has a 95% accuracy rate.

Edge Adaptive Total Variation (EADTV) (Deepak & Ameer, 2019) applied the mean shift clustering approach in regard to brain tumor categorization segmentation. The proposed technique has 2 advantages: When utilizing the image, EADTV preserves the edges with mean shift clustering, unlike K-mean and fuzzy c-means, and automatically updates cluster centers. In a combined approach of Particle Swarm Optimization (PSO) with fusion features for tumor of brain diagnosis, a fine-tuned Capsule Network feature extraction and Local Binary Patterns are applied. SVM classification accuracy on the BRATS2018 and RIDER databases is 98.3 % and 97.9%, respectively. The new

proposal has shown good results by combining handcrafted and deep features. On the CEMRI dataset, SVM and kNN classifiers are used to assess pre-trained GoogleNet for deep feature extraction for 3 class classification into Glioma, Meningioma with accuracy of 97.8% and 98%, respectively. The BRATS 2017 dataset, which contains 48 images, is used to assess the accuracy of a multinomial logistic regression model for brain tumor categorization. The system's functioning, however, should be evaluated on bigger databases.

Narayana & Reddy (2018) proposed a system that works well with the 9 Genetic Algorithm (GA) based SVM classification method. In an effective brain tumor classification optimization technique, GA is employed in order to segment tumors. SVM and GLCM texture characteristics provided 91.23 % performance for high-grade glioma (HGG) and low-grade gliomas (LGG) brain tumor categorization.

Polly et al. (2018) developed a k-means segmentation algorithm. From wavelet features, Principal Component Analysis (PCA) is employed to determine ten relevant features. On the way to discriminate between images that are normal and abnormal, SVM algorithm is utilized. Once again, SVM classification method is employed on the way to classify LGG and HGG tumors in aberrant images. On 440 images, the suggested technique achieves 99 %, but it needs to be evaluated on a larger database using added important data.

Amin et al. (2018) suggested a new technique for identifying brain tumors using MRI. To reduce noise and smooth MRI, skull stripping and Gaussian filtering were used. Following K-means segmentation, GLCM texture characteristics were extracted. The system was tested on three datasets: local, AANLIB, and RIDER. They used linear, RBF, and cubic SVM kernels. The linear kernel with 5-fold cross validation was found to have 98% accuracy. On the other hand, Minz & Mahobiya (2017) provided a study that uses the AdaBoost classifier to classify brain tumors. Following Median filtering, threshold-based segmentation is used to reduce noise. Using GLCM characteristics, the system proposed texture-based classification.

Shankar et al. (2016) proposed exploiting texture features to classify brain tumors using Gustafson-Kessel(G-K) fuzzy clustering. A histogram-based approach is used to segment preprocessed images with the Wiener filter. G-K fuzzy manner was given GLCM texture features for binary classification with 95% accuracy. The detection of brain tumors using systems of DL was a cutting-edge subject of study. Researchers use a variety of DL architectures to automatically segment and classify brain tumors. For brain classification, Regularized Extreme Learning Technique with Mix Features was also recommended via Gumaei et al. (2019).

A feature extractor of Hybrid PCA-NGIST can be utilized for 3-D feature extraction. The NGIST feature descriptor is a descriptor of standardized feature that is utilized to address image illumination and shadowing issues. RELM is a single hidden layer, input, and output FFNN. The suggested technique is examined for three kinds of tumors: neuroendocrine tumor, glioma, and pituitary tumor using CE-MRI database with 94.33 % after 5 fold cross-validation. Link Net is a small DNN design that is employed to group brain cancers (Hemanth et al., 2019). On a freely released UCI repository database, binary classification achieved 91% accuracy. The Multi-Layer Perceptron (MLP) classification system has a 96 % accuracy rate and a 0.65 Kappa Statistic. However, sparse auto encoder could be examined in forthcoming years when DNN is integrated with other auto encoder versions like denoising auto encoder.

Latif et al. (2018) proposed a brain tumor classification technique derived from transfer learning. To suit the VGG19 network with MRI images that are scaled to 224×224 pixels. To update the weights, fine tweaking of parameters such as learning rate, scheduling rate, and momentum is done block by block. The system has 94.82% accuracy on the CE-MRI database. The disadvantage of that approach is that fine-tuning settings block by block takes 20-30 minutes to train CNN classifier. MLP uses statistical and wavelet features to classify brain tumors (Mohsen et al., 2018).

METHODOLOGY FOR BRAIN TUMOR CLASSIFICATION

This section reviews three CNN based DL architectures implemented for brain tumor classification in this study. The methodology used in this paper for the implementation of brain tumor classification employs AlexNet, VGG16, and ResNet architectures. The main contribution of this paper is to present the implementation of deep learning based AlexNet, VGG16, and ResNet architectures for brain tumor classification separately. The evaluation metrics for the presentation of the experimental results are then discussed in the following section. CNN is the most well-known and extensively utilized approach in the field of DL. CNN's key benefit over its predecessors is that it accurately

characterizes relevant characteristics with almost no human intervention. Face recognition, computer vision, audio processing, and other applications have all benefited from CNN. The development of CNN was invigorated by neurons in humans. A typical type of CNN has many convolutions pooling layers, similar to an MLP, except the end layers are Fully Connected layers. In this paper, three of the aforementioned architectures, namely AlexNet (Huafeng et al., 2015), VGG16 (Simonyan & Zisserman, 2014), and ResNet (Wang & Gong, 2020) are implemented for brain tumor classification.

A general block diagram of the implemented system with a general CNN architecture is shown in Figure 3. The methodology used in this study for the implementation of brain tumor classification starts with the brain MRI images that are used as the input of the system, and then the system employs AlexNet, VGG16 and ResNet architectures separately to classify the input images with or without tumors. Feature extraction and classification are performed by the DL architecture automatically and the output is produced at the end of this process. The output of the system for images with tumor is "YES" and for healthy brain images, the output produced is "NO" as shown in Figure 3.

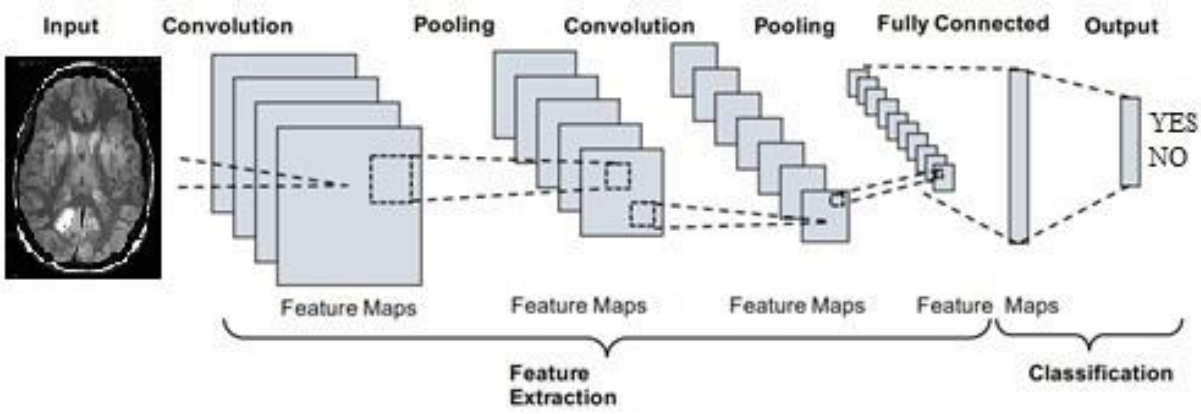

Figure 3. Block Diagram of the Implemented System

Dataset Descriptions

In this study, two datasets, namely Kaggle (Kaggle Brain Tumor Dataset, 2020) and Figshare (Figshare Brain Tumor Dataset, 2018) are employed for the experiments. In the train folder of Kaggle dataset, there are 1200 images labeled as "yes" and 1200 images labeled as "no", which makes a total of 2400 images in the train folder. In the test folder, there are 300 images labeled as "yes" and 300 images named as "no" which makes a total of 600 images in the test folder. Therefore, Kaggle image dataset in this dataset includes 3000 images totally.

On the other hand, the second dataset, named Figshare, includes two files entitled "test" and "train". In the train folder, there are 4117 images considered as "yes" and 1588 images termed as "no" and there is a total of 5705 images in the train folder. In the test folder, there are 906 images considered as "yes" and 405 images called "no" and there is an overall of 1311 images in the test folder. However, because of the quality of some images in Figshare dataset, some of the images are not used in the experiments. Consequently, in the experiments, 5600 images are selected for training and 1400 images are selected for testing which makes use of total 7000 images in our Figshare dataset.

Performance Metrics

This section discusses metrics for evaluation, which are accustomed to assess the value of a model statistically. A number of evaluation measures can be employed to show the value of a model such as accuracy, precision, and recall. The evaluation metrics used in DL tasks are critical in determining the best classifier. They are employed in the testing and training stages of a typical data classification process. During the phase of training, it is employed to improve the algorithm of classification. This indicates that the assessment measure is utilized to distinguish between options and select the best one, such as a discriminator, which can yield a more precise estimate of future evaluations when used in conjunction with an exact classifier. In the meantime, the assessment metric is accustomed to analyze the developed classifier's effectiveness, such as a hidden data evaluator during the model test phase. The number of effectively classified negative and positive instances is denoted by TN and TP, respectively. Furthermore, the

amounts of misclassified positive and negative cases are defined as FN and FP, respectively. The following are around of the supreme famous evaluation metrics.

1) Accuracy: Computes the percentage of correctly forecast classes in relation to the overall number of samples that were tested. Accuracy can be calculated as follows:

$$\text{Accuracy} = \frac{\text{TP+TN}}{\text{TP+TN+FP+FN}} \quad (1)$$

where TP is the number of true positives that are perfectly recognized. The total of perfectly-identified true negatives is recognized as TN. FP denotes the number of images that are wrongly recognized in place of positive but are really negative. FN is the sum of falsely detected negatives that are truly positive.

Accuracy values are in the range [0,100] percent. If we divide that range evenly, 100-87.5% equals very good, 87.5-75% equals good, 75-62.5% equals satisfactory, and 62.5-50% equals bad. In reality, we regard numbers between 100 and 95% to be excellent, 95 to 85% to be good, 85 to 70% to be satisfactory, and 70 to 50% to be “needs to be improved” for brain tumor recognition.

2) Recall or Sensitivity: The percentage of successfully classified positive patterns is calculated using sensitivity or recall as shown below:

$$\text{Sensitivity} = \frac{\text{TP}}{\text{TP+FN}} \quad (2)$$

where TP is the total number of true positives that are perfectly recognized. FN is the total of falsely detected negatives that are truly positives. The recall is calculated as TP/FN, in which TP represents true positives, and FN represents false negatives. The recall of a classifier refers to its ability to locate all samples that are positive. 1 is the best value while 0 is the worst.

3) Specificity: is used to calculate the percentage of incorrectly classified negative patterns. The formula of specificity is as follows:

$$\text{Specificity} = \frac{\text{TN}}{\text{FP+TN}} \quad (3)$$

where the quantity of perfectly-identified negative images is equal to TN. FP denotes the quantity of positive images that are wrongly known as positive but are truly negative.

In an ideal world, the model would have a high specificity or true negative rate. A greater specificity score would imply a higher real negative rate and a decreased rate of false-positives. A reduced specificity score indicates a lower genuineness score.

4) Precision: is used to figure out which positive patterns in a positive class are the most common. Precision is calculated as follows:

$$\text{Precision} = \frac{\text{TP}}{\text{TP+FP}} \quad (4)$$

where TP is the total of fully recognized positive images. The sum of positive images that are wrongly recognized as positive but are essentially negative is referred to as FP. Precision can be used as a measure of quality. When an algorithm's precision is higher, it produces more relevant outcomes rather than irrelevant ones.

5) F1-Score: also known as F-score and F-measure, is a model's accuracy on a dataset. It is used to assess binary classification systems that categorize examples as positive or negative. F1-Score is calculated as follows:

$$\text{F1 Score} = 2 * \frac{\text{Precision}*\text{Recall}}{\text{Precision} + \text{Recall}} \quad (5)$$

where recall (also called sensitivity) is the percent of related examples identified, and precision for positive predictive value is the proportion of applicable examples found among the improved instances. The greatest rate of an F-score is 1.0, which implies faultless accuracy and recall, while the minimum value is 0 if neither precision nor recall is 0.

RESULTS AND DISCUSSION

This section presents the experimental results obtained using Kaggle and Figshare datasets for brain tumor classification. Afterward, the discussion about the results is given and the comparison with the state-of-the-art demonstrates an analysis of different studies and findings on brain tumor classification and the comparison of these findings with the results obtained in this study.

Results

All evaluation metrics and methods applied for both datasets are described in Table 1 and Table 2. All values and results obtained in these experiments are demonstrated in details. The pathological brain images were taken from the Kaggle dataset and there are two folders called test and train to analyze the performance of each prediction model.

When Figshare dataset is used, the results for three different models (AlexNet, VGG16 and ResNet) are better than when Kaggle dataset is used. The reason for this is that the total images in Figshare dataset is more than the amount of images in Kaggle dataset and also the quality of images in Figshare dataset is better than the quality of images in Kaggle dataset finally, these models are more compatible with Figshare dataset compared to Kaggle dataset.

Table 1. Brain Tumor Classification Results on Kaggle Dataset

Evaluation metric	**Method Used**		
	AlexNet	VGG16	ResNet
Accuracy	0.9883	0.9733	0.6667
Precision	0.9895	0.9767	0.6185
Recall(Sensitivity)	0.9861	0.9703	0.9258
Specificity	0.9904	0.9764	0.3897
F-Measure	0.9878	0.9735	0.7416

Table 2. Brain Tumor Classification Results on Figshare Dataset

Evaluation metric	**Method Used**		
	AlexNet	VGG16	ResNet
Accuracy	0.9943	0.9915	0.9658
Precision	0.9960	0.9928	0.9818
Recall(Sensitivity)	0.9960	0.9948	0.9700
Specificity	0.9900	0.9840	0.9553
F-Measure	0.9960	0.9938	0.9759

Comparison with the State-of-the-Art

Expert radiologists perform the crucial task of brain tumor segmentation and classification. As decision-making aids, radiologists can use ML and DL methods. This paper outlines a number of cutting-edge methodologies for classifying brain tumors automatically. Brain tumor classification results are compared on Kaggle Brain MRI and Figshare Brain MRI datasets in Table 3. In Kaggle dataset, a total of 2400 images exist in the train folder. There is a total of 600 images in the test folder. All the train and test images in Kaggle dataset are used in the experiments. Additionally, there is another dataset named Figshare in which 5600 train images and 1400 test images are selected and used in the experiments. All of the images available in Kaggle dataset are used in this study, however, some of the low quality images in Figshare dataset are not utilized in that dataset.

In recent years, there have been several state-of-the-art studies for the classification of brain MRI images using Kaggle Brain MRI dataset and Figshare Brain MRI dataset. Comparison with the state-of-the-art methods in Table 3 indicates that the results on Kaggle Brain MRI dataset show that most of the DL architectures, such as AlexNet and VGG16, achieve better results compared to handcrafted methods. Similarly, the results on Figshare Brain MRI dataset show that AlexNet achieves the best accuracies for the classification of brain tumors. The best accuracies obtained using AlexNet on Kaggle Brain MRI dataset and Figshare Brain MRI dataset are 98.83% and 99.43%,

respectively. It means that using these DL methods can be helpful for achieving better accuracy and results, especially in the medical fields, because of the disease diagnosis in the initial steps is very crucial and vital in these fields.

Table 3. Comparison with the State-of-the-Art on Kaggle and Figshare Datasets

Autours	Preprocessing and Segmentation	Feature Extraction and Classification	Dataset	Accuracy
Manav et al., (2021)	Segmentation, Image Enhancement	Pixel-based feature extraction and CNN.	Kaggle	97.79%
Prabira & Santi, (2021)	Deep Fusion	PCA and fused deep features and SVM.	Kaggle	97.89%
Arshia et al., (2020)	N/A	VGG16	Figshare	98.69%
Polat & Güngen, (2021)	N/A	DenseNet121, ResNet50.	Figshare	98.91%, 99.02%
This Study	N/A	AlexNet	Kaggle	98.83%
This Study	N/A	VGG16	Kaggle	97.33%
This Study	N/A	ResNet	Kaggle	66.67%
This Study	N/A	AlexNet	Figshare	99.43%
This Study	N/A	VGG16	Figshare	99.15%
This Study	N/A	ResNet	Figshare	96.58%

CONCLUSION

In this paper, three DL models including Alexnet, VGG16 and ResNet are utilized to classify brain tumors by employing MRI images. The performances of these models have been investigated using two datasets, namely Kaggle and Figshare, and five metrics are used to calculate their performances. AlexNet achieves 98% accuracy on the Kaggle dataset, VGG16 has 97% accuracy, and ResNet gets 66% accuracy. AlexNet has offered the highest level of accuracy among these networks. On the other hand, AlexNet achieves 99% accuracy in the Figshare dataset, VGG16 gets 99% accuracy, and ResNet has 96% accuracy. AlexNet and VGG16 outperform ResNet in terms of accuracy. These accuracies allow for the early detection of abnormalities before they create physical harm such as disability or other complications. The experimental results reveal that DL models perform well on Figshare Brain MRI dataset and Kaggle Brain MRI dataset, however, better accuracy is obtained on the Figshare dataset. The reason for this is that we have more images in the train and test sections when Figshare dataset is used. Therefore, the efficiency is increased, and better results are obtained on Figshare dataset. For future work, since identifying the exact location of a brain tumor is very important and the location of the tumor determines the need for surgery to remove malignant tumors, other segmentation methods can be investigated. Additionally, more powerful and efficient DL architectures, such as ResNet50, can be used to increase the accuracy of brain tumor classification.

REFERENCES

Amin, J., Sharif, M., Mussarat,Y., Fernandes, S.L. (2018). Big Data Analysis for Brain Tumor Detection: Deep Convolutiona Neural Networks. Future Gener. Comput. Syst., vol.87. 290–.297. https://doi.org/10.1016/j.future.2018.04.065.

Arshia, R., Saeeda, N., Muhammad, I.R., Faiza, A., Muhammad, I. (2020). A Deep Learning-based Framework for Automatic Brain Tumors Classification Using Transfer Learning, Circuits, Systems and Signal Processing. vol. 39, 757-775.https://doi.org/10.1007/s00034-019-01246-3.

Çınar, A. & Yıldırım, M. (2020). Detection of Tumors on Brain MRI Images Using the Hybrid Convolutional Neural Network Architecture, Med. Hypotheses, 139 (2020), 109684. https://doi.org/10.1016/j.mehy.2020.109684.

Deepak, R. & Ameer, P.M. (2019). Brain Tumor Classification Using Deep CNN Features via Transfer Learning, Computers in Biology and Medicine, 1-7. https://doi.org/10.1016/j.compbiomed.2019.103345.

Figshare Brain Tumor Dataset, https://doi.org/10.6084/m9.figshare.1512427.v5, Accessed: December 2018.

Gumaei, A., Hassan, M.M., Hassan, M.R., Alelaiwi, A. N., Fortino, G. A. (2019). Hybrid Feature Extraction Method with Regularized Extreme Learning Machinefor Brain Tumor Classification. 36266-36273.https://doi.org/ 10.1109/ACCESS.2019.2904145.

Hasan, A.M., Jalab, H.A., Meziane, F., Kahtan, H., Ahmad, A.S. (2019). Combining Deep and Handcrafted Image Features for MRI Brain Scan Classification. IEEE Access. 79959–79967. https://doi.org/10.1109/ACCESS.2019.2922691.

Hemanth, G., Janardhan, M., Sujihelen, L. (2019). Design and Implementing Brain Tumor Detection Using Machine Learning Approach . Third International Conference on Trends in Electronics and Informatics.1-6..https://doi.org/ 10.1109/ICOEI.2019.8862553.

Huafeng, W., Haixia, P., Huafeng,W., Yanxiang , Z., Yehe, C. (2015). Deep Learning for Image Retrieval: What Works and What Doesn't, Conference Paper .1-22.https://doi.org/10.1109/ICDMW.2015.121.

Kaggle Brain Tumor Classification (MRI) dataset, by Bhuvaji, S., Kadam, A., Bhumkar, P., Dedge, S., Kanchan, S., https://doi.org/10.34740/KAGGLE/DSV/1183165, Accessed: December 2020.

Kebir, S.T. & Mekaoui, S. (2018). An Efficient Methodology Of Brain Abnormalities Detection Using CNN Deep Learning Network. in Proc. Int. Conf.Appl. Smart Syst. (ICASS). https://doi.org/10.1109/ICASS.2018.8652054.2018.

Latif, G., Iskandar, D., Alghazo, N.F., Mohammad, J.M.N. (2018). Enhanced MR Image Classification Using Hybrid Statistical and Wavelets Features. IEEE Access .9634- 9644.https://doi.org/10.1109/ACCESS.

2018.2888488.

Manav, S., Pramanshu, S., Ritik, M., Kamakshi, G. (2021). Brain Tumour Detection Using Machine Learning . Journal of Electronics and Informatics, Volume 3, Issue 4. 298-308, 2021. https://doi.org/10.36548/jei.2021.4.005.

Minz, A. & Mahobiya, C. (2017). MR Image Classification Using Adaboost for Brain Tumor Type. IEEE 7th International Advance Computing Conference .1-5.https://doi.org/10.1109/IACC.2017.0146.

Mohsen, H., Sayed, E., Dahshan, E., Badeeh, A., Salem, M. (2018). Classification Using Deep learning Neural networks for Brain Tumors Future. Computing and Informatics Journal.68-73.https://doi.org/10.1109/ACCESS.2018.2888488.

Narayana, R.L. & Reddy, T.S. (2018). An Efficient Optimization Technique to Detect Brain Tumor from MRI Images. International Conference on Smart Systems and Inventive Technology.1-4.https://doi.org/10.1109/ICSSIT.2018.8748288.

Polat, Ö. & Güngen, C . (2021). Classification of Brain Tumors from MR Images Using Deep Transfer Learning. The Journal of Supercomputing ,volume 77. 7236–7252. https://doi.org/10.1007/s11227-020-03572-9.

Polly, E.P., Shil, S.K., Hossain, M.A., Ayman, A., Jang, Y.M. (2018). Detection and Classification of HGG and LGG BrainTumor Using Machine Learning. International conference on Information Networking. 813-817.https://doi.org/10.1109/ICOIN.2018.8343231.

Prabira, K.S. & Santi, K.B. (2021). A Data Constrained Approach for Brain Tumour Detection Using Fused Deep Features and SVM, Multimedia Tools and Applications, vol. 80, 28745-28760.https://doi.org/10.1007/s11042-021-11098-2.

Rehman, A., Khan, M.A., Saba, T.Z., Mehmood, T.U., Ayesha, N. (2021). Microscopic Brain Tumor Detection And Classification Using 3D CNN And Feature Selection Architecture. Microsc. Res. Techn, vol. 84, no. 1,133–149, 2021. https://doi.org/10.1002/jemt.23597.2021.

Rehman,A., Naz, S., Razzak,M.I., Akram ,F., Imran,M.Amin, J., Sharif, M., Yasmin, M., Fernandis, S.(2017). A Distinctive Approach in Brain Tumor Detection and Classification Using MRI. Pattern Recognition Letters.1-10.https://doi.org/10.1016/j.patrec.2017.10.036.

Sethy, P.K. & Behera, S.K. (2021). A Data Constrained Approach for Brain Tumour Detection Using Fused Deep Features and SVM . Multimedia Tools and Applications (2021) 80.28745–28760.https://doi.org/10.1007/s11042-021-11098-2.

Sert, E., Ozyurt, F., Doğantekin, A. (2019). A New Approach for Brain Tumor Diagnosis System: Single Image Superresolution Based Maximum Fuzzy Entropy Segmentation and Convolutional Neural Network. Medical Hypothesis.1-9.https://doi.org/10.1016/j.mehy.2019.109413.

Shankar, A.S., Asokan, A., Sivakumar, D. (2016). Brain Tumor Classification Using Gustafson–kessel (G-k) Fuzzy Clustering Algorithm. International Journal of Latest Engineering Research and Applications .68-72.

Simonyan, K. & Zisserman, A. (2014). Very Deep Convolutional Networks for Large-Scale Image Recognition. arXiv preprint arXiv:1409.1556.https://doi.org/10.1109/ACPR.2015.7486599.

Talo, M., Baloglu, U.B., Yıldırım, O., Acharya, U.R. (2019). Application Of Deep Transfer Learning For Automated Brain Abnormality Classification Using MRI Images.Cognitive Systems Research, 54(2019), 176–188.https://doi.org/10.1016/j.cogsys.2018.12.007.

Vinoth, R. & Venkatesh, C. (2018). Segmentation And Detection Of Tumor in MRI Images Using CNN And SVM Classification. in Proc. Conf. Emerg. Devices Smart Syst. (ICEDSS). 21–25. https://doi.org/10.1109/ICEDSS.2018.8544306.2018.

Wang, F.& Gong, M. (2020). Single Image Super-Resolution by Residual Recovery Based On an Independent Deep Convolutional Network.VOLUME 4.1–10.https://doi.org/10.1109/ACCESS.2020.2986365.

Wang, H., Pan, H., Zhang, Y., Cai,Y. (2015). Deep Learning for Image Retrieval: What Works and What Doesn't. Conference Paper ·1-22. https://doi.org/10.1109/ICDMW.2015.121.

Zaw, H.T., Maneerat, N., Win, K.Y. (2019). Brain Tumor Detection Based On Naïve Bayes Classification. International Conference on Engineering, Applied Sciences and Technology.1-4. https://doi.org/10.1109/ICEAST.2019.8802562.